Structured beam optical parametric oscillators

This dissertation is submitted for the degree of

Doctor of Philosophy

by

Varun Sharma

(Roll No. 15330014)

Under the guidance of

Dr. Goutam K Samanta

Associate Professor

Atomic Molecular and Optical Physics Division

Physical Research Laboratory. Ahmedabad

Discipline of Physics

Indian Institute of Technology Gandhinagar

To

My Parents, Grandmother

&

My better half

Declaration

I declare that this written submission represents my ideas in my own words and wherever others ideas or words have been included, I have properly cited and referenced the original sources. I also declare that I have adhered to all principles of academic honesty and integrity and have not misrepresented or fabricated or falsified any idea/data/fact/source in my submission. I understand that any violation of the above can cause disciplinary action by the Institute and can also evoke penal action from the sources which have thus not been properly cited or from whom proper permission has not been taken when needed.

Varun Sharma

Roll No. 15330014

Certificate

It is certified that the work contained in the thesis titled "Structured Beam Optical Parametric Oscillators" by Varun Sharma(Roll no: 15330014), has been carried out under my supervision and that this work has not been submitted elsewhere for a degree. I have read this dissertation and that, in my opinion, it is fully adequate in scope and quality as a dissertation for the degree of Doctor of Philosophy.

Dr. Goutam Kumar Samanta

Associate Professor

Atomic Molecular and Optical Physics Division

Physical Research Laboratory, Ahmedabad

Acknowledgments

Writing acknowledgment is a difficult part, as it requires to concise your PhD tenure and writes (thoughts?) about that time. I had a nice time during my PhD tenure in PRL Thaltej and Ahmedabad. When I first entered Ahmedabad for the PhD interview, I thought not to come back to this hot weather again. Fortunately, I was back to pursue my degree here, and moreover, I got connected with people who made my stay comfortable. I take this opportunity to present my heartiest gratitudes towards them.

First and foremost, I would like to express my sincere gratitude toward my thesis advisor Dr. Goutam K Samanta. During the graduation period, we used to hear different good and bad stories about PhD tenure and in most of those stories the supervisor used to be the central character. Fortunately, I am blessed to be supervised by Dr. Goutam K Samanta, the most dynamic person, I have ever met. I can starkly remember the first meeting I had with him, outside the PRL Thaltej canteen, where all the group members accompanied him. It was indeed surprising and at the same time difficult for me to figure out the hierarchy in the relation of an advisor and his students, as everyone present there behaved like close friends. After a few interactions and lab visits, I was certain to join his group. This decision was a result of the work culture I experienced during my initial days of the projects and feeling of togetherness like a family in the group. Moreover, the whole group used to play football on weekends and as a passionate footballer, it was like a holy grail for me. During my PhD tenure, I had a great time and may fruitful discussions with Dr. Goutam K Samanta, specifically his ability to come up with a solution for each problem. His experimental skills and immense knowledge of nonlinear optics helped me to complete each project within the stipulated period. His endless support at a personal as well as professional level, helped me to carry out thesis work in a balanced manner. I would like to take this opportunity and put my sincerest thanks to Dr. Goutam K Samanta for guiding my thesis work and helping me out in each step of PhD tenure.

I would like to thank, Prof. Majid Ebrahim-Zadeh and Dr. Suddapalli Chaitanya Kumar, for providing me an opportunity to work in Optical parametric oscillator group at ICFO Barcelona. I am out of words to express my sincerest gratitude toward Prof. Zadeh, for his constant endless support throughout. My stay in Barcelona could not have been perfect without the support of Dr. Suddapalli Chaitanya Kumar. His support for experiments during the daytime and most of the dinner hosted by him made my stay in Barcelona comfortable. I learned a lot from him during my stay in Barcelona, specifically his commitment toward work is exceptionally brilliant. I acquired great experimental skills from him while working at ICFO Barcelona and implemented for the completion of my thesis work. I would like to thank our area chairperson at PRL Ahmedabad, Prof. R P Singh for his constant support during my PhD tenure. In my opinion, no one can get a better person to lead a division other than Prof. R P Singh. I am thankful to Dr. Rajesh Kumar Kushawaha and Prof. R P Sir for guiding me during my PhD tenure as my DSC member. After entering the lab, fortunately, I got great senior members in the lab who became great mentors and friends with me. I want to take this opportunity to thank A Aadhi, Apurv Chaitanya and Jabir M V for helping me in various experiments.

I would like to express my sincerest gratitude toward PRL Director, Prof. Anil Bhardwaj for his constant support throughout my PhD tenure. I would like to thank him for his support for various student outreach activities done by the PRL student chapter. His endless support for the SCOP-2019 also made the conference huge success and personally gave me an opportunity to lead the SCOP-2019 team.

I would also like to take this opportunity to thank Academic services, Administrative services, workshop, computer center and all the other members of PRL family for all the help, love and care they have given to me and made my four years feel short in PRL.

PhD tenures being quite rigorous, with an overflow of pending work sometimes, it's essential to take regular breaks from the hectitic work schedules. Other than friends no one can make that time more enjoyable. It's very difficult to find great friends who take care of you, no matter however you are. I would like to specially thank Nidhi Tripathi for her endless care as a great neighbor and one of the best friends here in PRL Ahmedabad. I would like to thank Kaustov Chakraborty for many trips he travelled with me and enjoyment we had at the sand dunes of Jaisalmer, hills of Lonavala and National park of Ranthambhore. I would like to acknowledge Shefali, Subir, Akanksha, Archita, Aarthy, Rahul, for a lot of cherished memories I had in PRL Ahmedabad. I would like to mention special thanks to Subir, for his support as a great friend and his invitations for lunch and dinner. I would like to put it on record here that, no one can cook better food than Subir Mandal. I would like to thank my food partners, Abdur, and Sandeep for accompanying and sharing a lot of stories over dinner time.

SCOP-2019 was one of the event I was fortunate to organize. I would like to thank the SCOP-2019 team for working with me and making that conference a success. I would like to specially thank Ayan Biswas for his friendship and for sharing the responsibility for this conference.

I would like to thank all my current and past group members for common understanding and helping me during my experiments. I had a great time with Dr. Raghwinder Singh, Dr. Ravikiran Sarripalli, Dr. A S Rao, Dr. Deepika Yadav, Harshith, Anirban Ghosh, Vimlesh Kumar, and Subith P Kumar during my stay in the lab and PRL Ahmedabad. I would like to special thank Harshith and Ravi for helping me in writing my thesis and advising me on thesis improvement.

This is the hardest part of thanking; Starting, my PhD at PRL Ahmedabad would have been not possible if Neha has not forced me to attend the interview and booked my tickets for the Journey. I am fortunate to have her in my life as my life partner. Her constant support and care helped me to go through any tough situation very easily. There are no words, which can explain my thanks toward the care, the support I got from her.

And lastly but foremost, I would like to thank my whole family for their constant support and endless love I get throughout my life. I cannot express my gratitude and thanks to my parents for their endless love. I learned a lot from my father and mother starting from my childhood and my mother’s tender care brought me as a good human being and helped me to achieve various recognition. I thank my brother and sister in law for their love and affection. And special thanks to little Vedika for bringing joy to my face whenever I talk with her.

Abstract

The applications of lasers cover almost all fields of science and technology including medical diagnosis, lithography, communication and material processing. Typically, lasers, the main source of coherent optical radiation, are characterised with the performance parameters such as output power, energy, temporal, and spectral features. However, they typically provide output radiation in the Gaussian spatial intensity distribution. While the majority of the scientific and technological applications require laser beams in Gaussian spatial distribution, however, in recent times laser beams with different spatial structures have also attracted a great deal of interest. For example, optical vortices are important for material processing, lithography, quantum information, particle manipulation and high-resolution microscopy. Similarly, Airy beam, a non-diffraction waveform, finds many applications in curved plasma wave-guiding, micro-particle manipulation for optically mediated particle clearing and light-sheet microscopy. The applications of all these different spatial structures extend across the entire electromagnetic spectrum. For example, optical vortices in the short wavelength region have their application in quantum and long-wavelength region such as mid-IR and THz vortices are essential for the spectroscopy. Similar, to optical vortices, Airy beam, and vector beams are prepared across the different spectral region from ultraviolet to mid-IR for various applications. For demonstrations of these applications, lasers in the Gaussian intensity distribution are used along with different phase elements. There are few conventional elements used for spatial beam shaping such as liquid crystal-based spatial light modulators (SLM) or dielectric phase elements. However, with new emerging and ever increasing applications of structured beams over different wavelengths, there is a humongous demand for their generation with high power and broad wavelength coverage.

Unfortunately, most of the commercially available lasers used for the generation of structured beams have certain drawbacks in terms of limited or no tunability, high cost, and complicated design. Some of the shortcomings can be overcome by choosing a proper system design. However, the generation of wide tunable radiation from a laser itself is limited by the availability of suitable gain medium. Such unavailability of gain medium restricts access to many wavelength regions ranging from the ultraviolet (UV) to mid-IR spectrum. Additionally, due to the normal dispersion, the phase elements used to generate structured beams are

wavelength-selective. For example, a spiral phase plate used to generate optical vortices at 532 nm cannot be used for other wavelengths. While liquid crystal-based spatial light modulators can have limited wavelength coverage but such systems have lower damage threshold and do not provide high output powers. Moreover, all commercially available phase elements have limitations for the generation of structured beams in UV and the mid-IR region due to the limitations of lithography techniques and high absorption in those wavelength regions. All these limitations restrict the generation of structured beams at a wide range of wavelengths using lasers

On the other hand, optical parametric oscillators (OPOs) have become a well-established technology to generate coherent radiations inaccessible to lasers. Based on the nonlinear frequency conversion process of a single pump laser, the OPOs produce optical radiation tunable over a wide wavelength range from UV to deep mid-IR region. Like lasers, the optical parametric oscillators have three basic requirements, pumping, gain medium and the optical cavity. However, in contrary to the lasers, the OPOs have instantaneous parametric gain along the direction of the pump. The OPO's are designed in various cavity configurations, like singly resonant, where one of the generated beams resonate, doubly resonant, where both the generated beams resonate, or triply resonant, where all the interacting beams resonate in the cavity to overcome the losses inside the cavity. While the parametric gain increases with the number of resonating beams in the OPO, however, the increase of the number resonating beams degrade the performance of the systems in terms of output power and the system stability. On the other hand, as the nonlinear parametric gain can be controlled using the pump intensity, the conventional OPOs utilize pump beam in Gaussian intensity distribution. Further, for efficient energy transfer among the interacting beams, the resonating beams oscillate in fundamental cavity mode of the oscillator producing output radiation in Gaussian intensity distribution. As such, to utilize the OPOs for structured beam generation, one need either manipulate the pump beam spatial structure or produce higher order cavity mode of the OPO through higher pump intensity. However, the spatial structuring of the pump lead to the lower parametric gain and subsequent increase in the OPO threshold as compared to conventional OPOs reported so far. On contrary, the increase of pump energy to increase the parametric gain to excite higher order cavity modes inside the OPO is restricted to the damage of the nonlinear gain medium. To overcome such challenges to generate structured beams directly from an OPO, one needs better OPO cavity designs for maximum gain extraction, and the selection of suitable cavity mirrors, nonlinear crystals and pump sources. In this thesis, we addressed the generation of various structured coherent beams including the Gaussian beam, optical vortex beam, vector vortex beams, Airy beam, and vortex Airy beam across the ultraviolet to the mid-IR region in all time scales (from ultrafast as well as continuous-wave) based on OPOs.

While the optical vortices are generated through the spatial mode conversion of the Gaussin beam using a transverse phase element, we tried to avoid the use of any phase element to generate optical vortices from a continuous-wave (cw), Gaussian beam pumped doubly resonating optical parametric oscillator (DRO). The basic principle of such vortex generation is the superposition of two Gaussian beams with lateral phase shift inside the OPO cavity. Using a 30-mm long MgO doped periodically poled lithium tantalate (MgO:sPPLT) crystal based DRO, pumped in the green by a frequency-doubled Yb-fiber laser in Gaussian spatial profile we have generated signal and idler beams in vortex mode of order, l=1, tunable across 970-1178 nm. Controlling the spatial overlap between the Gaussian pump beam with the fundamental cavity mode of the resonant signal and idler beams of the DRO through the tilt of the pump beam and/or the cavity mirror in the transverse plane, we generated both signal and idler beams in vortex and vortex dipole spatial profiles. However, due to the high reflectivity of the cavity mirrors, the generated vortex and vortex dipole beams have substantially low output power. To increase the output power of the vortex beam we have explored the Gaussian beam superposition using an anti-resonant ring based picosecond OPO configuration. With the help of two mirrors of the anti-resonant ring, we introduced a linear phase in the superposed beams and successfully generated optical vortices in the near-IR region from 1457 to 1657 nm with output power in excess of 860 mW.

While we have successfully generated tunable vortex beam of substaintial output power using an OPO without use of any transverse phase modulator, however, the order of the vortex by this technique is limited to l=1. Therefore, to generate higher order optical vortices using OPO, we have used vortex beam pumped OPOs. Conventionally, in singly resonant OPOs (SROs), the vortex pumping enables the generation of optical vortices in the non-resonant beam while resonating beam oscillate in Gaussian mode due to lower threshold and high gain. Therefore, we have demonstrated the control of orbital angular momentum (OAM) exchange among the interacting beams using a synchronously pumped by a picosecond SRO. Using vortex pump beam from a frequency-doubled Yb-fiber laser at 532 nm in the green we have demonstrated the successful transfer of the pump OAM mode to the non-resonant idler beam tunable across 1109-1209 nm, with OAM as high as l_p=3. Controlling the cavity loss and spatial overlap between the resonant signal and the pump beam in the nonlinear crystal, we have generated signal and idler OAM mode combinations, (l_s,l_i) of (0,2), (1,1) and (0,3), (1,2) for pump OAM mode l_p=2 and 3, respectively. Using a pump power of 1 W, we have generated idler OAM mode of orders, l_i=1, 2, and 3, with maximum output powers of 202, 113, and 57 mW, respectively.

Further, we have demonstrated the generation of tunable, ultrafast optical vortices in mid-IR from a picosecond SRO. Using a SRO based on multigrating MgO doped PPLN crystal and synchronously pumped by a picosecond Yb-fiber laser centered at 1064 nm we have demonstrated for the first time an ultrafast OPO in the mid-IR spectral region pumped with pump vortex order as high as l_p=5. We have successfully demonstrated the transfer of pump optical vortices directly to the non-resonant idler beam, while the signal resonates in Gaussian cavity mode and generated optical vortices from 2538 nm to 4035 nm with a maximum output power of 1.6 W at vortex order of l_i=1.

To increase the span of wavelength coverage of the vortex beam OPO, we have generated optical vortices in the ultraviolet wavelength range using a continuous-wave (cw) OPO. Based on a MgO:sPPLT as the nonlinear crystal, the SRO is pumped by a cw vortex beam in the green, and deploying intracavity sum-frequency-generation (SFG) between the undepleted pump and the resonant Gaussian signal in the crystal second nonlinear crystal (BiB_3O_6), we have generated optical vortices of order, l_{uv}=1 and 2, tunable across 332-344 nm in the UV with a maximum power of 12 mW. Due to the conservation of orbital angular momentum in the parametric process, the OPO also produces non-resonant idler output beam in the vortex spatial profile of order, l_i=1 and 2, identical to the pump vortex, with the signal beam in Gaussian distribution. The idler vortex is tunable across 1172-1338 nm with a maximum output power of 1.3 W.

Given the nonlinear frequency conversion processes depend on the polarization state of the interacting beams, convensionally the OPOs so far produces vortex beams with uninform polarization in the transverse plane of the beam commonly known as scalar vortex beams. However, there exist another set of vortex beams known as *vector vortex beams*, where, the beams have space-variant polarization in the transverse beam plane. We have explored the possibility of generating tunable vector-vortex beams directly from the OPO source. Exploiting the orbital angular momentum conservation, we have systematically control the polarization of the resonant beam using a pair of intracavity quarter-wave plates to generate coherent vector-vortex beam tunable across 964-990 nm, with output states represented on the higher-order

Poincaré sphere. The generic experimental scheme paves the way for new sources of structured beams in any wavelength range across the optical spectrum and in all time-scales from cw to the ultrafast regime.

While we have addressed the generation of vortex beams and vector vortex beams from OPO, however, each of those beams require a dedicated experimental setup. As a result, one need to design a dedicated experiment setup to generate the desire spatial structured beam. To avoid such difficulty, in the current thesis we have tried to address the possibility of generating tunable multiple structured optical beams from a single OPO source. Using vortex pumping and controlling the spatial mode and subsequent intracavity cubic phase modulation of the resonant beam of an OPO, we have successfully demonstrated the simultaneous generation of multiple spatial structures in the near-IR to mid-IR wavelength region. Using a synchronously pumped SRO with pump vortex order of $l_p = 2$ and controlling the pump OAM transfer between signal and idler, for OAM mode combination of (l_s, l_i)=(0,2), we generated Gaussian and Airy beam in signal and vortex beam in idler wavelength range. On the other hand, for OAM mode combination of the signal and idler, (l_s, l_i)=(1,1) we have further generated, vortex and vortex-Airy beam in signal and vortex beam in idler wavelength range. All these generated structures are tunable from 1457 nm to 1680 nm in signal and 2901 to 3944 nm in idler with excess power of 980 mW.

Publications and manuscripts under preparation

Included in this thesis

1. **Varun Sharma**, G. K. Samanta, S. Chaitanya Kumar, R. P. Singh, and M. Ebrahim-Zadeh, "Tunable ultraviolet vortex source based on a continuous-wave optical parametric oscillator," Optics Letters 44, 4694-4697 (2019)
2. **Varun Sharma**, S. Chaitanya Kumar, A. Aadhi, H. Ye, G. K. Samanta, and M. Ebrahim-Zadeh, "Tunable vector-vortex beam optical parametric oscillator," Scientific Reports 9, 9578 (2019)
3. **Varun Sharma**, A. Aadhi, and G. K. Samanta, "Controlled generation of vortex and vortex dipole from a Gaussian pumped optical parametric oscillator," Optics Express 27, 18123-18130 (2019)
4. **Varun Sharma**, S. Chaitanya Kumar, G. K. Samanta, and M. Ebrahim-Zadeh, "Orbital angular momentum exchange in a picosecond optical parametric oscillator," Optics Letters 43, 3606-3609 (2018)
5. **Varun Sharma**, S. Chaitanya Kumar, G. K. Samanta, and M. Ebrahim-Zadeh, "Ultrafast mid-IR vortex pumped picosecond optical parametric oscillator," submitted to Optics Express.
6. **Varun Sharma**, S. C. Kumar, G. K. Samanta, and M. Ebrahim-Zadeh, "Optical vortex generation from an anti-resonant-ring picosecond optical parametric oscillator," in *2019 Conference on Lasers and Electro-Optics Europe and European Quantum Electronics Conference*, OSA Technical Digest (Optical Society of America, 2019), paper cd_8_5 and **manuscript under preparation** for journal publication.
7. **Varun Sharma**, S. C. Kumar, G. K. Samanta, and M. Ebrahim-Zadeh, "Tunable multi-structured-beam optical parametric oscillator," in *Frontiers in Optics + Laser Science APS/DLS*, The Optical Society (Optical Society of America, 2019), paper JW3A.41 and **manuscript under preparation** for journal publication.

Not included in this thesis

1. A. Aadhi, **Varun Sharma**, and G. K. Samanta, "High-power, continuous-wave, tunable mid-IR, higher-order vortex beam optical parametric oscillator," Optics Letters 43, 2312-2315 (2018).
2. A. Aadhi, **Varun Sharma**, N. Apurv Chaitanya and G. K. Samanta, "Multi-GHz Femtosecond Airy Beam Radiation in Higher-harmonic Fractional Cavity OPO," Scientific Reports 7, 43913 (2017).
3. A. Aadhi, **Varun Sharma**, R.P. Singh and G. K. Samanta, "Continuous-wave. Singly resonant parametric oscillator based mid-infrared optical vortex source," Optics Letters 42, 3674-3677 (2017).

Selected conference papers

1. **Varun Sharma**, S. C. Kumar, G. K. Samanta, and M. Ebrahim-Zadeh, "Tunable multi-structured-beam optical parametric oscillator," in Frontiers in Optics + Laser Science APS/DLS, The Optical Society (Optical Society of America, 2019), paper JW3A.41.
2. **Varun Sharma**, S. C. Kumar, G. K. Samanta, and M. Ebrahim-Zadeh, "Optical vortex generation from an anti-resonant-ring picosecond optical parametric oscillator," in 2019 Conference on Lasers and Electro-Optics Europe and European Quantum Electronics Conference, OSA Technical Digest (Optical Society of America, 2019), paper cd_8_5.
3. **Varun Sharma**, S. C. Kumar, A. Aadhi, H. Ye, G. K. Samanta, and M. Ebrahim-Zadeh, "Vector vortex beam generation from a doubly-resonant nanosecond optical parametric oscillator," in Frontiers in Optics / Laser Science, OSA Technical Digest (Optical Society of America, 2018), paper JW4A.50.
4. **Varun Sharma**, G. K. Samanta, R. P. Singh, S. C. Kumar, and M. Ebrahim-Zadeh, "Continuous-wave, singly-resonant optical parametric oscillator source of vortex beams tunable in the ultraviolet," in Frontiers in Optics / Laser Science, OSA Technical Digest (Optical Society of America, 2018), paper JW3A.41.
5. **Varun Sharma**, S. C. Kumar, G. K. Samanta, and M. Ebrahim-Zadeh, "Tunable vortex beam, singly-resonant ultrafast optical parametric oscillator," in Conference on Lasers and Electro-Optics, OSA Terchnical Digest (online) (Optical Society of America, 2018), paper FTh3E.5.
6. **Varun Sharma**, S. C. Kumar, A. Aadhi, H. Ye, G. K. Samanta and M. Ebrahim-Zadeh, "Generation of vector vortex beam from doubly-resonant nanosecond optical parametric oscillator," 2018 Conference on Lasers and Electro-Optics (CLEO), San Jose, CA, 2018, pp. 1-2.
7. **Varun Sharma**, A. Aadhi, and G. K. Samanta, "Direct generation of tunable optical vortex dipole beams using a Gaussian beam pumped optical parametric oscillator," in Frontiers in Optics 2017, OSA Technical Digest (online) (Optical Society of America, 2017), paper FW2B.2.
8. **Varun Sharma**, A. Aadhi, and G. K. Samanta, "Tunable, vortex dipole doubly resonant optical parametric oscillator," in 2017 European Conference on Lasers and Electro-Optics and European Quantum Electronics Conference, (Optical Society of America, 2017), paper CD_P_9.
9. **Varun Sharma**, A. Aadhi, N. A. Chaitanya, and G. K. Samanta, "Multi-GHz femtosecond Airy beam radiation in higher-harmonic fractional cavity OPO," in Conference on Lasers and Electro-Optics, OSA Technical Digest (online) (Optical Society of America, 2017), paper JTh2A.90.
10. A. Aadhi, **V. Sharma**, and G. K. Samanta, "Generation of high power, higher order, continuous-wave optical vortices tunable in the mid-IR wavelength ranges," in Conference on Lasers and Electro-Optics, OSA Technical Digest (online) (Optical Society of America, 2018), paper STh3F.6

Contents

List of Figures

List of Tables

Chapter 1 Structured beams and non-linear optics

Optics plays a key role in our daily life, we observe colourful rainbows, sparkling diamonds and other endless magical optical phenomena. The process of understanding how light behaves and interacts with matter has a very rich history starting from the 300 B.C when various philosophers and scientists have started to explore the origin of light. The first basic experiments demonstrate how light originates, in which Empedocles explained that light originates from the eyes and falls on the object. Contrary to this point of view, Alhazen came with a different understanding that vision occurs when light reflected by objects gets detected by the eyes. With the progress in physics, understanding of how light behaves also improved with the evolution of major theories and experiments such as the Fermat's principle of least time, Diffraction of light, Huygens's principle of wavefront and Young's double-slit experiment. A major revolution in the field of optics came after Maxwell's analysis of light as an electromagnetic field and Einstein's understanding of light as quanta of particle known as photon. With an improved understanding of the fundamental nature of light and the recent advancements in the field of optics, it played a key role in the development of various scientific and commercial equipment such as lenses, binoculars and telescopes.

Einstein's theory of stimulated emission of identical photons from excited atoms in 1916 gave a conceptual method to produce coherent states of light. With the conventional understanding of Boltzman distribution in atoms, practical implementation of stimulated emission was difficult to demonstrate and took 30 years for the first implementation. In mid 20th century, the major breakthrough came in this field with the first conceptualization of Masers in 1951 by Charles H. Townes, and the suggestion of a resonator to produce coherent radiation in the microwave region. This experimental demonstration in 1954 lead to the curiosity of applying the same concept in the optical frequencies. Gould succeeded in theoretically inventing a cavity scheme to have coherent light output and came up with a name LASER for this device. In 1960 Maiman succeeded for the first demonstration of coherent emission of light through Ruby Laser. After the invention of the laser, it was common to say that this device is a solution looking for a problem. After the invention of the laser, Maiman suggested for their application in the field of telecommunication, industrial applications and probing matter for basic research. With time, coherent sources of radiation proved their application in the field of material processing [1], spectroscopy [2], communication [3] and in medical science [4]. Efforts have been made continuously to develop coherent sources with an improved spatial beam quality, output power, temporal, and spectral characteristics [5]. This chapter will focus on the discussion on the spatial shaping of coherent sources, their application, and the limitation of current methods and the solutions through nonlinear optics.

1.1 Spatial beam shaping

After 1960, the field of laser physics advanced very rapidly with the development of different types of lasers such as semiconductor lasers, gas lasers, dye lasers, and solid-state laser. In laser physics, the output modes of a laser beam is described by the solution of the paraxial wave equation inside a rectangular symmetric cavity given by the equation (1.1.1).

$$\begin{aligned} E(x,y,z) = {} & \left(\frac{2}{\pi n!m!}\right)^{1/2} 2^{-N/2}(1/w)\exp\left[\frac{-ik(x^2+y^2)}{2R}\right]\exp\left(\frac{-(x^2+y^2)}{w^2}\right) \\ & \times\exp\left[-i(n+m+1)\psi\right]H_n\left(\frac{x\sqrt{2}}{w}\right)H_m\left(\frac{x\sqrt{2}}{w}\right) \end{aligned} \quad \textbf{(1.1.1)}$$

where w is the beam waist, R, is the wavefront curvature, Ψ, is the Gouy phase, and H_n, H_m are Hermite polynomial of the order n and m respectively. With the advancement in the field of coherent sources, spatial structuring of the beam also found application in the various field. With the demonstration of spatial beam shaping into optical vortices through the resonator [6], the field of beam shaping has advanced with the generation of complex beam shapes, such as perfect optical vortices, Airy beam, vector beams, bottle beams, and various other spatial structure. These different spatial structures have proved their application and versatility in the field of quantum optics and information, material lithography, laser printing, and microscopy. In this thesis, we have covered the Gaussian beams, vortex beams, vector vortex beams, and Airy beam.

1.1.1 Gaussian beam

The Gaussian mode is the lowest order mode of the resonator and solution of the paraxial wave equation. For such beams, the complex field is given by equation (1.1.2), with Gaussian distribution of field in the transverse plane along the x and y-axis.

$$E(x,y,z)=E_0\frac{w_0}{w_z}\left(\frac{2}{\pi}\right)^{1/2}\exp\left[\frac{-ik(x^2+y^2)}{2R(z)}\right]\exp\left(\frac{-(x^2+y^2)}{w^2(z)}\right)\exp\left(-i(kz-\varphi(z))\right) \quad \textbf{(1.1.2)}$$

Where E_0 is the beam amplitude, *w(z)* is the beam waist along the propagation distance (*z*), w_0 is the minimum waist, and R(z) is the Gaussian beam wavefront curvature along the propagation direction. The Gaussian beam is characterized by the beam waist *w(z)* = $w(0)\left(1+\left(z/z_r\right)^2\right)^{1/2}$ and the radius of curvature, R(z) = z[1+(π $w_0^2/\lambda z$] which are function of the propagation distance, z. Rayleigh length is another parameter for the Gaussian beam characterization and defined as a region where the Gaussian beam has √2 times the minimum beam radius. Rayleigh length is given by $n\pi w_o^2/\lambda$, where w_o is the minimum beam waist, n is

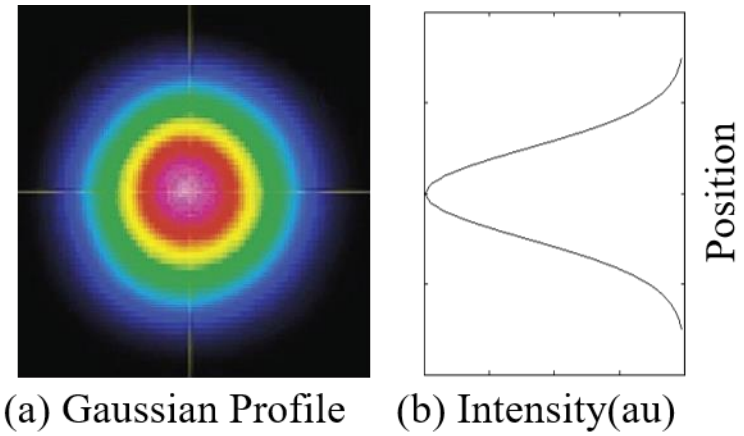

Figure 1.1. 2D Gaussian intensity profile and corresponding transverse line profile

the refractive index of the medium, and λ is the corresponding wavelength. At the minimum beam waist point, the radius of the curvature for a Gaussian beam is R = ∞ and has different values for the converging and diverging beam. Typically 2D intensity profile of the Gaussian beam is shown in Figure 1.1(a).

1.1.2 Optical vortex

Linear momentum of light is represented by the wave vector and points in the direction of propagation. Similarly, the light beam carries angular momentum with the polarization of the beam represented by the spin angular momentum, and also the beams with helical phase variation represent the orbital angular momentum in the beam. The study of optical vortices dates back to 1949 with Wolter's study of phase singularities appearance in the glass-air surface during total internal reflection. Two major breakthrough came into this field with the study of J F Nye and M V Berry titled as dislocations in wave train [7] in which they showed existence of screw-like dislocation in interfering ultrasound waves and the demonstration by the Allen et al showing the light beam with helical wavefront carries orbital angular momentum (OAM)[8]. Optical vortices are represented by the Laguerre Gaussian polynomial as shown in equation (1.1.3).

$$\begin{aligned} \mathrm{u}_{nm}^{\mathrm{LG}} = \left(\frac{2}{\pi n! m!}\right)^{1/2} \min(n,m)! \left(\frac{1}{\omega}\right) \exp\left[\frac{-\mathrm{i}k\mathrm{r}^2}{2\mathrm{R}}\right] \exp\left(-\left(\frac{\mathrm{r}^2}{\mathrm{w}^2}\right)\right) \exp\left[-i(n+m+1)\psi\right] \\ \times \exp[-il\phi](-1)^{\min(n,m)} \left(\frac{r\sqrt{2}}{\omega}\right) L_{\min(n,m)}^{n-m}\left(2\frac{r^2}{w^2}\right) \end{aligned} \quad \mathbf{(1.1.3)}$$

Here *exp(ilϕ)* represents the azimuthal phase variation in the beam, where, *l* is defined as the orbital angular momentum per photon in the beam. Optical vortices have helical wavefront with phase singularities at the center of the beam and results in doughnut-shaped intensity

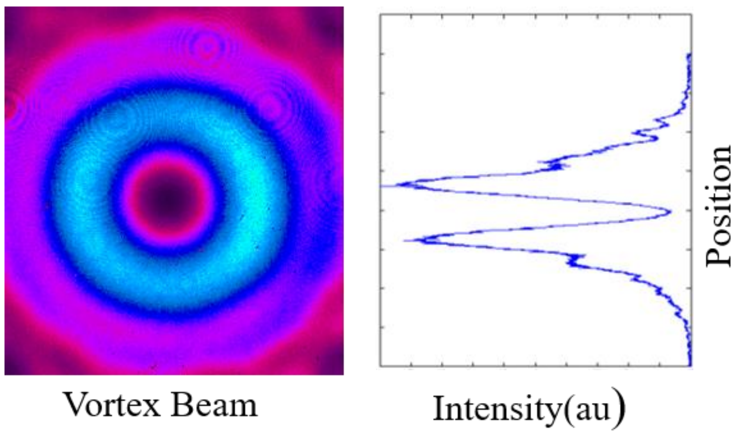

Figure 1.2. Vortex beam profile and corresponding transverse intensity distribution

distribution as shown in figure (1.2). For beams with only linear momentum, the wave vector of the beam is perpendicular to the phase front and lies along the optics axis of the beam. For beams with helical wavefront, there is a skew angle between the perpendicular to the phase front and optic axis of the beam. Unlike spin angular momentum, which has only two independent Eigen-states, OAM is represented in infinite-dimensional Hilbert space. The presence of OAM in optical vortices is utilized in various applications. With higher OAM value per photon, they surpasses polarization entanglement, which is limited to the low dimensionality, and demonstrates higher dimensional entanglement [9]. OAM content in the beam provides a way to multiplex the information and help in increasing the channel capacity for communication [10]. The doughnut shape of optical vortices is utilized in creating needle-like nanostructures in metal [11]. There are different methods used to generate optical vortices. For example, cylindrical lens based mode converters convert the higher-order HG modes into optical vortices [12], spatial light modulators [13] and spiral phase plates [14] provide a method to modulate the phase of the Gaussian beam into optical vortices. details of such methods are discussed in the upcoming section.

1.1.3 Vector vortex beams

Conventional laser beams have a uniform polarization state across the spatial profile of the beam. The manipulation of the state of polarization of the beam is done routinely in laboratories by using wave-plate retarders. However, recent developments have shown that the generation of a new class of beams with spatially varying polarization, known as vector beams. To study the polarization state of such beams, the Poincare sphere is utilized. Different points on the Poincare sphere represent different polarization states of the beam. With, poles represent circularly polarized beams and equatorial lines represent linear polarization. Vector beams are generated by the superposition of two orthogonal higher-order HG modes with orthogonal polarization and known as cylindrical vector beams given in equation (1.1.4).

$$\mathrm{E}_r = \mathrm{HG}_{01}\overrightarrow{e_x} + \mathrm{HG}_{10}\overrightarrow{e_y} \qquad \textbf{(1.1.4)}$$

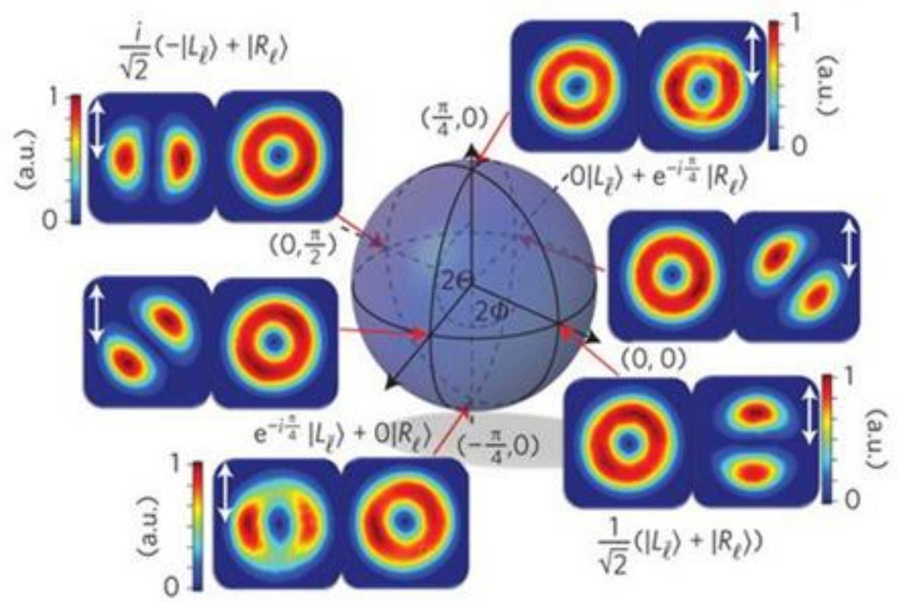

Figure 1.3. Vector beam representation on higher order poincare sphere

However, the superposition of two higher-order LG modes with opposite topological charge and orthogonal polarization is known as vector vortex beams. The total angular momentum (spin + orbital) of vector vortex beams is represented on the higher-order Poincare sphere, with the radius of the sphere representing the OAM content in such beams. An example of a higher-order Poincare beam [15] is shown in Figure 1.3. The varying polarization across the doughnut-shaped spatial profile of a vortex beam is illustrated in Figure 1.3. Due to the presence of orthogonal modes and polarization in the vector beam can have either radial varying polarization or azimuthally varying polarization depending upon the phase difference between the two beams. Some examples are shown in Figure 1.4.

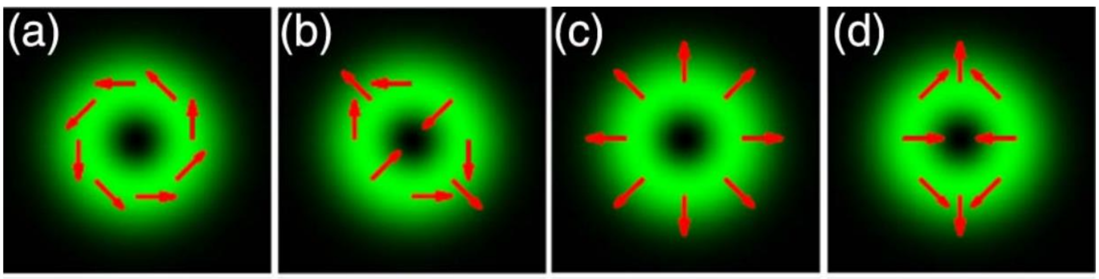

Figure 1.4. Polarization distribution in vector beams

As compared to homogeneously polarized beams, vector beams have unique features, and the presence of non-uniform transverse polarization patters along with the vortex spatial profile is of great interest for a variety of applications. It can be shown that radially polarized beams can be focussed to a smaller beam waist as compared to scalar beams [16]. The tight focusing leads to needle-shaped electromagnetic fields. Thus, radially polarized beams are being used in material science to design nanostructures [17] with high precision and very small feature sizes. Recently, it was shown that much higher trapping efficiencies and smaller particles can be trapped using vector-vortex beams as compared to conventionally uniformly polarized beams [18]. In classical communication, the polarization and orbital angular momentum of vector-vortex beams offer two independent degrees of freedom, thus offering several multiplexing opportunities. At the single-photon level, such states are non-separable in their polarization and orbital angular momentum basis leading to better security and efficiency in quantum communication protocols.

1.1.4 Airy beams

Light beams of the conventional lasers, propagates in a straight line and have divergence with propagation. On the other hand, Airy beams showed emergent properties of acceleration in a curved trajectory, non-divergence with propagation and self-healing of the beam. In 1979, Berry and Balazs's work showed a non-spreading Airy wave packet solution for the Schrodinger equation of free particle [19]. It took three decades for the experimental realization of such a solution. In 2007, G. A. Siviloglou et al [20] reported the first experimental demonstration of Airy wave packet in optics. In Berry and Balazs's work, they considered an infinite extended Airy wave packet as a solution, with properties of non-divergence for an infinite distance. In experimental schemes, these beams are truncated and have a finite spatial extension. Due to truncation of the beam, the Airy properties last for a limited distance and the truncated Airy wave function is represented by equation (1.1.5.)

$$\phi(\xi,s)=\mathrm{Ai}\left(s-(\xi/2)^2+ia\xi\right)\exp\left[\left(as-a\xi^2/2\right)-i\left(\xi^3/12-a^2\xi/2-s\xi/2\right)\right] \quad \textbf{(1.1.4)}$$

where ϕ is the electric field envelope, $s = x/x_0$ represents a dimensionless transverse coordinate, x_0 is an arbitrary transverse scale, $\xi = z/k\, x_0^2$ is a normalized propagation distance, and a is the truncation factor [20]. The Airy beam has multiple lobe structure as shown in Figure 1.5, these lobes have symmetric intensity distribution in the transverse plane with line profile as shown in figure 1.5 along the central bright lobe. With propagation, the size of these lobe structures stays the same and they propagate in a curved trajectory. To realize the Airy beam in the lasers, one needs to make a cubic phase variation in the beam, then with the help of a Fourier lens it results in the Airy beam profile at the Fourier plane. One can realize the simultaneous generation of one-dimensional as well as two-dimensional Airy beam in the lab as demonstrated by R. S. Grewal et al [21] by making a suitable phase variation in the single beam itself. Due to interesting properties of acceleration, self-healing, and non-divergence, the Airy beam has found various applications in the field of light-sheet microscopy [22], curved plasma guiding [23] and micromachining in a curved channel [24]. With the new emergent application of the Airy beam, there are different solutions available for their generation. The conventional methods of Airy beam generation includes the holographic techniques and diffractive elements.

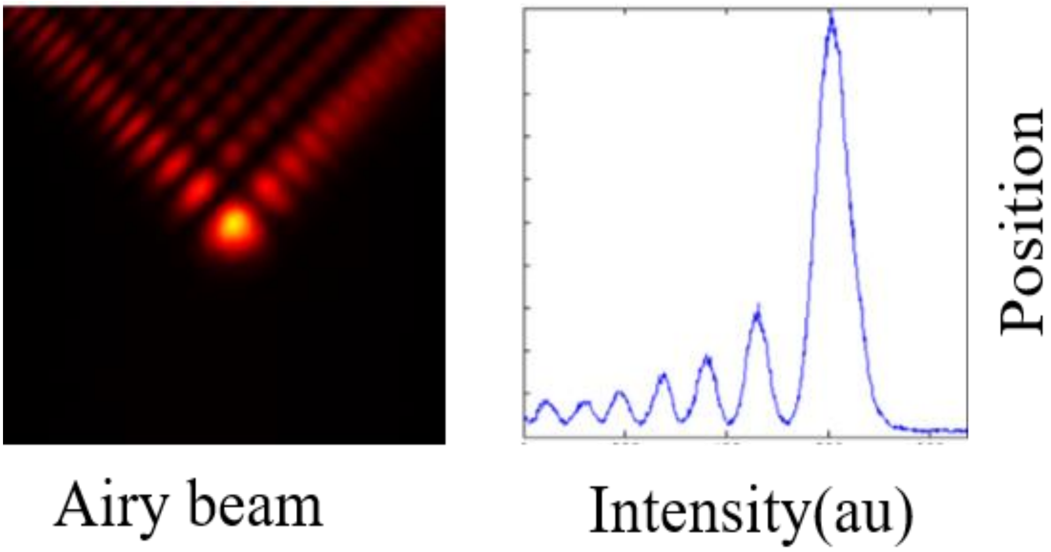

Figure 1.5. Two dimensional Airy beam and corresponding line profile across central lobe

In the next section, we will be discussing different methods for the generation of such spatial structure from the laser beams.diffractive elements.

1.1.5 Methods of beam shaping

There are different methods available for the spatial beam shaping of coherent sources. The active method includes direct generation from the laser resonator itself, while other methods are based upon the mode converters such as spatial light modulators and phase plates.

1.1.5.1 Spatial light modulators

Spatial light modulator is a device used to modulate the amplitude and phase of the light beams. Current methods to modulate spatio-temporal properties of the light beam by SLM are based upon either MEMS (microelectromechanical system) or LCD (liquid crystal-based). The LCOS-SLM (liquid-crystal-on-silicon spatial light modulator) are reflection type phase spatial light modulators based on liquid crystal on silicon (LCOS) technology. In this technique, an electrical signal is used to modulate the liquid crystal in the desired manner to modulate the input light. LCOS based SLM utilizes the technique of computer-generated hologram, which imprints the grating structure into SLM to modulate the phase and amplitude of the beam. For example, to generate optical vortices from a Gaussian beam, a forked grating is used to imprint on the SLM, which results in the generation of optical vortices of respective order as shown in Figure. 1.6. They offer a great technique to achieve various spatial structure depending upon the input given to SLM. This technique is based upon the liquid crystal and voltage provided to each of them, which limits the input power usage. In reflection type SLM, use of dielectric

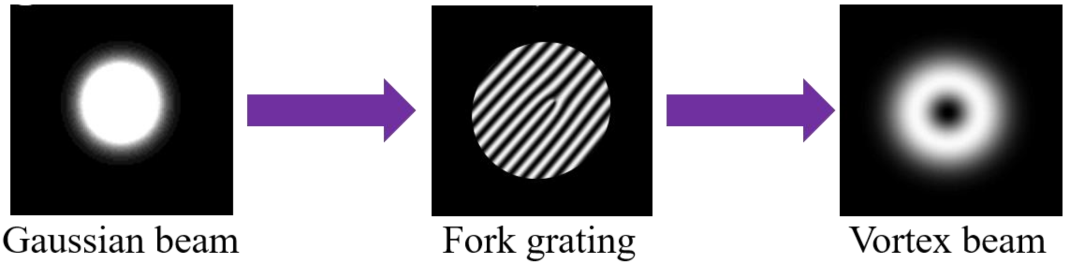

Figure 1.6. Spatial light modulator method for structured beam generation

mirror after the LCD limits the SLM operation within 50 – 100 nm of central wavelength operation. To overcome the limitations of high power beam shaping, different dielectric phase elements are used.

1.1.5.2 Dielectric phase elements

Various dielectric elements are used for beam shaping of coherent sources. Due to the high damage threshold of the medium, they are highly useful in the generation of high power structured beams. One example of such an element is a spiral phase plate (SPP) [14]. Spiral phase plates are designed with thickness variation in the azimuthal plane such that the input beam sees a helical phase variation, as shown in Figure 1.7. For a beam with plane wavefront, this thickness variation results in the generation of a helical wavefront or optical vortices. Depending upon the requirement of topological charge in the beam one can design these phase elements for the desired output.

Another type of such element is the cubic phase mask (CPM), which has a cubic phase grating imprint, as shown in Figure 1.7. Passing of a Gaussian beam through CPM results in the cubic phase pattern in the beam, and the Fourier transform of this pattern results in the generation of an Airy beam. These phase elements have a very high damage threshold and are useful for the generation of high power structured beams. However, due to material refractive index dependence on the wavelength, these elements are highly wavelength-specific and limit their functionality beyond the central wavelength region.

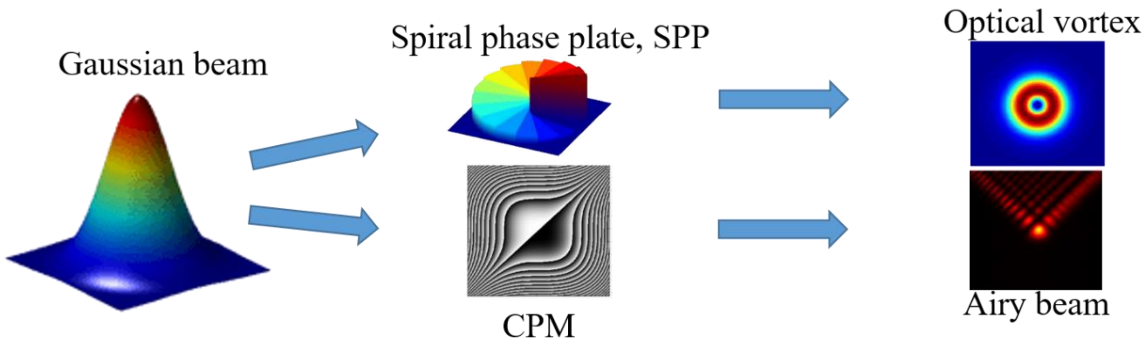

Figure 1.7. Dielectric phase element method for generation of different spatial structure.

Most of the commercially available lasers have certain drawbacks in terms of limited or no tunability, high cost, and complicated design. Some of the shortcomings can be easily overcome by choosing proper system design and laser gain medium. However, the generation of wide tunable radiation from a laser itself is limited by the availability of suitable gain medium. Such unavailability of gain medium restricts access to many wavelength regions ranging from the UV to mid-IR using lasers. Additionally, due to the normal dispersion, the phase elements used to generate structure beams are wavelength selective. For example, the spiral phase plate used to generate optical vortices at 532 nm cannot be used for other wavelengths. While liquid crystal-based spatial light modulators can have higher wavelength coverage but such systems have lower damage threshold. All these limitations restrict the generation of structured beams at a wide range of wavelengths using lasers. To achieve the other frequency regions, which are not accessible through conventional laser, nonlinear optics plays a key role. With the help of nonlinear optics, one can generate such spatial structures in a broader wavelength region.

1.2 Nonlinear optics

The invention of the lasers opened new frontiers for the investigation of higher-order optical phenomena. With properties of high coherence and high intensities of pulsed ruby laser, P. A. Franken et al. demonstrated the first higher-order optical harmonic generation in 1961 [25]. This was the first study in the field of nonlinear optics and paved the way for the evolution of non-linear optics. Field of nonlinear optics deals with the study of various optical phenomena, which arises from higher-order nonlinearities in the medium. To observe such a process, high intense field interaction with the matter is required. Though it was known that material can exhibit higher-order nonlinearities much before the invention of lasers, but due to the unavailability of such sources, there were no experimental studies of non-linear optics before 1960. The invention of laser provided a platform and source to study such higher-order nonlinear optical phenomenon in different materials. With the help of high intense laser sources, materials started to show higher-order nonlinear phenomenon. In this discussion, we will neglect permanent dipole moments in the medium and focus on the induced dipole moment due to the applied electric field. In the presence of an external field, the electric displacement vector is given by equation 1.2.1, where, ε is the epsilon tensor, $\vec{E}$ is the applied electric field and $\vec{P}$ is the dipole moment per unit volume. This dipole moment induces due to the charge separation in the medium because of the applied electric field.

$$\vec{D} = \varepsilon\vec{E} + \vec{P} \tag{1.2.1}$$

This induced dipole moment per unit volume is dependent upon the input field and represented by the equation 1.2.2. For most of the physical scenarios, input fields are not very intense and $\vec{P}$ is linearly dependent on the input electric field. In the linear regime, applied electric fields are very small and we can simplify the interaction of light with the matter as simple harmonic oscillator system [26] which results in the linear component of dipole moment per unit volume. For high input electric field, as compared to the interatomic electric fields in the medium, this approximation fails and anharmonicity in the medium results in higher-order terms contribute toward the dipole moment per unit volume as shown in equation 1.2.2.

$$\begin{aligned} \vec{P}_i &= \varepsilon_0\left(\chi_{i,j}E_j + \chi^{(2)}_{i,j,k}E_jE_k + \chi^{(3)}_{i,j,k,l}E_jE_kE_l + \ldots\right) \\ \vec{P}_i &= \vec{P}_L + \vec{P}_{NL} \end{aligned} \tag{1.2.2}$$

Where $\varepsilon_0\chi^{(2)}_{i,j,k}$, $\varepsilon_0\chi^{(3)}_{i,j,k,l}$ are second-order and third-order susceptibility tensor respectively. The induced polarization, $\vec{P}_i$ is a combination of linear dipole moment per unit volume ($\vec{P}_L$) and nonlinear dipole moment per unit volume ($\vec{P}_{NL}$) which contribute only when the applied electric field becomes very strong (~10^7 V/m). Equation 1.2.2 is written in the tensor notation and can be further reduced to scaler form by making appropriate assumptions. Most of the materials $\chi^{(2)}_{i,j,k}$ and $\chi^{(3)}_{i,j,k,l}$ have values in the order of 10^{-12} and 10^{-24} respectively and require high intense electric field to see the output. Nonlinear polarization plays a key role in describing various physical phenomena due to its dependence on time-varying nature of the applied electromagnetic field. This nonlinear polarization acts as a source term in the Maxwell equation for the electromagnetic waves, as given in equation 1.2.3 [26].

$$\nabla^2\vec{E} - \mu_0\varepsilon\frac{\partial^2\vec{E}}{\partial t^2} = \mu_0\frac{\partial^2\vec{P}_{NL}}{\partial t^2} \tag{1.2.3}$$

1.2.1 Second-order nonlinear effects

Second-order nonlinear optics deals with the physical phenomenon arise due to the second-order nonlinear susceptibility ($\chi^{(2)}$) term in the nonlinear polarization description.

$$\vec{P}_i = \varepsilon_0 \left(\chi_{i,j} E_j + \chi^{(2)}_{i,j,k} E_j E_k \right) \qquad \textbf{(1.2.4)}$$

$\chi^{(2)}$ is third-order tensor which exists only in non-centrosymmetric materials in which there is no inversion symmetry. Due to the second-order dependence of dielectric polarization on the applied field, medium with inversion symmetry does not have a $\chi^{(2)}$ value [27]. In nonlinear optics literature, $\chi^{(2)}$ is defined by $d_{eff} = \frac{\chi^{(2)}}{2}$ which directly defines the strength of the second-order nonlinear phenomenon. By using symmetries of the medium, the d tensor can be reduced

$$\begin{pmatrix} P_x \\ P_y \\ P_z \end{pmatrix} = 2\varepsilon_0 K \begin{bmatrix} d_{11} & d_{12} & d_{13} & d_{14} & d_{15} & d_{16} \\ d_{21} & d_{22} & d_{23} & d_{24} & d_{25} & d_{26} \\ d_{31} & d_{32} & d_{33} & d_{34} & d_{35} & d_{36} \end{bmatrix} \begin{pmatrix} E_x^2 \\ E_y^2 \\ E_z^2 \\ E_y E_z + E_z E_y \\ E_x E_z + E_z E_x \\ E_x E_y + E_y E_x \end{pmatrix} \qquad \textbf{(1.2.5)}$$

to 18 value and represented by a tensor contracted to 3x6 matrix. By using d tensor and applied electric field, most general expression of second-order nonlinear polarization can be written as shown in equation (1.2.5). Coupling between second-order nonlinear polarization and applied electric field results in various second-order phenomena such as second harmonic generation, sum-frequency generation, difference frequency generation, and parametric processes. Details of such processes are discussed in the upcoming sections.

1.2.1.1 Second harmonic generation

Second-harmonic generation (SHG) was the first experimental demonstration [25] of the second-order nonlinear optics, in which laser of wavelength at 693 nm was frequency-doubled to 347 nm. For the simplified understanding of SHG, we have considered a high intense input

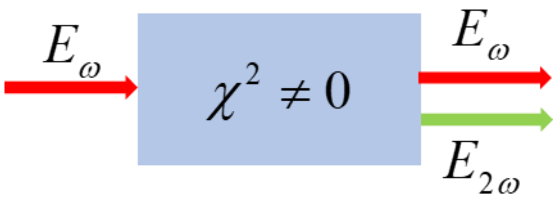

Figure 1.8. Schematic of the second harmonic generation

field oscillating at frequency ω which, results in the second-order nonlinear polarization, as shown in equation (1.2.6) at frequency 2ω.

Second-order polarization term at frequency 2ω results in the dipole oscillation at frequency 2ω, which gives rise to a new electric field inside the medium with frequency 2ω. As shown in Figure 1.8. SHG is a coherent process of the generation of new wavelengths that is not accessible through conventional laser, for which green pointer is a classic example.

Maxwell's equations for the propagation of electric fields at frequency ω and 2ω inside the nonlinear medium and interaction between these two electric fields are given by the following equation.

$$\begin{aligned} \nabla^2 \vec{E}^{(\omega)} - \mu_0 \varepsilon \frac{\partial^2 \vec{E}^{(\omega)}}{\partial t^2} &= \mu_0 \frac{\partial^2 \vec{P}_{NL}^{\omega}}{\partial t^2} \\ \nabla^2 \vec{E}^{(2\omega)} - \mu_0 \varepsilon \frac{\partial^2 \vec{E}^{(2\omega)}}{\partial t^2} &= \mu_0 \frac{\partial^2 \vec{P}_{NL}^{2\omega}}{\partial t^2} \end{aligned} \quad \textbf{(1.2.7)}$$

The above equation shows, the electric field generated at frequency ω induces nonlinear polarization at frequency 2ω. This induced polarization generates electric field at frequency 2ω which interacts with the electric field at frequency ω through the nonlinear interaction. Variation of the electric field at frequency 2ω with propagation distance and its dependence on the input field is governed by the equation, as given below.

$$\frac{dE_{2\omega}}{dz} = \frac{i\omega d}{cn_2} E_\omega^2 e^{-i\Delta kz} \quad \textbf{(1.2.8)}$$

Equation 1.2.8 is derived under the condition of low pump depletion and contains second-order nonlinear coefficient of the medium (*d*) with the refractive index of the medium (n_2) for second harmonic wave, Δk determines the phase mismatch between fundamental and second harmonic wave. Section 1.2.3, presents more discussion on phase mismatch and methods for efficient phase matching for the generation of the second harmonic process

1.2.1.2 Sum frequency generation

Sum frequency generation (SFG) is a similar process to the SHG process. In both of these processes, two photons energies are added to generate a new photon with higher energy. In the case of SHG initial photons have the same energy, while in SFG two input photons have different energies. To understand the SFG process, we can consider a second-order nonlinear medium with two input electric fields at frequencies, ω_1 and ω_2. Since the second-order process has square dependence on the input field, we are only considering real components of the electric field as given in equation (1.2.9).

$$E = E_1 e^{-i\omega_1 t} + E_2 e^{-i\omega_2 t} + c.c \qquad \textbf{(1.2.9)}$$

In the presence of two electric fields with two different frequencies, second-order nonlinear

$$\begin{aligned} P_{NL} = \chi^{(2)} & \left[E_1^2 e^{-2i\omega_1 t} + E_2^2 e^{-2i\omega_2 t} + 2E_1 E_2 e^{-i(\omega_1+\omega_2)} + 2E_1 E_2^* e^{-i(\omega_1-\omega_2)} + C.C \right] \\ & + 2\chi^{(2)} \left[E_1 E_2^* + E_1^* E_2 \right] \end{aligned} \qquad \textbf{(1.2.10)}$$

polarization is given by equation (1.2.10). This nonlinear polarization contains different terms oscillating at different frequencies as shown in equation (1.2.10). In this second-order nonlinear polarization, the term corresponding to the product of input electric fields results in the oscillation of dipoles in the medium with new frequencies which are the sum of initial input frequencies ($\omega_1 + \omega_2$).

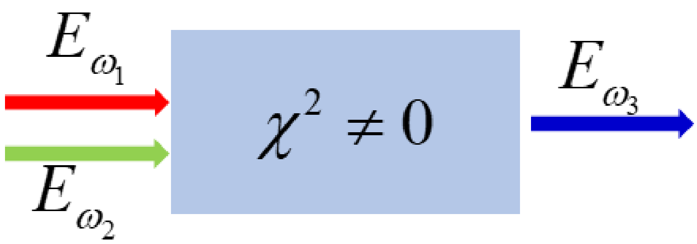

Figure 1.9. Schematic of sum frequency generation process

These dipole oscillations result in the generation of new EM waves with frequencies $\omega_{1}+\omega_{2}$ as shown in Figure (1.9). SFG process is utilized to go from the near-IR or visible region to UV [28] wavelength region in which conventional lasers do not operate.

1.2.1.3 Difference frequency generation

Difference frequency generation (DFG) is another second-order nonlinear process used to generate longer wavelengths. In equation (1.2.10), the polarization term corresponding to the product of electric fields with the difference of two input frequencies is describing the DFG process. In this process, pump photons of energy ω_1 interact with another input beam at frequency ω_2 and result in the generation of new photons at frequency $\omega_1 - \omega_2$ as shown in Figure 1.10.

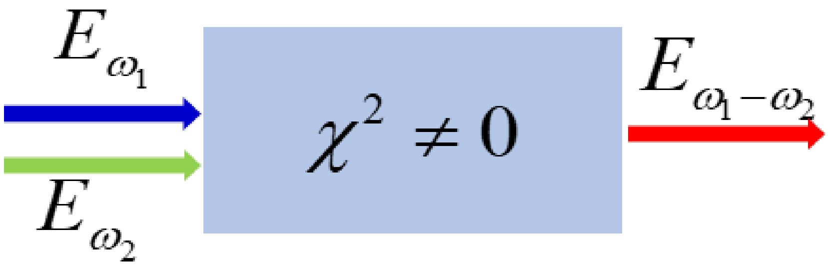

Figure 1.10. Schematic of difference frequency generation process

During this process, the number of interacting photons with frequency ω_2 with high intense pump at frequency ω_1, results in the further generation of the same number of photons at frequencies ω_2 and $\omega_1 - \omega_2$. Since, the number of input photons are enhanced during this process, DFG is also known as optical parametric amplification. DFG based schemes are utilized for the generation of new wavelengths in mid-IR and terahertz (THz) domain [29], which are difficult to access through the conventional methods. In the case of equal input frequencies, the process is termed as an optical rectification which results in a dc charge across the nonlinear medium.

1.2.1.4 Parametric processes

The parametric process is opposite to the second-order based frequency upconversion process such as SHG or SFG. In the parametric process, input pump photon (ω_p) splits into two daughter photons at lower energies, conventionally photon having higher frequency is known as signal (ω_s) and photon with lower frequency is known as idler (ω_i). Due to the presence of three interacting photons in this process, it is also known as three-wave mixing process. This process is also known as spontaneous parametric down conversion (SPDC) and parametric fluorescence in literature. This process does not involve any real energy level of the medium and originates from the quantum mechanical nature of the process [30]. With the experimental demonstration of this process in 1970 [31], it has proved its applicability as a single-photon source for quantum optics and quantum information studies.

During the splitting of the pump photon into two photons, input pump energy is distributed in the down-converted photons. Using this process and utilizing the condition of energy and momentum conservation, the new wavelengths can be achieved. This generation of new wavelengths is done through parametric amplification in a feedback mechanism to make an oscillator using this process, which is known as optical parametric oscillators (OPOs). Such devices are utilized to generate coherent radiations over a broad range of wavelengths. OPOs have proved their versatility of generating high powers with broad wavelength coverage in all time scales ranging from continuous-wave to the ultrafast domain. In the next chapter, we have discussed the design mechanism and different requirements to make a tunable source of coherent radiation.

1.2.2 Conservation laws

The second-order nonlinear process is a three-wave interaction phenomenon, which results in the generation of new wavelengths depending upon the interacting beams. In this three-wave mixing process, either two photons combine to generate one photon of higher energy or one photon splits into two daughter photons with lower energies. During all such processes, energy and total momentum are conserved, as shown in equation (1.2.11). Energy conservation can be understood from Figure 1.11(a), with the virtual energy level diagram of the three-wave interaction process. Figure 1.11(a) represents one photon of frequency ω_3 splits into two lower energy photons of frequency ω_1 and ω_2 through intermediate virtual energy levels represented by the dotted line. Linear momentum conservation is known as the phase-matching condition. For efficient interaction among interacting waves, they need to have equal phase velocities inside the medium. This condition is known as the phase-matching condition. Similar to linear

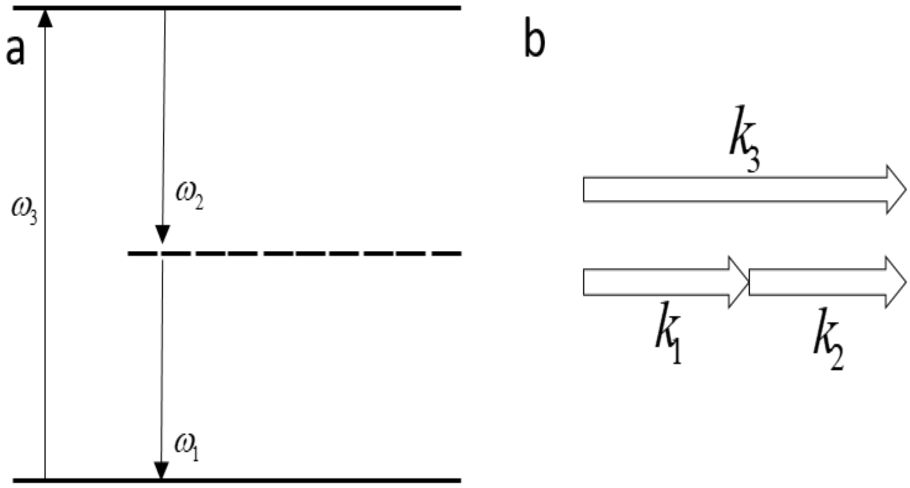

Figure 1.11. Conservation laws during second order process, (a): energy conservation, (b): momentum conservation

momentum, orbital angular momentum (OAM) is also conserved during second-order processes [32]. During this process, the input pump beam OAM transfer to the resultant output. During OAM conservation, one should keep in mind that OAM of the single-photon is always integral multiple and cannot split into a fraction among the generated pairs. Energy and OAM conservation in the second-order process does not need a special method for efficient transfer of energy among the interacting waves. However, for better efficiencies in this process, one needs special methods for phase matching. Physically this means that for coherent transfer of pump energy into new frequencies, they should have minimum phase mismatch inside the medium. On the other hand, we know that the refractive index of the medium is a wavelength-dependent quantity, which increases with an increase in the frequency. To overcome this hurdle of phase mismatch among interacting beams, special techniques, such as birefringent phase-matching [33] and quasi phase-matching [34] are widely used for the coherent transfer of energies between the interacting beams.

$$\begin{aligned} \omega_3 &= \omega_1 + \omega_2 \\ k_3 &= k_1 + k_2 \\ l_3 &= l_1 + l_2 \end{aligned} \tag{1.2.11}$$

1.2.3 Phase matching

The method of momentum conservation in the nonlinear processes is known as the phase-matching condition. The requirement of phase matching in a second-order nonlinear process can be understood from the output power of the second harmonic wave in the SHG process. Variation of 2ω field along the crystal length depends upon the square of the input pump field and phase mismatch between the pump and second harmonic waves as given in equation (1.2.8) [26]. From this equation, one can calculate the output intensities and power in the SHG process as given in equation (1.2.12).

$$I_{2\omega} = \frac{2\omega^2 d_{eff}^2 L^2 I_\omega^2}{\varepsilon_0 n_\omega^2 n_{2\omega} c^3} \sin c^2 \left[\frac{\Delta kl}{2} \right] \qquad \textbf{(1.2.12)}$$

Where $\Delta k = k_{2\omega} - 2k_\omega$ is the phase mismatch between the interacting waves, d_{eff} is the nonlinear coefficient of the medium, *L* defines the length of the crystal, n_ω and $n_{2\omega}$ are corresponding refractive index at frequencies ω and 2ω respectively. From the above equation for output intensity in the SHG process, output power depends upon the phase mismatch between the pump and SH wave. To achieve maximum output power, there should be zero mismatch, $\Delta k = 0$, between pump and second harmonic field. Output intensity falls down rapidly with Δk variation from zero and has a bandwidth (intensity fall by 1/4) π / l. This critical dependence of phase mismatch for efficient energy exchange in three-wave interaction processes, achieving zero phase mismatch is a necessary condition. To achieve zero phase mismatch for efficient interaction, the technique of birefringent phase-matching and quasi phase-matching is used in a second-order nonlinear medium.

1.2.3.1 Birefringent phase matching

One of the fundamental techniques used for achieving phase-matching utilizes the birefringence of the medium and known as birefringent phase-matching. Birefringence is the property of anisotropic medium where different polarization has different refractive index inside the medium. This variation in refractive index with polarization is utilized to design the anisotropic medium in such a way that different interacting waves have different polarization but the same phase or group velocity inside the medium. For achieving this, interacting beams are sent at specific angles to the optic axis of the medium, which results in a zero-phase mismatch between the interacting beams and helps in the transfer of energy between the interacting beams. These birefringent medium are divided according to the number of optic axis in the medium into the uniaxial and biaxial medium. Depending upon the epsilon tensor properties, materials are characterized into two categories- isotropic and anisotropic media. In anisotropic mediums, epsilon tensor reduces to a diagonal matrix in principal axis with three elements, $\varepsilon_{xx}, \varepsilon_{yy}, \varepsilon_{zz}$, if, $\varepsilon_{xx} = \varepsilon_{yy} \neq \varepsilon_{zz}$ the medium is known as uniaxial and for $\varepsilon_{xx} \neq \varepsilon_{yy} \neq \varepsilon_{zz}$ the medium is known as a biaxial medium. In a uniaxial medium, there is only one optic axis along which one can satisfy the phase-matching condition, while in a biaxial medium there are two optic axes in which phase matching conditions can be satisfied. In this thesis, we have utilized only uniaxial medium and we will limit our discussion only to uniaxial mediums. In uniaxial mediums, the birefringence is based upon two different refractive indices, the ordinary (n_o) and the extraordinary (n_e) index of refraction. In the ordinary index of refraction, the electric field polarized perpendicular to the optical axis, beam propagating in this direction is known as the ordinary ray and have a same refractive index (n_o), irrespective of angle with the propagation direction. While in the case of an extraordinary beam, the polarization of the propagating beam lies in the plane of the optic axis. In the case of extraordinary beams, the refractive index face by the beam is dependent upon the angle with the optic axis and given by $n_e(\phi)$. By choosing a suitable angle with propagation direction, one can make the refractive index at extraordinary polarization and ordinary polarization same for two different wavelengths to satisfy the phase-matching condition. Birefringent phase matching is further divided into two categories, Type 1 and Type 2. In Type 1 phase matching, pump photon has orthogonal polarization as compared to the generated photons. Whereas, in Type 2 phase matching, generated photons have orthogonal polarization among each other.

1.2.3.2 Quasi phase matching

The second approach to phase match the interacting beams inside a nonlinear medium is known as the quasi phase-matching (QPM). It is clear from the term itself that in this technique, it does not perfectly cancel the phase mismatch between the interacting beams. There is a small mismatch between the phase of the interacting beams and represented by Δk. For understanding, we can consider a simplified case of SHG. In this process, pump beam propagates inside the medium and generates energy with twice the frequency. After propagation of small length corresponding to coherence length (l_c), the pump beam acquires a π phase as compared to the second harmonic wave. This results in the backward energy transfer from the second-harmonic to the pump beam. To make the energy transfer process efficient with propagation, an additional phase shift of π is required after coherence length (l_c). This will enable the coherent transfer of pump energy back to the second-harmonic wave. To realize this additional phase modulation of π, method of periodical polling is used in the nonlinear medium. In this technique, after coherence length, the crystal axis of the medium is oriented in the opposite direction, this changes the sign of the effective nonlinear coefficient. This helps in canceling the effective mismatch in the three-wave interaction and helps in the effective transfer of the pump energy. The modulation of the crystal axis is done in a ferroelectric medium with the help of externally applied voltage. The conversion efficiency of QPM method is lower than that of BPM, if we consider the same nonlinear material, with the same effective nonlinear coefficient. QPM technique is versatile with no dependence on polarization of interacting waves, enables the use of long crystal length and one can selectively choose the desired d_{eff} coefficient of the medium which is not possible using BPM technique.

1.3 Aim of the thesis

Structured beams have proved their application in the field of material lithography, microscopy, quantum information and communication, and spectroscopy. Current techniques for the generation of spatial structures over a broad range of wavelengths are limited due to the laser's output wavelengths over a limited range or fixed wavelength operation of phase elements due to the normal dispersion. On the other hand, with limited tunability available with SLM, the generation of structured beams with high power is difficult. On the other hand, OPOs have demonstrated the generation of tunable coherent sources from UV to mid-IR with high average power, stable spectrum and good beam qualities in all time scales. OPOs can serve as a great platform to overcome the limitation of the existing methods and can help in the generation of high power tunable coherent sources of radiation with spatial engineered structures. The objective of this thesis is to develop structured beam sources of coherent radiation over a broad range of wavelengths with the help of optical parametric oscillators. In this thesis, I have covered and studied the following works:

1. Direct generation of optical vortices by using doubly resonant continuous-wave and ultrafast OPOs.
2. Generation and study of OAM exchange in singly resonant picosecond OPOs in near-IR and mid-IR spectral domain.
3. Generation of tunable optical vortices in the ultraviolet spectral domain by using intracavity SFG of a cw OPO.
4. Generation of tunable vector vortex beams by using doubly resonant nanosecond OPO.
5. Generation of multispatial structured beams with a wavelength tunability using a single picosecond OPO.

This thesis contains 8 chapters. It also includes the introduction of spatial beam shaping, methods of their generation and nonlinear optics. The first chapter is a broad overview of the basic motivation behind my thesis work. To achieve the goal of my thesis, we have used OPOs as a platform, for better understanding. Therefore we have provided the basic design mechanisms for the building of an OPO in chapter 2. After preparing the recipe for the thesis work in the first two chapters, we have presented my experiments completed during my thesis tenure in subsequent chapters. The third chapter focused on the direct generation of optical vortices from Gaussian pumped OPOs in CW as well as ultrafast time domain. In chapter 4, we have discussed the generation of high power, higher-order optical vortices in near-IR as well as the mid-IR spectral region by using ultrafast OPO. In chapter 5, we have focus on the generation of optical vortices in the UV region by using intracavity SFG configured OPO. Chapter 6, we have changed our gear from scaler beams to vector beams and presented a scheme to generate tunable vector-vortex beam from a doubly resonant nanosecond OPO. After gaining experience on structured beam OPO, we focused on developing a single system which can provide multiple spatial structure with broad wavelength coverage. The results of this work are presented in chapter 7. In chapter 8 we have summarised my thesis work and discussed about future possibilities to generate different spatial structures by using CW as well as ultrafast OPOs.

Chapter 2 Optical parametric oscillators and cavity design

2.1 Three wave interaction

In the last chapter, we have discussed second-order nonlinear processes such as SHG, SFG, and parametric processes. In this section, we will discuss the description of the parametric process and optical parametric oscillators (OPOs). In OPOs, discussion on their design mechanisms and dependence on the various parameters is presented. For this discussion we are going to consider input laser beam as a pump source which is represented by electromagnetic (EM) wave of frequency ω_p, down-converted photon of higher energy is considered as signal and is represented by EM wave of frequency ω_s and photon with lower energy as idler and is represented by EM wave of frequency ω_i. This is the common convention used to represent three waves involved in the process. Since the second-order nonlinear process is a three-wave mixing process and all the interacting waves are coupled to each other, so this process is represented by the coupled Maxwell equations as discussed in the last chapter. To understand the three-wave interaction process, we have considered a nonlinear medium with all three

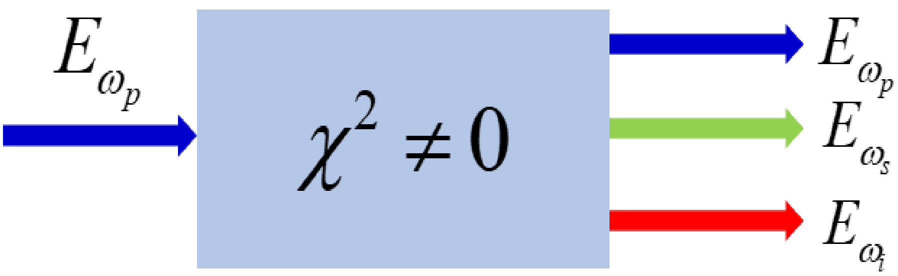

Figure 2.1. Schematic representation of second order parametric down conversion process.

waves inside the medium as shown in Figure (2.1). In this process, the energy of the pump photon splits into signal and idler such that $\omega_p = \omega_s + \omega_i$. The medium considered here is a homogeneous, non-magnetic with no free charges. In the second-order nonlinear processes, nonlinear polarization results in the generation of new frequencies. All three waves are represented by equation (2.1.1) inside this medium.

$$
\begin{aligned}
E(\omega_p) &= \frac{1}{2}\left[E_p e^{i\left(k_p z-\omega_p t\right)} + c.c\right] \\
E(\omega_s) &= \frac{1}{2}\left[E_s e^{i\left(k_s z-\omega_s t\right)} + c.c\right] \\
E(\omega_i) &= \frac{1}{2}\left[E_i e^{i\left(k_i z-\omega_i t\right)} + c.c\right]
\end{aligned}
\qquad \textbf{(2.1.1)}
$$

Each wave will induce a second-order nonlinear polarization inside the medium, given in equation (2.1.2).

$$
\begin{aligned}
P_{NL}(\omega_p) &= \frac{1}{2}\varepsilon_0 d\left[2E_s E_i e^{i\left[\left(k_s+k_i\right)z-\omega_p t\right]} + c.c\right] \\
P_{NL}(\omega_s) &= \frac{1}{2}\varepsilon_0 d\left[2E_p E_i^{*} e^{i\left[\left(k_p-k_i\right)z-\omega_s t\right]} + c.c\right] \\
P_{NL}(\omega_i) &= \frac{1}{2}\varepsilon_0 d\left[2E_p E_s^{*} e^{i\left[\left(k_p-k_s\right)z-\omega_i t\right]} + c.c\right]
\end{aligned}
\qquad \textbf{(2.1.2)}
$$

For simplified analysis of the interaction of these three waves in a nonlinear medium, we have considered that there is no phase mismatch in the system which can be achieved through birefringence phase-matching or quasi phase-matching. Under no phase mismatch, we can derive the coupled wave equation under the effect of nonlinear polarization as the source term in the medium. The generalized Maxwell equation for these three waves is given by as equation (2.1.3).

$$
\nabla^2 E(\omega_j) - \mu_0 \varepsilon(\omega_j)\frac{\partial^2 E(\omega_j)}{\partial t^2} = \mu_0 \frac{\partial^2 P_{NL}(\omega_j)}{\partial t^2} \qquad \textbf{(2.1.3)}
$$

Where index j can be replaced by p, s and i for deriving wave equation for pump, signal, and idler respectively. We can derive the wave equation for the pump, signal, and idler by replacing the P_{NL} and $E(\omega)$ with the corresponding expression given in equation (2.1.1) and (2.1.2). On replacing the corresponding term in equation (2.1.3), and working in slowly varying amplitude approximation (second-order variation in the field with propagation is neglected), we get the coupled-wave differential equations (2.1.4) for pump, signal, and idler. From equation (2.1.4), where, $\Delta k = k_p - k_s - k_i$, it is evident that the variation in pump amplitude depends upon the effective non-linear coefficient d and field amplitude of signal and idler. Similarly, field variation in signal and idler is dependent on the pump field and nonlinear coefficient. Under the condition of complete phase matching where $k_p = k_s + k_i$ which means pump photon momentum is the sum of signal and idler momentum, we get an efficient process of three-wave interaction.

$$\begin{aligned} \frac{dE_p}{dz} &= i\frac{\omega_p d}{cn_p} E_s E_i e^{-i\Delta kz} \\ \frac{dE_s}{dz} &= i\frac{\omega_s d}{cn_s} E_p E_i^* e^{i\Delta kz} \\ \frac{dE_i}{dz} &= i\frac{\omega_i d}{cn_i} E_p E_s^* e^{i\Delta kz} \end{aligned} \tag{2.1.4}$$

2.2 Optical parametric oscillators

From the discussion in the previous section, a strong pump in the second-order nonlinear medium can amplify the light and can generate signal and idler under complete phase-matching condition. In a single pass process, high intense pump amplifies the signal radiation, depending upon the gain of the nonlinear medium. By using the same principle as that of laser, this

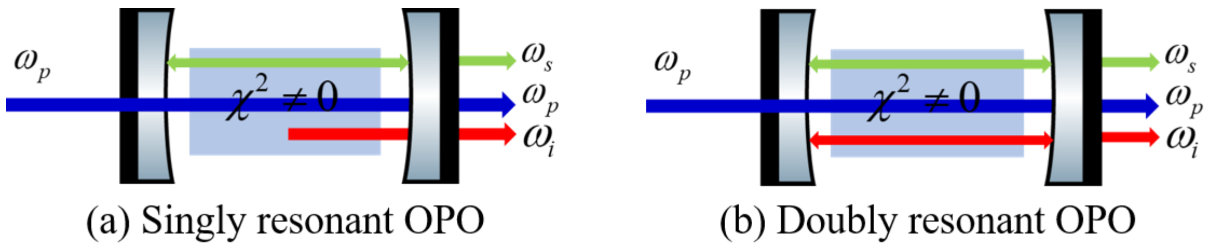

Figure 2.2. Schematic of optical parametric oscillator

parametric amplifier can be converted into an oscillator by putting the nonlinear gain medium inside a pair of mirrors. This pair of mirrors can be designed in such a way that they have minimum reflectivity for the pump wavelength and a very high reflection for either signal or idler wavelength or for both signal and idler. A schematic representation of doubly resonant and singly resonant OPO is shown in Figure 2.2. Here a pump photon enters into the cavity and generates signal, idler pair through parametric down-conversion. Cavity mirrors reflect signal/idler or both of them, after one round trip reflected beams propagate in the direction of the incoming pump beam. After one complete round trip, the signal/idler gets amplified in the presence of the input pump beam and after crossing the operational threshold, the cavity gives an output of coherent radiation. In the case of the singly resonant scheme, only one wavelength (either signal or idler) resonates inside the cavity, as shown in Figure 2.2(a). Whereas in the case of a doubly resonant scheme, both signal and idler resonate inside the cavity, as shown in Figure 2.2(b). There are other cavity configurations in which all the interacting waves resonate inside the cavity, known as triply resonant optical parametric oscillators. In this thesis, we have worked on the singly and doubly resonant OPO cavity configuration. In the upcoming section, we will discuss what are the various parameters involved in their designing mechanism.

2.2.1 Singly resonant OPO

To understand singly resonant OPO, we have considered a two-mirror cavity as shown in Figure 2.2 (a), such that the reflection coefficient of cavity mirrors for the pump and idler is $R_p=R_i=0$, while cavity mirrors reflect signal with reflection coefficient, $R_s=R_1$. Allowed signal resonating oscillation frequencies are dependent on the length of the resonator (L) and are given by $\omega_s = m\pi c / n_s L$ (n_s is the refractive index of the medium). This criteria further can be used to find the free spectral range of the OPO.

In this section, we have presented, the condition of threshold pump power required for the OPO to work. To find out the threshold power to run the OPO, we assume $E_s(0)$ as the signal amplitude at the input of crystal face and no idler field. After this, we have calculated the variation in the signal field along the crystal length. From equation (2.1.5) and assuming no phase mismatch in the system, we can simplify the variation of the signal, idler and pump amplitude variation along the propagation direction.

$$\frac{dE_p}{dz} = i\frac{\omega_p d}{cn_p} E_s E_i$$
$$\frac{dE_s}{dz} = i\frac{\omega_s d}{cn_s} E_p E_i^* \qquad \textbf{(2.1.5)}$$
$$\frac{dE_i}{dz} = i\frac{\omega_i d}{cn_i} E_p E_s^*$$

To find out the signal field along the crystal length, we looked at the second-order variation in the signal field with propagation distance z. We have assumed that we are working in no pump depletion region and ignored the pump variation with propagation, under this approximation second-order signal variation is presented by equation (2.1.6).

$$\frac{d^2E_s}{dz^2} = \frac{\omega_s \omega_i d^2}{c^2 n_s n_i} \left|E_p\right|^2 E_s \qquad \textbf{(2.1.6)}$$

For the singly resonant scheme, this wave equation results in the solution for the signal field along the propagation direction as shown in equation (2.1.7) .

$$E_s(z) = E_s(0)\cosh(gz) \qquad \textbf{(2.1.7)}$$

where gain coefficient, $g^2 = \frac{\omega_s \omega_i d^2}{c^2 n_s n_i} E_p^2$ defines the gain in the signal pass through a nonlinear medium. For OPO to work, after one complete round trip signal field should be equal to the input signal field. This condition is satisfied when the gain in the medium, equals losses inside the cavity. This condition gives rise to the threshold (g_{th}) condition and corresponding pump threshold intensity (I_{th}^p) as shown in equation (2.1.8). Also, it is evident that threshold intensity is inversely proportional to the effective nonlinear coefficient and length of the nonlinear medium, which directly determines the gain in a single pass process. Also, we have only considered losses due to the transmission in the mirror and neglected other losses such as scattering, absorption, and diffraction losses in the medium.

$$g_{th} = \frac{\sqrt{2}}{l}\left(\frac{1}{\sqrt{R_1R_2}} - 1\right)^{1/2}$$
$$I_{th}^{p} = \frac{cn_p n_s n_i}{\mu_0 \omega_s \omega_i d^2 l^2}\left(\frac{1}{R_1R_2} - 1\right) \qquad \textbf{(2.1.8)}$$

Equation (2.1.6) can also be used to determine the pump intensities output in the process. By using the same mechanism as that of the signal field, output pump intensities give a cosine dependence as shown in equation (2.1.9).

$$I_{out}^{p} = I_{in}^{p}\cos^2\left(\frac{I_{in}^{p} - I_{out}^{p}}{I_{th}^{p}}\right) \qquad \textbf{(2.1.9)}$$

Where I_{in}^{p}, I_{out}^{p} are pump input and output intensities at the crystal face. In the case of singly resonant OPO, one can achieve maximum output power in signal and idler at pump intensities of $2.47 I_{th}^{p}$.

2.2.2 Doubly resonant OPO

In doubly resonant OPO, as shown in Figure 2.2(b), we oscillate both signal and idler inside the cavity. In this case, we select cavity mirrors in such a way that they have a high transmission for the pump wavelength and high reflection for the signal (R_s) and idler (R_i) wavelength. In the case of a doubly resonant system, the cavity must satisfy the resonance condition for both signal and idler frequencies. Due to the oscillation of both signal and idler inside the cavity, now we cannot assume zero idler field at the crystal input face and we need to modify the signal and idler field equations. For the doubly resonating scheme, field equation for the signal and idler is give by the equation (2.1.10).

$$E_s(z) = E_s(0)\cosh(gz) + i\sqrt{\frac{\omega_s n_i}{\omega_i n_s}}E_i^*(0)\sinh(gz)$$
$$E_i^*(z) = E_i^*(0)\cosh(gz) - i\sqrt{\frac{\omega_i n_s}{\omega_s n_i}}E_s(0)\sinh(gz) \qquad \textbf{(2.1.10)}$$

For simplified understanding, we have assumed the reflection coefficient of the cavity mirrors for signal and idler are close to unity. After considering gain equals to the loss in the cavity after one complete roundtrip in this cavity configuration, we have a pump threshold intensity condition for the doubly resonating OPO, as shown in equation (2.1.11).

$$g_{th} = \frac{\sqrt{(1-R_s)(1-R_i)}}{l}$$
$$I_{th}^{p} = \frac{cn_p n_s n_i}{\mu_0 \omega_s \omega_i d^2 l^2}\left((1-R_s)(1-R_i)\right) \tag{2.1.11}$$

Now we have an understanding of the SRO and DRO operation. We have compared the threshold power requirements for the working of singly resonant OPO and doubly resonant OPO in equation (2.1.12).

$$\frac{\left(I_{th}^{p}\right)_{DRO}}{\left(I_{th}^{p}\right)_{SRO}} = \frac{(1-R_i)}{2} \tag{2.1.12}$$

In the case of doubly resonating of signal and idler, gain in the cavity is very high due to oscillation of both signal and idler, and results in a lower threshold as compared to the singly resonant OPO. As mentioned before DRO needs to satisfy the oscillation of signal and idler at the same time, which makes this system unstable as compared to the singly resonant OPO. This instability rises due to the refractive index dependence on wavelength, fluctuation in temperature or mechanical vibration results in the change in refractive index or cavity length respectively and leads to the cavity selection of new oscillating pair conditioned to the phase-matching. Since signal/idler wavelengths are dependent upon each other and free spectral range of the cavity will not allow all possible combinations to oscillate inside the cavity. This leads to frequency and phase instability inside the cavity and results in the jumping of signal and idler wavelength from one pair to another.

Tunability in this process is achieved through the different mechanisms depending upon what kind of phase matching technique we are using. Any parameter which changes the refractive index of the nonlinear medium is used as a tuning parameter. For OPO configuration with a nonlinear medium as BPM, angular orientation is used as a controlling parameter for the wavelength tuning. By changing the angle between the pump beam wave vector and the optic axis of the medium, the refractive index for the interacting waves will change. This change in the refractive index will correspond to a new phase-matching condition and changes the wavelength of the resonating beam inside the cavity. This method utilizes the angle on the nonlinear crystal and provides tunability to the coherent radiation. For OPO based on QPM crystals, temperature and grating period are used as a parameter for OPO tunability. By changing the temperature of the medium, refractive index changes, this affects the phase-matching condition and signal/idler will move to a new pair of wavelengths to cancel the resultant phase mismatch. Another parameter for wavelength tuning in QPM crystal is the grating period, which is dependent on phase mismatch in the three-wave interaction process. By changing the grating period, one can choose the new signal idler pair for a fixed pump, for efficient energy transfer. Another important parameter for wavelength tuning is pump tuning, in which by keeping all other parameters fixed one can tune the wavelength by tuning the pumping wavelength to the OPO.

2.3 Designing the OPO cavity

OPOs have proved their versatility as a tunable source of coherent radiation. To build an OPO, one needs to choose different parameters for getting the best performance out of the system. Out of various parameters, pump source, nonlinear gain medium, and cavity design are crucial for making an OPO.

2.3.1 Nonlinear gain medium

The nonlinear medium acts as a gain medium in the OPOs and requires selection for the best performance from the system. Not all the medium can be used as a gain medium to observe second-order processes, moreover $\chi^{(2)}$ medium is anisotropic in nature which limits the available options. For choosing a nonlinear crystal for OPO, one of the important parameters is the transparency range. Since we need a high intense pump field for achieving the threshold power for the OPO operation. If a crystal is not transparent for the interacting waves, absorption of the pump field leads to a serious problem of performance degradation. The second parameter is the damage threshold of the medium, OPOs are sources of high average power, which requires high pump power to pump the nonlinear medium, so damage threshold consideration is another crucial parameter for the medium selection. Thermal conductivity of the medium also plays a key role for material selection, due to the high pump power, of the order of MW/cm^2, it generates a lot of heat in the medium, which in turn needs proper heat sink mechanism to avoid any damage and performance issue in the system. Therefore, a medium with good thermal conductivity is preferable for OPO operation.

The figure of merit (FOM) is defined as $d_{eff} / \sqrt{n_p n_s n_i}$ is one of the most essential parameter for material selection for the parametric interaction. Nonlinear gain determines how much gain extraction is possible in the single-pass process and makes the material selection highly dependent upon d_{eff} value. In practice, the d tensor can be reduced to a matrix with 18 elements, with different values across the matrix. Depending upon the parametric interaction and phase matching condition, one can decide which element of this tensor we can utilize. This simplifies the d_{eff} consideration as a scaler with a certain value and defines the strength of the nonlinear process.

For the efficient generation of coherent radiation through OPO, it is important to know the phase-matching possibility in the desired wavelength, while keeping above mentioned parameter in mind. In the second-order nonlinear frequency conversion process, maximum gain is achievable under the perfect phase matching and theoretically, it is possible to convert whole pump power to the desired wavelengths. Conversion efficiency achieved in the nonlinear process follows $sinc^2$ function with maximum conversion at one frequency and then it falls rapidly. Since in practice, it's not possible to have a single frequency laser system, each laser system has a specific spectral width which varies from continuous-wave to ultrafast laser system. While designing the medium, It is essential to consider the spectral and temperature acceptance bandwidth of the medium.

2.3.2 Pump source

The laser pump source determines how much maximum gain we can extract from the nonlinear medium. The selection of pump source depends upon the output wavelength requirement from the OPO. To generate coherent radiation with narrow linewidth from an OPO, it requires a narrow band CW pump source. The threshold of the singly resonant OPOs in CW pumping scheme is very high and require a selection of pump source with high average power to extract the maximum gain from the medium. Power fluctuations in the pump source reflect in the OPO output powers, for the stability in output power, it is crucial to choose a stable laser source. To achieve nanosecond to femtosecond pulses from OPOs, it needs a pulsed pumping source such as nanosecond laser, picosecond laser, and femtosecond laser sources. Pumping with an ultrafast laser helps to achieve the threshold with lower average power as compared to the CW laser sources due to the availability of high peak power. Although the use of ultrafast laser increases the peak power, in contrast, it evokes group velocity mismatch between the interacting waves and limits the length of the nonlinear medium. With ultrafast laser sources, crucial parameters are pump spectral as well as temporal width for the desired output wavelength through OPO. For all pump sources, another requirement is the good beam quality of the pump laser, sources with M^2 value closer to Gaussian distribution and good pointing stability are useful for the gain extraction from the nonlinear medium.

2.3.3 Cavity design

For the generation of coherent radiation from parametric interaction, the gain of the medium should exceed the losses in the system. One method to increase the gain is by enclosing the nonlinear medium inside a pair of mirrors and form a cavity. For the operation of OPOs, one needs to take care of the stability of the cavity which enables the efficient generation of output radiation. Different cavity designs lead to the controlling of longitudinal (possible frequencies) as well as transverse modes (spatial pattern) inside the cavity. Longitudinal modes inside the cavity are calculated from the separation between two mirrors of the cavity. For the Fabry-Perot cavity (with two plane mirrors), these longitudinal modes are given by, $\upsilon = nc/2d$, where, d is the separation between two mirrors, n is the corresponding refractive index of medium and υ is the resonant frequency of the Fabry-Perot cavity. This method is utilised to determine the possible frequencies which can oscillate in any cavity configuration. For transverse spatial pattern output from a cavity, Fresnel-Kirchhoff integral method, along with symmetries of the cavity decides mode selection inside the cavity. In practice, rectangular symmetric cavities can produce all possible HG modes depending upon the laser gain and input pump power.

The stability of an OPO cavity is determined by using the ABCD matrix method. ABCD matrix method is used to describe the evolution of light rays in a medium from initial to the final point. When a ray is travelling from one point to another, it can pass through different optical elements such as translation in free space, reflection through mirrors, focusing via the lens and curved mirrors and translation from one medium to another. These optical elements are represented by a 2x2 matrix and if they are applied in an exact sequence from point A to B, they give exact spatial evolution of the beam from initial to the final point. The ABCD matrix for different optical elements is given below in equation 2.3.1.

$$M_{trans} = \begin{pmatrix} 1 & d \\ 0 & 1 \end{pmatrix}$$
$$M_{refr} = \begin{pmatrix} 1 & 0 \\ 0 & \frac{n_1}{n_2} \end{pmatrix} \qquad \textbf{(2.3.1)}$$
$$M_{lens} = \begin{pmatrix} 1 & 0 \\ \frac{-1}{f} & 1 \end{pmatrix}$$

Where M_{trans}, M_{refr}, and M_{lens} are ABCD matrix for translation, refraction from a medium with refractive index n_1 to n_2 and lens of focal length f respectively. For a stable cavity, the crucial criterion is that the beam should return to its original state after one complete roundtrip. During this round trip, the beam will undergo translation as well as pass-through various optical components. Beam evolution is calculated through ABCD matrix formulation for one complete roundtrip and final ABCD components of the matrix define the stability of the cavity with the condition given in equation (2.3.2).

$$0 \le \frac{A+D+2}{4} \le 1 \qquad \textbf{(2.3.2)}$$

For the OPO cavity after finding the stability of the cavity, another important parameter is the Gaussian beam waist evolution inside the cavity. Since the gain of the medium is dependent upon the pump beam intensity which further depends upon the beam waist of the pump, moreover maximum pump power transfers among the down-converted beams interacting beams when they all have equal confocal beam parameters [35]. This condition makes it crucial to calculate the evolution of the Gaussian beam waist of the resonating beam and matching it with the pump beam after one complete roundtrip.

The Gaussian beam is characterized by the beam waist and radius of curvature of the wavefront. Conventionally, q parameter is used to define the Gaussian beam characteristics which is dependent upon beam waist and radius of curvature of the wavefront, where the q parameter is defined as follows:

$$\frac{1}{q} = \frac{1}{R_j} - i\frac{\lambda}{n\pi w^2(z)} \tag{2.3.3}$$

where R_j is the radius of curvature of wavefront and $w^2(z)$ is the beam waist at point z for the beam with wavelength λ. This calculation of beam waist depends on which type of cavity we are using for the experiment. This q parameter used with ABCD matrix formalism to calculate the Gaussian beam properties from point A to B with the final q parameter is given by equation (2.3.4)

$$q_2 = \frac{Aq_1 + B}{Cq_1 + D} \tag{2.3.4}$$

The final beam waist and radius of curvature are calculated by equating the final q parameter with an initial q parameter and putting an appropriate value of the ABCD matrix in the above equation.

For OPO configuration, the more general type of cavities are linear cavity with two plane or curved mirrors, V cavity, ring cavity, and X-cavity configuration. In this thesis work, we have utilized the V-cavity, ring cavity and X-cavity for the different studies. The schematic of these different cavity configurations in the singly resonant scheme is shown in Figure 2.3.

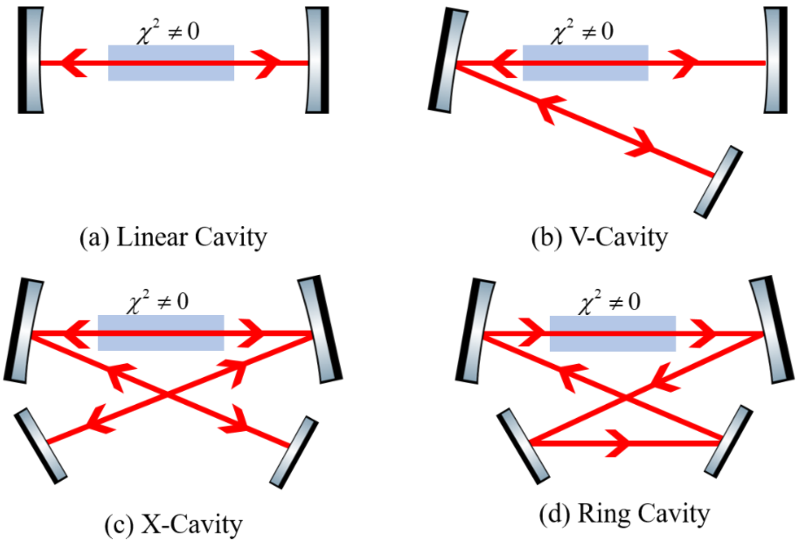

Figure 2.3. Schematic of different OPO cavity configuration

For simplified understanding, we can study the Gaussian beam evolution inside the ring cavity and we will find out how cavity design helps in achieving the maximum gain. Boyd and Kleinmann [35] suggested choosing the pump beam waist in such a way that l/b (l defines the length of the medium and b is the pump confocal beam parameter) should have a value of 2.84 for maximum gain extraction in single pass parametric process. For the Gaussian beam propagation, we take the center of the nonlinear crystal as the starting point with minimum beam waist $w(0)$. Gaussian beam with minimum beam waist starts to propagate along the length of the nonlinear crystal up to the face of the crystal. This process is characterized by the first translation matrix for the Gaussian beam waist calculation. At the exit point of the nonlinear crystal, there is a change in the refractive index, which corresponds to the refraction matrix. After this, the beam again propagates in free space from face of the crystal to the first curved mirror of radius of curvature, R, this implies translation matrix and then subsequent matrix for the curved mirror. After this beam propagates from the curved mirror to the plane mirror, which corresponds to the translation matrix and unit matrix for the plane mirror. Since the unit matrix represents the plane mirror, one can assume a continuous translation from the first curved mirror to the second curved mirror. After passing through the second curved mirror of the same radius of curvature beam translates to the input crystal face, this corresponds to the curved mirror matrix operation, translation matrix operation in the same order. After entering inside the nonlinear crystal, the beam sees a refractive index change, which corresponds to another refraction matrix and subsequent translation matrix until the starting midpoint in the nonlinear crystal, for the Gaussian beam. We expect the same Gaussian beam characteristics in the beam after one complete roundtrip for the stable cavity configuration. For achieving this goal, curved mirror separation plays a crucial role. We can calculate the Gaussian beam evolution for different cavity configurations in the same manner. For the understanding of beam waist

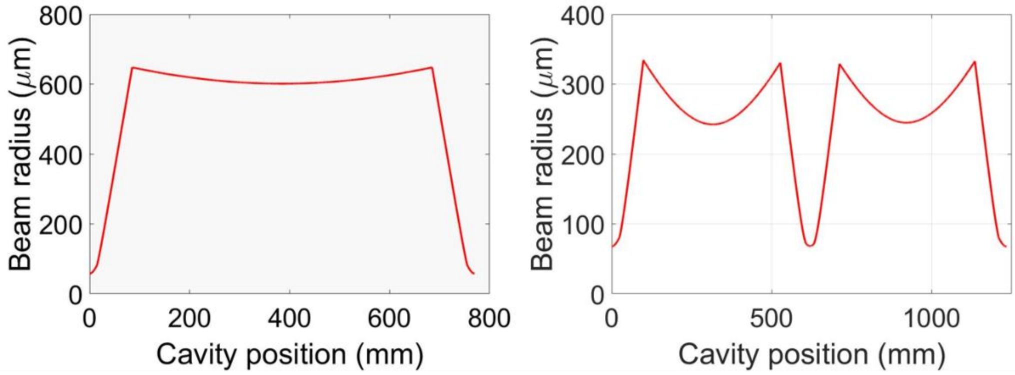

(a) Ring cavity (b) X-cavity

Figure 2.4. Beam waist evolution inside ring cavity and X-cavity

evolution, we have plotted the beam waist for the stable ring cavity and X-cavity configuration as shown in Figure 2.4.

2.4 Conclusion

In this introductory chapter, we discussed optical parametric oscillators, their threshold condition, and comparison between the singly resonant scheme and the doubly resonant scheme. We have also discussed what are key requirements for setting up an OPO in the lab, with focusing on the material selection, pump property, designing a stable cavity configuration.

Chapter 3 Direct generation of optical vortex and vortex dipole from OPOs

This chapter constitutes the following publications.

1) Varun Sharma, A. Aadhi, and G. K. Samanta, "Controlled generation of vortex and vortex dipole from a Gaussian pumped optical parametric oscillator," Opt. Express 27, 18123-18130 (2019).
2) Varun Sharma, S. C. Kumar, G. K. Samanta, and M. Ebrahim-Zadeh, "Optical vortex generation from an anti-resonant-ring picosecond optical parametric oscillator," in 2019 Conference on Lasers and Electro-Optics Europe and European Quantum Electronics Conference, OSA Technical Digest (Optical Society of America, 2019), paper cd_8_5 and manuscript under preparation for journal publication.

In this chapter, we have discussed the external mode convertor independent method of vortex beam generation directly from Gaussian pumped OPOs. These two works have enabled the direct vortex beam generation by either using the modes of the cavity or manipulating the cavity for higher-order mode generation.

3.1 Introduction

Optical vortices, the doughnut shaped beams carrying orbital angular momentum (OAM), have drawn a great deal of interest in recent times with new applications in various fields of science and technology including quantum information and quantum entanglement [9], lithography [36], high resolution microscopy [37] and micro-particle manipulation [38]. Typically, the optical vortices are generated through the mode conversion of the Gaussian laser beam using the conventional mode converters such as astigmatic mode converter based on cylindrical lenses to convert the HG modes into LG modes [12]. Other commercial techniques such as spiral phase plates (SPPs), with transverse thickness variation corresponding to the spiral phase pattern of the vortices [14], q-plates [39], liquid crystal-based spatial light modulators (SLMs) [40] and computer-generated holograms [13]. Among all mode converters, the SPPs, cylindrical mode converters and the etched-glass diffractive optical elements, are simple and stable devices to generate high power optical vortices required for various applications including nonlinear optics [41], gravitational wave detection [42] and micromachining [43]. On the other hand, with limited wavelength coverage, mode converters including q-plates and SLMs are conventionally used for applications requiring low output power vortex beams. However, the future advancement of optical communication with a demand of high-capacity and multi-channel operation requires high power laser source with wavelength and OAM-tunable vortex beam output over a wide spectral range. Efforts have been made in recent times to generate optical vortices from the lasers [44]. While the direct generation of high power optical vortices from lasers eliminates the need of phase elements for mode conversion, however, the limited wavelength tunability of the lasers is the major challenge towards the generation of vortex beams over a broad wide wavelength range.

On the other hand, optical parametric oscillators (OPO), based on nonlinear optical effects, have been established as the source of coherent radiation tunable across the electromagnetic spectrum in all time scales (continuous-wave (cw) to femtosecond) [45–47]. Therefore, the direct generation of optical vortex from the OPOs can be the most straightforward way of addressing the requirement of wavelength and OAM-tunable vortex beam directly from the source. Efforts have been made in recent times to generate optical vortex from the OPOs by transferring the OAM of the pump beam to one of the generated beams owing to the OAM conservation in nonlinear frequency conversion processes [48–50]. Similarly, the control of the cavity losses among the resonating beam has also enabled the selective transfer of the pump OAM modes to one of the OPO output beams [49]. However, due to the need of pump beam in vortex spatial profile, all the OPO based vortex sources [48–50] till date demand external mode converter for the pump wavelength. Additionally, the vortex pumped OPO has a higher operation threshold as compared to the Gaussian beam pumped OPO. Therefore, it is imperative to generate vortex beam directly from the Gaussian beam pumped OPOs.

3.2 Generation of vortex and vortex dipole from a Gaussian pumped optical parametric oscillator

Given the vortex beam generation through the superposition of orthogonal Hermite-Gaussian (HG) modes with suitable phase relation and the operation of OPOs in higher-order TEM modes [51], one can in principle generate vortex beam directly from a Gaussian beam pumped OPO. For the implementation of the direct generation of optical vortices from OPOs, requires higher-order mode oscillations inside the cavity. Here we demonstrated for the first time to the best of our knowledge, the direct generation of tunable optical vortex beam from a Gaussian beam pumped cw OPO. By controlling the overlap of the Gaussian pump beam and the fundamental OPO cavity modes through the external pump beam tilt, we have generated optical vortex of order, l=1, tunable across 970-1178 nm. The experimental results presented here are in close agreement with theoretical treatment used for vortex beam generation from the overlap of two Gaussian beams [52].

3.2.1 Experimental configuration

The realization of the generation of optical vortices through OPO is done in a green pumped doubly resonant OPO scheme. The configuration of the experimental setup is shown in Figure 3.1. A continuous-wave (cw), single-frequency, Yb-fibre laser, providing output power up to 50 W at 1064 nm in Gaussian intensity distribution is used as the fundamental laser. Using a lens, L1, of focal length, f = 150 mm, we have focused the laser beam at the centre of a 50 mm long, MgO-doped periodically poled congruent grown lithium tantalate (MgO: PPCLT) crystal (C1) having single grating of period, Λ_c= 7.65 µm to frequency-double into green at 532 nm with maximum output power generation of 4.5 W in a Gaussian intensity profile. The half-wave plate (λ/2) is used to adjust the polarization of the fundamental with respect to the poling period direction of the MgO:PPCLT crystal for optimum phase-matching. A lens, L2, of focal length, *f* = 150 mm is used to collimate the generated green and subsequently extracted from the undepleted pump using a wavelength separator, S1 (dichroic mirror with high transmission for 1064 nm and high reflection from 532 nm). The power attenuator comprised with a λ/2 centred at 532 nm and a polarizing beam splitter (PBS) cube is used to control the input green pump power to doubly-resonating OPO (DRO). With the help of subsequent λ/2 plate after power controlling unit, the polarization of the green pump beam is adjusted for the perfect phase matching and best performance for OPO operation. The DRO is configured in a standing wave V-shaped cavity configuration which comprised of two plano-concave mirrors, M1-M2, of radius of curvature, *r* = 100 mm, and a plane mirror, M3. All the cavity mirrors are high reflective (R>99.5%) across 850-1200 nm ensuring doubly resonant condition for signal and

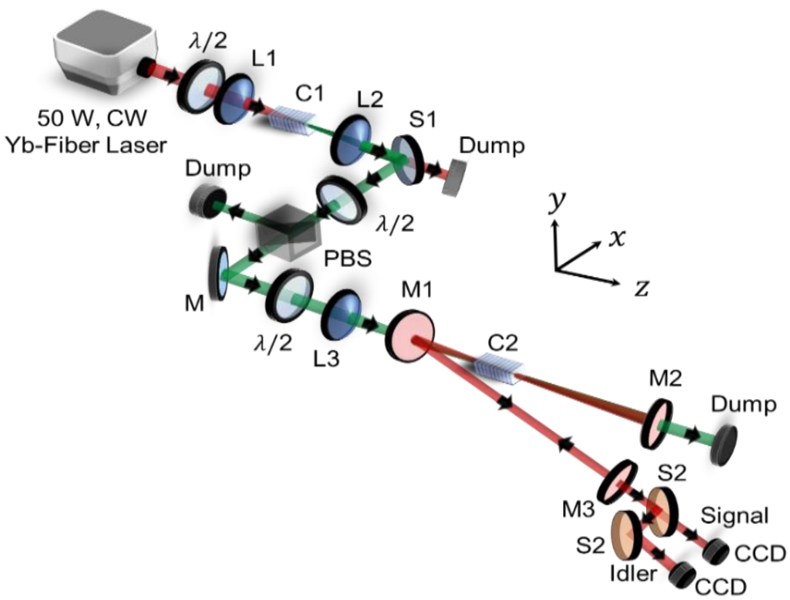

Figure 3.1. Schematic of the experimental setup. λ/2, half wave plate; L1-3, lenses; PBS, polarizing beam splitter cube; S1-2, wavelength separators; M, mirror; M1-3, DRO cavity mirrors; C1, PPCLT for SHG; C2, PPSLT for DRO.

idler beams and high transmission (T>95%) at pump wavelength, 532 nm. A 30 mm long and 2x1 mm^2 in aperture, MgO-doped periodically poled lithium tantalate (MgO:sPPLT) crystal

(C2) of single grating period of, Λ_c= 7.97 µm, is used as the nonlinear crystal for OPO operation. The crystal is housed in a temperature oven whose temperature can be varied up to 200°C with a stability of ±0.1°C. The out-coupled signal and idler radiation of mirror, M3, are wavelength separated using the separator, S2, for further studies. Since the mirror reflection changes vortex sign, we have used even number of reflections to both signal and idler beams before characterization. For maximum gain inside the OPO, the input Gaussian pump beam is focused at the centre of MgO:sPPLT crystal using a convex lens, L3, of focal length, f = 150 mm, to an estimated beam waist radius of w_p = 55 µm. The separation of the curved mirrors, M1 and M2, placed on the translation stages, was adjusted to match the confocal parameter of the resonating signal to that of the pump beam for optimum performance of the DRO [53]. The beam waist radius of the signal is estimated to be w_s = 78 µm with the optical length of the DRO cavity of, L = 315 mm.

3.2.2 Results and discussion

To verify the generation of vortex beam directly from a Gaussian beam pumped DRO, we adjusted the crystal temperature at 62°C producing signal and idler at 1002 nm and 1134 nm (recorded with ocean optics spectrometer) respectively, away from the degeneracy to study the beams individually. Pumping the DRO with the Gaussian beam, we have measured the spatial profile of the signal and idler for different cavity alignments with the result shown in Figure 3.2. As expected, for the exact alignment of the OPO cavity ensuring optimum overlap of the pump beam with the fundamental cavity mode, the Gaussian pump beam produces the signal and idler beams, as shown in Figures 3.2(a)-3.2(b), resembling Gaussian spatial profiles. For exact alignment, OPO started working at a pump power of 60 mW. To confirm the absence of any topological charge in the resonant beams, we have recorded the self-interference pattern of the signal and idler beams using a Mach-Zehnder interferometer (MZI). The straight line interference fringes, as shown in Figures 3.2(c)-3.2(d), confirm both signal and idler oscillating in fundamental cavity modes resulting in the Gaussian spatial intensity distribution.

Keeping the cavity parameters fixed, we have introduced a tilt between the Gaussian pump beam and the fundamental cavity mode by tilting the focusing lens, L3, in the transverse plane and recorded the intensity profile of the signal and idler beams with the result shown in Figures 3.2(e)-3.2(f), respectively. As evident from Figures 3.2(e)-3.2(f), both the signal and idler are

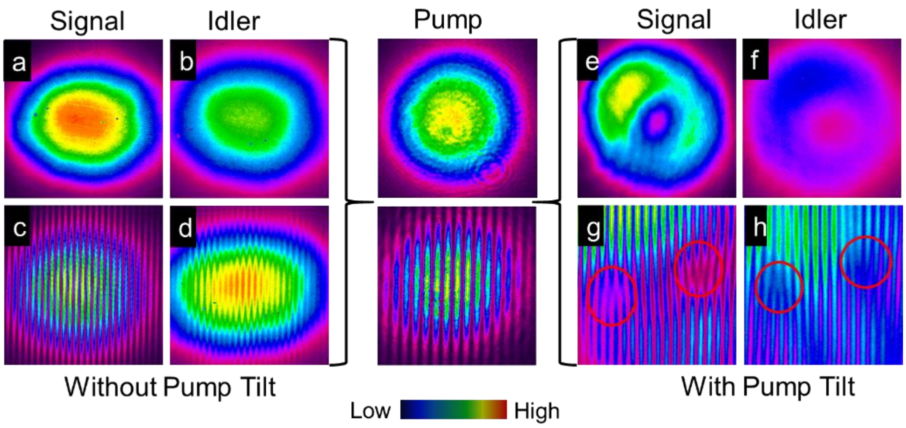

Figure 3.2. (a,b) Far-field intensity pattern and (c.d) self-interference of the signal and corresponding idler beams generated in absence of any tilt in the Gaussian pump beam. (e,f) Far-field intensity pattern and (g,h) self-interference of the signal and corresponding idler beams generated for the tilt in the Gaussian pump beam.

transformed into a beam with doughnut shape intensity distribution. To confirm the presence of topological charge, we have recorded the self-interference of the signal and idler beams using the MZI with the results shown in Figure 3.2(g)-3.2(h), respectively. The presence of characteristic fork in the interference pattern, as evident from Figure 3.2(g)-3.2(h), confirm both the signal and idler carrying optical vortices of the same order, $l_s = l_i = 1$ and same sign. Given the OAM conservation of nonlinear processes [48,49], one can expect the Gaussian pump beam, $l_p = 0$, to produce signal and idler vortices of the same order but opposite in sign satisfying, $l_p = l_s + l_i$. However, the generation of signal and idler beams with the same vortex order and sign from the Gaussian pump beam can be attributed to the generation of higher-order cavity mode due to the pump beam tilt and not due to the OAM conversation of the nonlinear process of the OPO.

To understand the vortex beam generation mechanism of the Gaussian pumped DRO, we have investigated the generation of vortex and dipole using superposition of two transversely scaled Gaussian beams [52].

$$E(x,y) = \sqrt{2}A\mathrm{Sinh}\left[-\frac{(x^2+y^2)}{2w_0^2}\left(\alpha^2-\frac{1}{\alpha^2}\right)+i\phi_{x,y}(x,y)\right]\exp\left[-\frac{(x^2+y^2)}{2w_0^2}\left(\alpha^2+\frac{1}{\alpha^2}\right)\right] \quad \textbf{(3.1.1)}$$

$$E_1(x,y) = A_1 \exp\left[-\frac{(x^2+y^2)}{w_1^2}\right]\exp\left[i\phi_1(x,y)\right] \quad \textbf{(3.1.2)}$$

$$E_2(x,y) = A_2 \exp\left[-\frac{(x^2+y^2)}{w_2^2}\right]\exp\left[i\phi_2(x,y)\right] \quad \textbf{(3.1.3)}$$

Above equations represent the electric field of signal/idler beams generated by pump beam and supported by the cavity mode, respectively with $A_1 = A_2 = A$, the complex amplitudes, and $w_o = w_1\alpha = w_2/\alpha$, $w_{1,2}$ are the beam waist radii. The parameter, α, describes the transverse scaling of the beams with linear phases, ϕ_1 and ϕ_2, whereas, $\phi_{x,y}$ is the phase difference between two beams in the transverse plane. The cavity is designed in such a way that the confocal parameter of the pump is equal to that of the signal beam [53]. Therefore, we can assume both the beams to have the same beam waist radius i.e., α = 1, and numerically simulated the intensity distribution of the superposed beam by varying the linear phase difference ϕ along the *x*-axis, *y*-axis with the results shown in Figure 3.3. As evident from Figures 3.3(a)-3.3(d), the superposed beam maintains a Gaussian intensity distribution for linear phase difference, $\phi_{x,y}$ = 0, and transform into HG_{10} mode, HG_{01} mode and HG_{01} mode along 45° due to the linear phase difference $\phi_{x,y}$ along *x*-axis, *y*-axis and 45° to the *x*-axis, respectively. The HG_{01} mode along 45° can be transformed into an optical vortex as shown by the inset of Fig. 3(d) using the astigmatic mode converter based on tilted curved mirrors of the OPO cavity [54].

To verify the theoretical proposal experimentally, we pumped the DRO at a constant power of 1 W producing signal (idler) at 1002 nm (1134 nm). Controlling the spatial overlap of the pump beam and the cavity mode by tilting the pump focusing lens, L3, to introduce linear phase along *x* and *y*-axis, we have recorded the spatial intensity profile of both signal and idler beams with the results shown in Figure 3.3(e)-3.3(h), and Figure 3.3(i)-3.3(l), respectively. As evident from Figure 3.3(e) and 3.3(i), both signal and idler beams have Gaussian spatial intensity profile in absence of any tilt in the lens, L3, similar to the theoretical result of Figure 3.1(a). The measured operation threshold as low as ~60 mW, confirms the DRO operation in fundamental cavity mode and the signal and idler carry Gaussian spatial mode. However, the introduction of linear phase difference between the pump beam with the cavity mode through the tilt of the lens, L3, by ~3' along *x*-axis and *y*-axis, transfer the pump energy to the resonating beams (signal and idler) in HG_{10} mode, and HG_{01}, as shown in Figure 3.3(f) and 3.3(j) and Figure 3.3(g) and 3.3(k), respectively. In addition, the presence of higher-order spatial mode for the signal and idler beams is also be confirmed from the increase of DRO threshold to ~280 mW in both cases. Since the HG_{01} mode along 45° can be represented as the superposition of HG_{10} and HG_{01} modes and can be transformed into an optical vortex, we have introduced a linear phase along 45° by tilting the lens along both *x*-axis and *y*-axis equally. As evident from Figure 3.3(h) and 3.3(l), both the signal and idler have doughnut shaped intensity distribution. While we expect the signal and idler beams to oscillate with HG_{01} mode along 45°, however, the tilted curved spherical mirrors of the DRO cavity act as an astigmatic mode converter [54] to transform the HG mode into an optical vortex. On the other hand, one can generate signal and idler beams in HG_{01} mode along 45° by reducing astigmatism through use of the low angle of incidence of the curve mirror and transform into vortex beams using external mode converter.

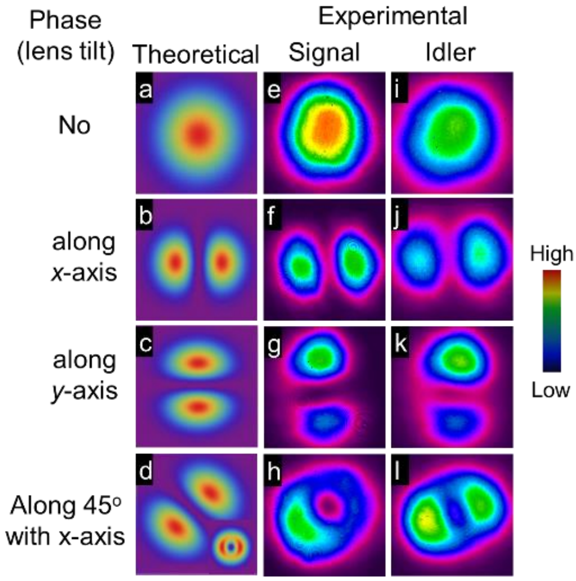

Figure 3.3. (a-d) Variation of theoretical intensity profile of the resultant beam due to the change in the relative transverse phase between two superposed Gaussian beams. Measured intensity distribution of (e-h) signal and corresponding (i-l) idler beams of the DRO with the pump beam title arising from the tilt of the focusing lens in transverse plane.

In such a case, we expect both the signal and idler beams to carry vortex spatial profile with the same order and sign similar to the current experimental results. From Figure 3.3, it is evident that experimental results are in close agreement with the theoretical prediction.

Although we have created a linear phase by tilting the lens, one can in principle observe the same effect by tilting the plane mirror, M3, and the curve mirrors, M1-2, of the DRO cavity. The tilt of the nonlinear crystal can modify the output modes of an OPO, however, it is not as sensitive as compared to the tilt of the lens and cavity mirrors.

On the other hand, the crystal tilt has more serious implications to the OPO performance in terms of wavelength change and crystal damage. We have measured the pump beam shift at the center of the nonlinear crystal due to the tilt of the focusing lens. Using a 4-*f* imaging system we have imaged the pump beam position at the center of the crystal in a CCD camera and measured the shift of the Gaussian beam by 12 μm along 45° to the *x*-axis for the lens tilt of 3' as used to generate vortex beam. It is to be noted that the beam waist size of the pump beam at the center of the nonlinear crystal is 55 μm. We have further recorded the spatial profile of the signal and idler beams across the tuning range of the DRO. The results are shown in Figure 3.4. Changing the crystal temperature from 60°C to 80°C, we have generated signal and corresponding idler tunable across 1005 - 970 nm and 1130 - 1178 nm, respectively, with total output power varying from 68 mW to 48 mW with a maximum of 84 mW at 995 nm for a fixed pump power of 4.3 W. As evident from the Figure 3.4(a)-3.4(f), the signal and corresponding idler beams carry doughnut shaped intensity profiles resembling optical vortex across the tuning range. To confirm the presence of phase singularity and determine the vortex order, we have recorded the self-interference of the beams using MZI. The presence of characteristic

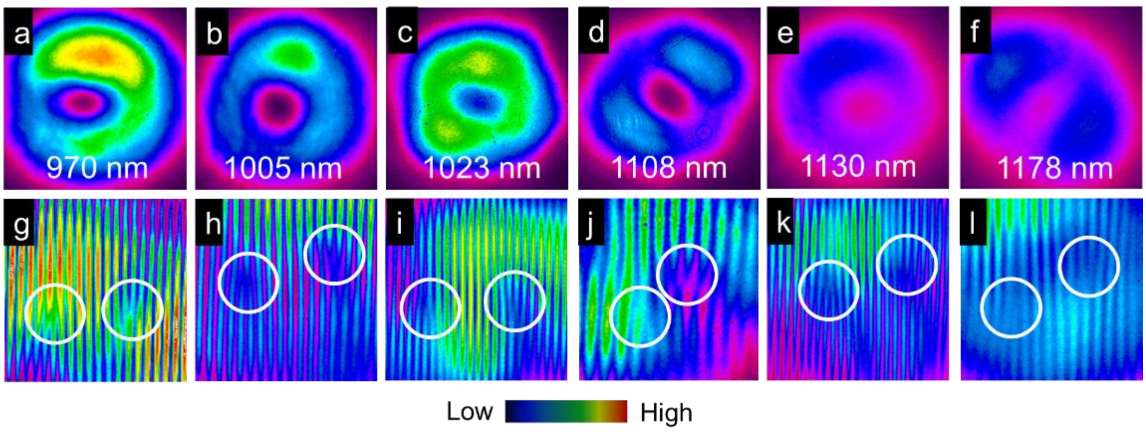

Figure 3.4. (a-f) Spatial intensity profile and corresponding (g-l) interference pattern of the output beam different wavelengths across the tuning range of the DRO.

fork, as shown in Figure 3.4(g)-3.4(l), confirms both the signal and idler beams to carry optical vortex of order, $l = 1$, and the same sign. The relatively poor image quality of the idler beams can be attributed to the inferior sensitivity of the CCD camera beyond 1100 nm. Due to the unavailability of suitable wavelength separator to extract the signal from the idler, we could not study the spatial form of the beams in the wavelength range of 1024-1107 nm. However, it is important to note that, we have recorded the spatial profile in doughnut shape in the wavelength range 1024-1107 nm but could not observe self-reference interference fringes due to the obvious reason.

As evident from [52], by controlling the beam overlap, one can generate vortex dipole. To verify the possibility of controlled generation of vortex and vortex dipole, we have designed the DRO in a standing wave X-cavity configuration (not shown here) comprised with two curved mirrors and two plane mirrors. Although the use of an additional plane mirror increases the OPO threshold to 112 mW due to the extra loss, however, we have observed the X-cavity configuration enabling easy control over the cavity modes and beam overlapping. Keeping the curved mirror separation of 127 mm corresponding to α=1 and optimizing the DRO to produce both signal and idler beams in Gaussian mode, further, we have tilted the plane mirrors and recorded the signal and idler beams with the results shown in Figure 3.5. As evident in Figure 3.5(a) and 3.5(b), the signal and idler beams have doughnut shaped intensity profile which further confirmed to carry vortex beams from the self-interference images recorded using MZI as shown in Figure 3.5(c) and 3.5(d). Due to the mechanical constraint of the X-cavity setup, the signal has faced one extra reflection as compared to the idler beam. As a result, the fork pattern of signal and idler are in opposite directions. However, counting the number of reflection in each beam path, we confirm that both signal and idler carry vortex beam of the same order, $l_s = l_i = 1$, and sign. Interestingly, the change in curved mirror separation from 127 mm to 118 mm changing the transverse scaling factor from α=1 to α=1.2, keeping rest of the cavity parameters unchanged, we still observe the signal and idler beams to have doughnut shaped profile as shown in Figure 3.5(e) and 3.5(f). However, the presence of oppositely oriented fork pattern in the self-interference images as recorded in Figure 3.5(g) and 3.5(h), confirm the generation of vortex dipole of unit charge in both signal and idler wavelengths. Such transformation of the vortex into vortex dipole can be attributed to the change in the transverse scaling factor, α, of the superposed beams and also to the increased beam astigmatism due to the presence of two curve mirrors of the DRO in X-cavity configuration. To measure the spatial stability of the resonating vortex beams, we have recorded 20 continuous frames in the CCD camera and estimated the shift in the dark core of the beam in

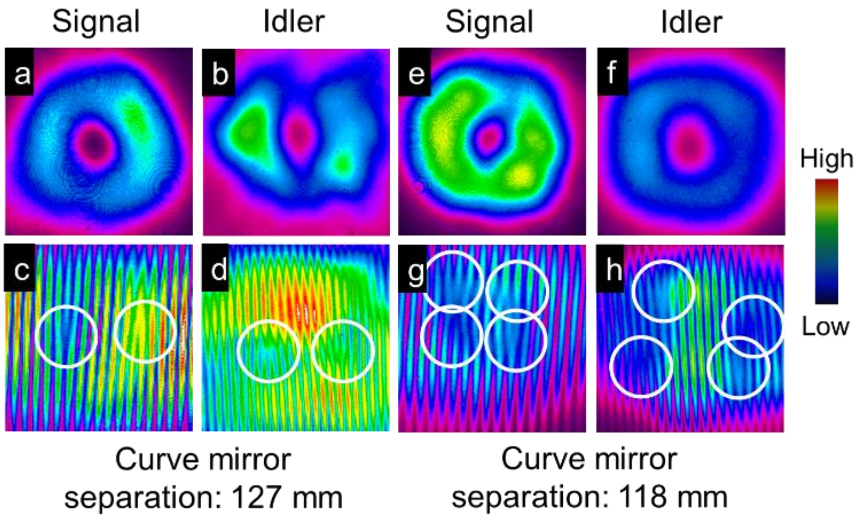

Figure 3.5. (a,b) Far-field intensity distribution, and (c,d) self-interference pattern of the signal and idler beams confirming the vortex beam generation for curved mirror separation of 127 mm. (e,f) Far-field intensity distribution, and (g,h) interference pattern of the signal and idler beam showing vortex dipole generation for the curve mirror separation of 118 mm.

each frame. We have observed a maximum variation of 60 μm and 62 μm along x and y directions respectively, from the mean position of vortex minima. Such small fluctuations of the beam position can be attributed to the instability of the DRO. Since the DROs have higher cavity instability as compared to singly-resonant OPOs configurations, using a suitable cavity locking scheme, one can improve the stability and mode quality of the output vortex beam. We have also studied the output power characteristics of the generated beam and recorded 86 mW of total output power at pump power of 4.3 W at a slope efficiency of 2.1%. While the increase of mirror transmission might produce higher output power, however, the increase of cavity loss can restrict the DRO operation in Gaussian mode.

In conclusion, we have demonstrated the direct generation of optical vortex and vortex dipole from a Gaussian beam pumped DRO by simply controlling the overlap of the pump beam with the cavity modes of the resonant beams. Pumping the DRO at green we have generated signal and idler beams in vortex spatial profile with the same order and sign tunable across 970-1170 nm with practical output power as high as 86 mW. Using the simple theoretical model explaining the vortex and vortex dipole generation from the superposition of two Gaussian beams, we have numerically simulated the beam overlap of the Gaussian pump beam with the cavity mode of the DRO in close agreement with the experimental results. The generic experimental scheme can be used to generate vortex and vortex dipole across the electromagnetic spectrum in all time scales (cw to ultrafast).

3.3 Optical vortex generation from ARR based singly resonant picosecond optical parametric oscillator

Discussion in this chapter highlighted the limitation of the commercially available method for the generation of optical vortices in terms of high power optical vortices over a broad range of wavelengths. All solutions either are dependent upon the mode conversion of Gaussian beams into optical vortices by SLM or phase plates and the method of direct generation of optical vortices from an OPO cavity itself can overcome the above limitations. The previous method depends upon the generation of HG_{01} mode inside the cavity and their mode conversion into optical vortices by the cavity-curved mirror. Similarly, an antiresonant ring (ARR) based

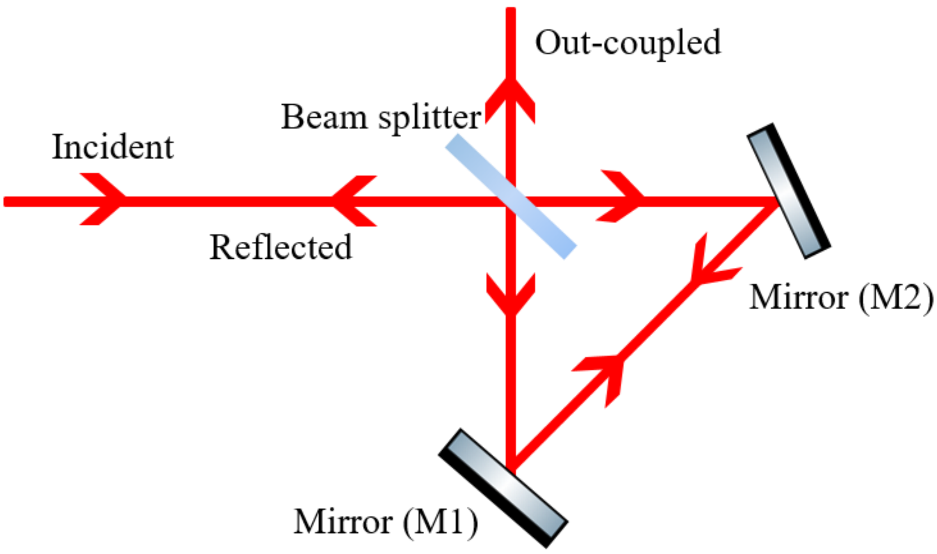

Figure 3.6. Schematic of anti-resonant ring scheme

optical parametric oscillator (OPO) [55] is also a potential method for the generation of optical vortices with high power over a broad range of wavelength. Siegman introduced the concept of ARR as a potential method to extract laser intracavity power [56]. This scheme utilises the reflection and transmission coefficient of the beam splitter to out couple the intracavity laser power [56] in Gaussian intensity distribution. As shown in Figure 3.6, beam splitter with reflection coefficient r and transmission coefficient t split the oscillating beam into two parts. After a complete trip inside this interferometer, they combine back on the beam splitter and (t^2-r^2) decide the outcoupled power from the cavity. Since commercial lasers operate in the Gaussian intensity distribution, the outcoupled beam can be characterized as the interference of two Gaussian beams. This concept of ARR based laser cavities is used for the generation of sub-nanosecond pulses from laser [57] and direct beam shaping in the laser cavities [58].

Method of ARR based cavities is utilised in OPOs to develop a system with high output power over broad wavelength [55] with tunable output coupling. This technique is further deployed for the generation of high repetition rate picosecond pulses [59] and continuous wave OPO operation [60]. In this work, we have utilised ARR based OPO and method of superposition of two Gaussian beams to generate first-order HG modes [61] and further converted to optical vortices by using a single cylindrical lens based mode conversion [12]. The advantage of the lower threshold for the Gaussian beam inside the OPO cavity and superposition of two Gaussian beams in the output port of the ARR, helped in the generation of optical vortices from 1457 nm to 1647 nm with output power as high as 848 mW across the tuning range.

3.3.1 Experimental Setup

For experimental realization, we have utilized a Yb fiber laser system cantered at 1064 nm with a maximum output power of 20 W, with a pulse width of 20 ps at 80 MHz repetition rate with a spectral width of ~2nm to pump the OPO. To avoid thermal issues with time in the system, we operated the laser with maximum output power and used a power controlling unit before the OPO. Input pump power to the OPO is controlled with a combination of a polarizing beam splitter and a half-wave plate (HWP) centered at the pump wavelength. To adjust input pump polarization according to the crystal optic axis for the maximum gain another HWP is employed as shown in Figure 3.7. To maximize the gain in the OPO, the pump beam is focused into the nonlinear crystal with a plano-convex lens of 200 mm focal length. We have calculated the beam waist to be around 60 µm at the focus on using a 200 mm focusing lens. For OPO action, we have used a multi-grating periodically polled lithium niobate (PPLN) crystal with an aperture size of 1 mm and length of 50 mm. The grating period varied from 28.3 to 31.8 µm with equal width of 0.5 mm across the width of the crystal. To minimize losses and to maximize the gain in the cavity, OPO designed in standing wave X-cavity configuration with a synchronous pumping scheme. OPO cavity constituted with two curved mirror M1 and M2 having a radius of curvature 150 mm, one arm of the X-cavity formed with plane mirror M3, and ARR is employed in other arm of the cavity. Mirrors M1-M3 had high reflection (>99.5%) for signal wavelength (1400-2100 nm) and high transmission (>95%) for pump (1064 nm) and idler (2100-4400 nm). For ARR configuration, we have used one pellicle beam splitter (BS) which have angle dependent reflection coefficient for signal wavelength from 1400-1600 nm and two plane mirror with high reflection for signal wavelength. To control the angle dependent reflection and transmission coefficient for the signal wavelength, pellicle beam splitter kept on

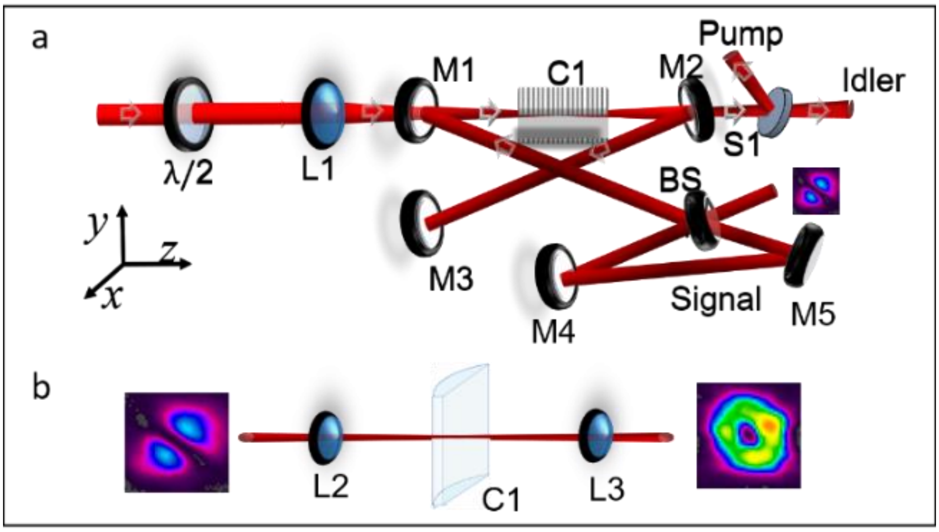

Figure 3.7 Experimental setup, λ/2: half wave plate, L1: lens, C1: PPLN crystal, M(1-2), M(4-5): Curved mirror (ROC: 150 mm), M3: plane mirror, BS: beam splitter, S1: pump idler separator; (b) HG to LG mode convertor, L(2-3): lens (f=150 mm), C1: cylindrical lens (f= 25mm).

the rotational mount. For adjusting total cavity length for synchronous pumping, mirror, M3 kept on a linear translation stage with total cavity length of 1.875 m. Mirror M1 and M2 are also kept on a micro translation stage for the coarse adjustment of the curved mirror separation to control the confocal beam parameter of the resonating signal for the best cavity performance [53]. Pellicle beam splitter kept at 26º with the normal incidence of the beam, to get 0.5, reflection and transmission coefficient for the resonating signal wavelength.

3.3.2 Results and discussion

For the initial working of the ARR based OPO, we used a 30.3 µm grating period of PPLN at a temperature of 150°C. We aligned the OPO cavity with minimum output coming out of the ARR, which corresponds to equal reflection and transmission coefficient. OPO operation started at a threshold of 2.9 W with an intracavity signal resonating in the Gaussian intensity profile. We measured the signal wavelength of 1570 nm at this temperature by using a spectrometer. This signal spectrum corresponded to an idler wavelength of 3301 nm. We have used intracavity aperture to remove higher-order modes in the resonating signal wavelength. To confirm the Gaussian mode operation in the signal, we imaged signal leakage coming out of the mirror M3 on pyrocam with pixel area of 85 X 85 µm. This confirmation made sure that the input beam to the ARR is in Gaussian intensity distribution. Since ARR is configured in common-path configuration, both reflected and transmitted beams faced equal amplitude and phase shift. We then measured the beam profile of non-resonating idler and ARR output for this cavity alignment. For the Gaussian pumped OPO, the output beam profile of signal and idler are in accordance with the expected beam pattern, as shown in Figure 3.8(a) and 3.8(b), respectively.

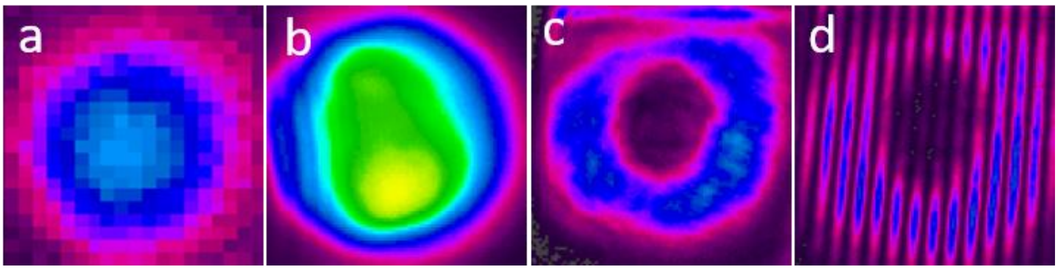

Figure 3.8. ARR based OPO; (a) intracavity signal profile, (b) non-resonating idler profile, (c) ARR output port beam profile, (d) ARR output self-interference pattern.

Interestingly, with minimum output power coming out of the ARR port, we observed a doughnut shape beam profile as shown in Figure 3.8(c). To find the presence of topological charge in the output beam, we used a Mach-Zehnder interferometer and did the self-interference of the beam. We observed linear interference fringes, which resemble with plane wave interference pattern. This interference pattern ruled out the presence of any topological charges in the output beam coming from the ARR output port. This beam profile resulted from the interference minima of the ARR interferometer and did not contain any phase singularities. To understand the output beam profile from the ARR, we utilized the method of Gaussian beam superposition as done previously in equation (3.3.1-3.3.3). At the output port of the beam splitter, we can consider both reflected and transmitted beams have equal phase and amplitude. This condition resulted in output in accordance with equation 3.3.1, with α=1 and ϕ_{xy}=0. Initially, with no linear phase difference between two beams, the resultant beam in the ARR output port have destructive interference and results in the generation of intensity minima beam profile, as shown in Figure 3.8(c). For the simulation purpose, we considered plane wave approximation, whereas in experiment input beams have phase variation in the beam. Since ARR is based on the two plane mirrors and one beams splitter, x and y-axis tilt in the beam can be used to give a linear phase for two Gaussian input beams. A tilt along the x-axis will result in the generation of HG_{01} mode and y-axis tilt will result in HG_{10} mode as shown in Figure 3.3(b) and 3.3(c). In our experiment, we gave simultaneous tilt to x and y-axis by using mirror M4 and M5, which resulted in the output beam in HG_{01} mode aligned 45° along the x-axis as predicted theoretically in Figure 3.3(d). As a result of simultaneous tilt in mirrors M4 and M5, there was more leakage of output power from the beam splitter which in turn resulted in the OPO threshold increase from 2.9 W to 4 W. To observe the output pattern from ARR output port, we have used pyrocam based Spiricon camera and recorded the resultant output beam profile. As shown in Figure 3.9(a), the signal output beam profile in HG_{01} mode matches the theoretical prediction. While aligning the ARR mirrors for the generation of HG modes, we observed idler in Gaussian intensity distribution as shown in Figure 3.9(b). For the conversion of HG_{01} into vortex, we have used a single cylindrical lens based astigmatic mode converter [62]. In this scheme, HG modes tilted, 45° with the x-axis, (linear combination of orthogonal HG modes of the same index) are focused with the help of a plano-convex lens, a cylindrical lens is introduced at the focus point within the rayleigh length. Since the input mode is aligned 45° with the axis of the cylindrical lens, astigmatism of the lens gives rise to a phase difference of $\pi/2$ between constituting orthogonal HG modes and results in the phase singularity in the beam. Collimation of the output beam with another plano-convex lens results in the doughnut shape intensity distribution. Experimental setup for the generation of optical vortex is shown in figure 3.7(b). We used a focusing lens of 150 mm to focus the HG_{01} mode, a cylindrical lens with a focal length of 30 mm to introduce astigmatism in the beam and another plano-convex lens of focal length 150 mm to collimate the focused beam. We have recorded the output beam profile of ARR on pyrocam

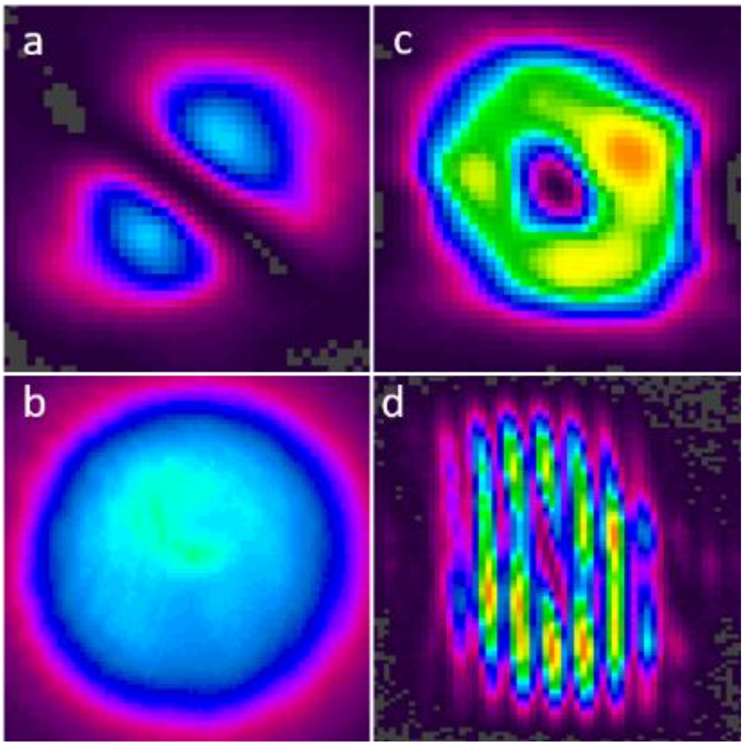

Figure 3.9. (a): ARR output signal in HG01 mode, (b): idler beam profile, (c): signal beam profile after the mode conversion, (d): interference fringes of signal after mode conversion.

and recorded doughnut shape intensity distribution as shown in Figure 3.9(c). For quantifying the topological charge and phase singularity in the beam, we have used a Mach-Zehnder based interferometer (MZI) and used the self-interference of the doughnut shape beam. We recorded the interference pattern of the MZI on pyrocam with two fork pattern in the opposite direction, as shown in Figure 3.9(d). This confirmed the topological charge of order 1 in the resultant doughnut shape beam. After the successful generation of optical vortices through the method of astigmatic mode conversion after the ARR output port in the OPO, we studied the tunability characteristics of the generated beams. For achieving the tunability in the OPO, we changed crystal temperature from 50-180°C. Further tuning is extended by changing the grating period of the PPLN from 29.3 µm to 30.8 µm. By temperature tuning for the different grating periods, we successfully tuned ARR based OPO from 1457 nm to 1647 nm. Across this tuning range, we recorded the output beam profile on pyrocam and further confirmed the topological charge of the beam from MZI based setup. It is evident from Figure 3.10, beam is having doughnut shape profile all across the tuning range with interference fringes of two opposite fork pattern which confirmed the topological charge of order 1 across the tuning range. Across the tuning range we studied, the power variation in signal and idler beam by keeping the input pump power fixed at 7 W as

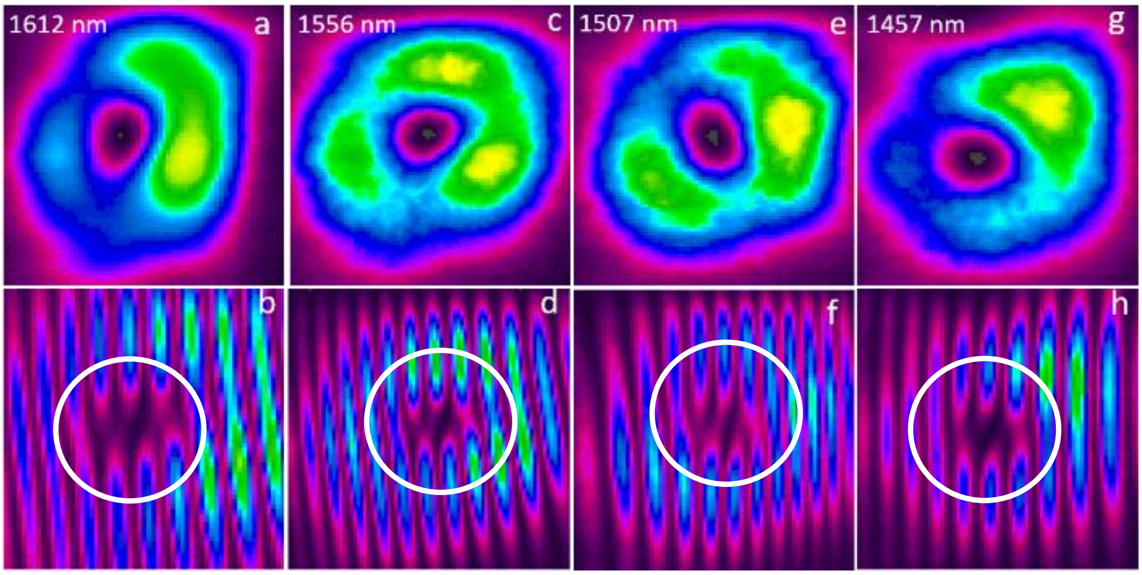

Figure 3.10. Signal profile across the tuning range, (e-h): corresponding signal interference pattern across the tuning range.

shown in figure 3.12(a). We observed power variation from 512 mW at 1457 nm to 417 mW at 1657 nm with a maximum power of 536 mW at 1489 nm as shown in Figure 3.11(a). While signal output tuned with wavelength tunability of 200 nm, we recorded idler in Gaussian beam intensity distribution from 3944 nm to 2973 nm. Across this tuning in idler wavelength, output power varied from 523 mW to 835 mW with a maximum output power of 580 mW at 3015 nm as shown in Figure 3.11(a).

After confirming the generation of optical vortices across the tuning range, we have done the power scaling at 1466 nm and 1591 nm. For output power characteristics, we pumped ARR based OPO with a maximum pump power of 11 W and initial pump power of 5 W. With maximum pump power of 11 W we observed signal power of 931 mW at 1466 nm with slope conversion efficiency of 10.9 % and 976 mW of idler power at 3880 nm with slope efficiency of 10.5 % as shown in Figure 3.11(b). By tuning the wavelength toward the degeneracy of the OPO, we recorded maximum output power of 1020 mW at 1591 nm with a slope conversion efficiency of 12 % while in idler we observed the maximum power of 1578 mW at 3212 nm with a slope efficiency of 19 % as shown in Figure 3.11(c). After the power scaling and tunability characteristics of the OPO, we studied the power stability of the vortex source at a signal wavelength of 1591 nm over a time of 60 minutes, as shown in Figure 3.12(d). For stability of this vortex source for a long time, we measured power stability by pumping the OPO with a constant pump power of 7 W. We measured the signal and idler output power over 60 minutes in Ophir power meter and recorded average output power of 491 mW and 735 mW respectively. We recorded a standard deviation of 16 mW in the signal vortex power and 4 mW in idler power in Gaussian intensity distribution.

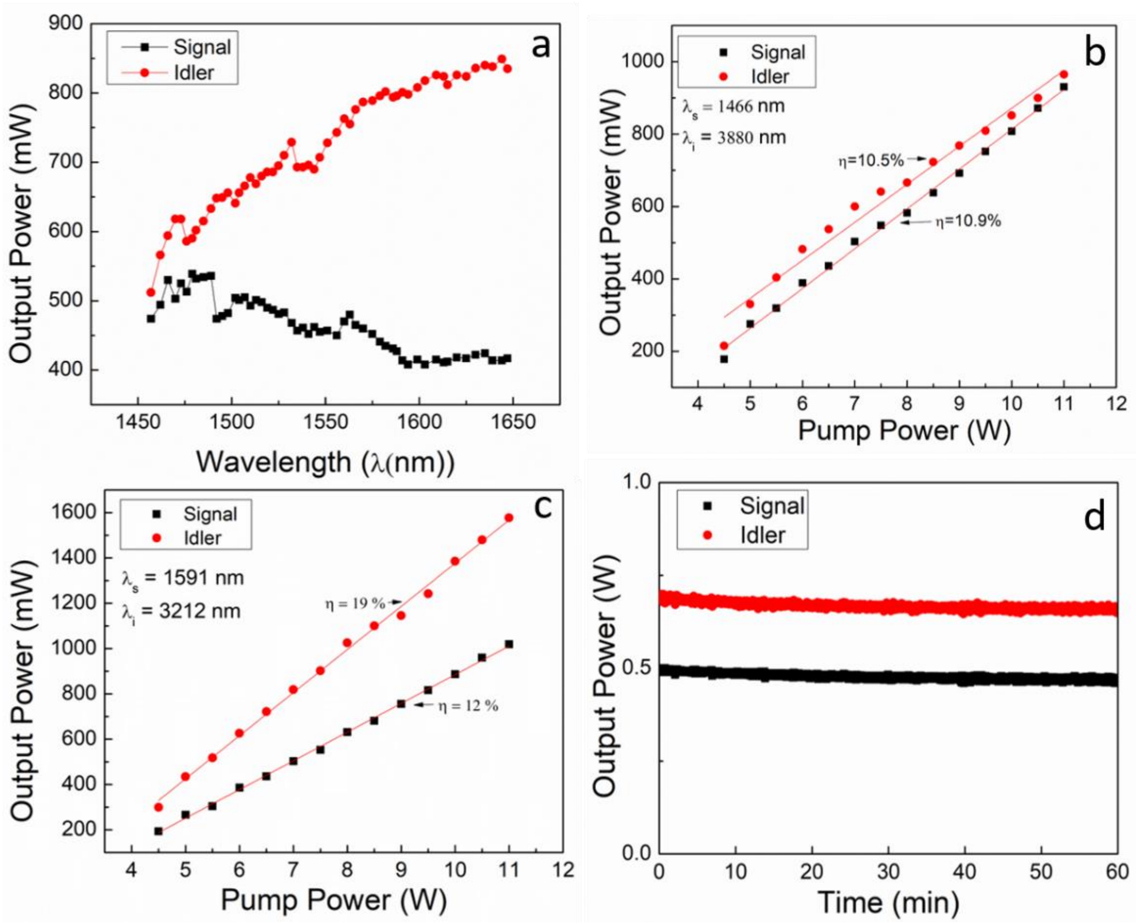

Figure 3.11. Power characteristics of OPO; (a) power variation across the tuning range, (b-c) power scaling, (d) power stability

After measuring the output power characteristics of the beams, we have studied the ultrafast nature of the generated optical vortices. We have done the spectrum and autocorrelation measurements to measure the spectral and pulse width across the tuning range. We observed the generated optical vortices with 16.5 ps pulse width and 1.4 nm of spectral width at 1453nm. Similarly, we measured the pulse width of 18 ps and a spectral width of 1 nm at 1550 nm. We repeated these same measurements over different spectral points across the tuning region and plotted time-bandwidth product across the tuning range as shown in Figure 3.13. We observed a time-bandwidth variation from 3.28 to 2.25 with a minimum bandwidth product of 1.84 at 1638 nm. These measurements confirms the ultrafast characteristics of the generated optical vortices through ARR based OPO.

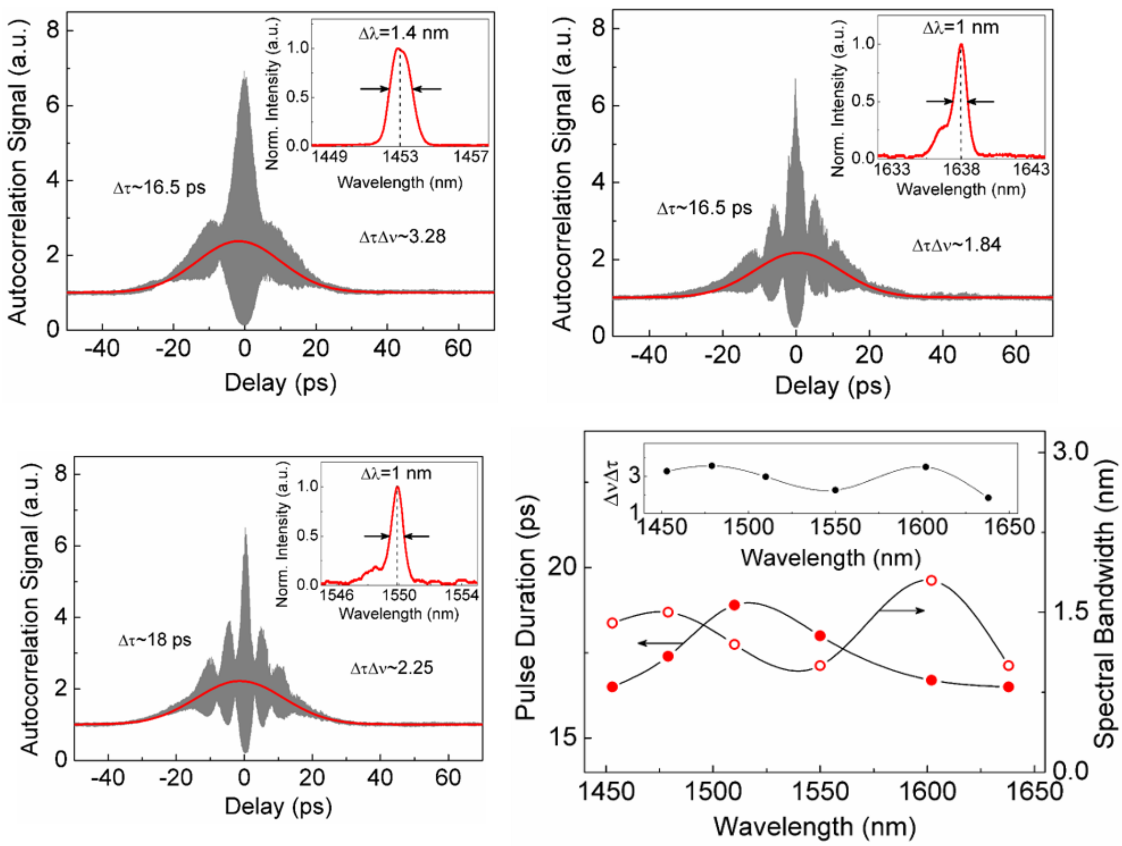

Figure 3.12. Spectral and temporal characteristics of the optical vortices across the tuning range.

In conclusion, in this work, we successfully demonstrated the direct generation of ultrafast optical vortices from a Gaussian pumped picosecond OPO. ARR based OPO, provided a stable mechanism for the generation of HG_{01} modes via superposition of two Gaussian beams coming through two input port of the interferometer. Generated optical vortices are continuously tunable over a spectral range of 200 nm from 1457 nm to 1657 nm, with maximum output power as high as 1 W. Stability and robustness of such system is observed with long-time power stability, beam evolution and presence of phase singularity in the beam across all wavelengths. This method is versatile and can be employed over all time scale.

3.4 Conclusion

In this chapter, we presented a method of direct vortex beam generation from Gaussian pumped OPOs. By using the technique of two Gaussian beam superposition inside the cavity, we demonstrated the direct vortex beam generation in DRO and HG modes from ARR based OPO which further converted into optical vortices. Both techniques are generic and can be used to generate optical vortices with broad wavelength tunability and high output power for various applications. Configurations demonstrated in this chapter, eliminated the dependence on phase elements and spatial light modulators for the generation of optical vortices. The scheme shown in section 3.1, can be utilized for the generation of higher-order optical vortices by generating higher-order mode oscillation inside DRO, but due to the DRO configuration, we are limited by the output powers. Whereas, the technique demonstrated in section 3.2 is limited for the generation of optical vortices up to order 1. In the next chapter, we discuss how we can overcome the limitations of the scheme presented in this chapter for the generation of higher-order vortices over a broad range of wavelengths.

Chapter 4 High power ultrafast optical vortex generation from near-IR to mid-IR

This chapter includes the following publications:

1) Varun Sharma, S. Chaitanya Kumar, G. K. Samanta, and M. Ebrahim-Zadeh, "Orbital angular momentum exchange in a picosecond optical parametric oscillator," Opt. Lett. **43**, 3606-3609 (2018).
2) Varun Sharma, S. Chaitanya Kumar, G. K. Samanta, and M. Ebrahim-Zadeh, "Ultrafast mid-IR vortex pumped picosecond optical parametric oscillator," submitted to Optics Express

In this chapter, we have studied the singly resonant OPO schemes under the vortex-pumping configuration. These studies focused on to study the OAM exchange between signal and idler in SRO configuration. We have also demonstrated the techniques for the generation of higher-order optical vortices with high average output powers from the near-IR to mid-IR regions through OPOs

Early experiment involving orbital angular momentum is second-order nonlinear optics showed OAM conservation in this process. The reports on using beam with OAM [32,63] in second harmonic generation (SHG) process have paved the way for the exploitation of nonlinear frequency conversion techniques as an alternative route to produce optical vortices with high power in new spectral regions. Consequently, the use of SHG and sum frequency generation (SFG) [64] has enabled production of higher-order vortices at shorter wavelengths [41]. On the other hand, frequency down-conversion techniques such as optical parametric generation (OPG) [65,66], optical parametric amplification (OPA) [67], and optical parametric oscillators (OPOs) [45] are routinely used to provide widely tunable source of radiation. Recently these processes have enabled the generation of optical vortices with higher order topological charge, for a fixed pump wavelength and OAM [68,69]. Similarly, such multimode OPOs have provided a stable source for the generation of hyper entangled states [70,71]. Method of intracavity OPA enabled the generation of high-power and higher-order OAM beams tunable across wide spectral regions in the continuous wave region [72]. While OPGs and OPAs are realized in relatively simple single-pass experimental schemes, the OAM of the pump beam cannot be selectively shared between signal and idler [68,72] due to the lack of suitable control parameters. Hence, the OAM of the generated beams is strictly governed by the angular momentum conservation rule and better overlap for different modes among the interacting beams. However, in an OPO, the spatial cavity modes, which play crucial role in the overall performance of the oscillator, can be used as a control parameter to transfer the pump OAM to the generated beams. In a doubly-resonant oscillator (DRO) scheme, successful demonstration of controlled transfer of the pump OAM to the signal and idler output beams in a continuous-wave (cw) OPO [49]. Given the intrinsic limitations of DROs with regard to wavelength tunability, phase instability and power fluctuations, it is important to develop alternative schemes to generate high-power and higher-order OAM beams using OPOs. In this context, singly-resonant oscillators (SROs) have tunabilty in the mid-IR wavelength region by direct transfer of the pump OAM mode with order up to, $l=2$, to the idler [69], indicating a non-zero spatial overlap integral [48,49], thereby satisfying the OAM conservation, despite the restrictions imposed by the cavity parity. However, due to the low parametric gain under cw pumping, the pump OAM mode in SRO was only transferred to the non-resonant idler [69], precluding the possibility to observe other combinations of output OAM modes. Selective transfer of orbital angular momentum among interacting beams in singly resonant scheme can open ways for the generation of high repetition rate higher order optical vortices and further can give access to blue region of the spectrum.

4.1 Orbital angular momentum exchange in a picosecond optical parametric oscillator

In this work, we demonstrated a simple mechanism to selectively choose the OAM mode combinations in the generated output beams from a synchronously vortex pumped ultrafast picosecond SRO, for the first time. The short pulse duration and high peak-intensity of input pump beam helped to extract high gain from a MgO:sPPLT crystal and used as the OPO gain medium to enable the generation of idler with OAM order as high as l=3. Generated idler beams are tunable across 1110-1209 nm for vortex order 1-3. Further, adjusting the separation between the focusing mirrors of the SRO cavity, we have observed additional output (signal, idler) OAM modes such as (0,3) and (1,2) for pump OAM mode, l=3, and (0,2) and (1,1) for pump OAM mode, l=2, which was not possible under cw pumping.

4.1.1 Experimental setup

The experimental configuration is shown in Figure 4.1. The primary laser source is a picosecond Yb-fiber laser providing up to 20 W of average power in 20 ps pulses at 78 MHz repetition rate, with a spectral bandwidth of 1.4 nm centered at 1064 nm. The laser beam is focused using a lens (L1) to a waist radius of wo~34 µm at the center of a 30-mm long LBO crystal (C1) for frequency doubling into green under noncritical phase matching (NCPM), providing up to 8 W of average power in ~16 ps pulses at 532 nm [73]. The generated green beam is collimated using a lens (L2) of focal length, f=100 mm, and extracted from the undepleted fundamental using a harmonic separator (S1). The NCPM scheme in LBO crystal ensures high green beam quality with TEM_{00} Gaussian spatial profile and M^2<1.04, as required for the generation of stable symmetric vortex beam through mode conversion techniques. The green pump power to the OPO is controlled using a combination of λ/2 plate and polarizing beam-splitter (PBS) cube. Using two spiral phase plates (SPPs), SPP1 and SPP2 centred at 532 nm, having phase winding corresponding to vortex orders 1 and 2, and their combination, we transform the Gaussian intensity profile of green pump beam into optical vortices of orders, l=1, 2, and 3, respectively. A second λ/2 plate is used to adjust the polarization of the green pump for perfect phase-matching in the nonlinear crystal. Using a lens, L3, of focal length, f=175 mm, we focused the pump beam at the center of the nonlinear crystal, C2, for the SRO operation. The crystal for OPO operation is a 20-mm-long MgO-doped stoichiometric periodically poled lithium tantalate (MgO:sPPLT), with a single grating period of μ=7.97 μm. To achieve tunability in the OPO, crystal is housed in an oven whose temperature can be varied up to 200 ºC with a stability of ±0.1°C. The SRO is configured in a four-mirror standing-wave cavity with two concave mirrors, M1 and M2, of radius of curvature (r=100 mm), and two plane mirrors, M3 and M4. All mirrors have high reflectivity (R>99.5%) for the signal (850-

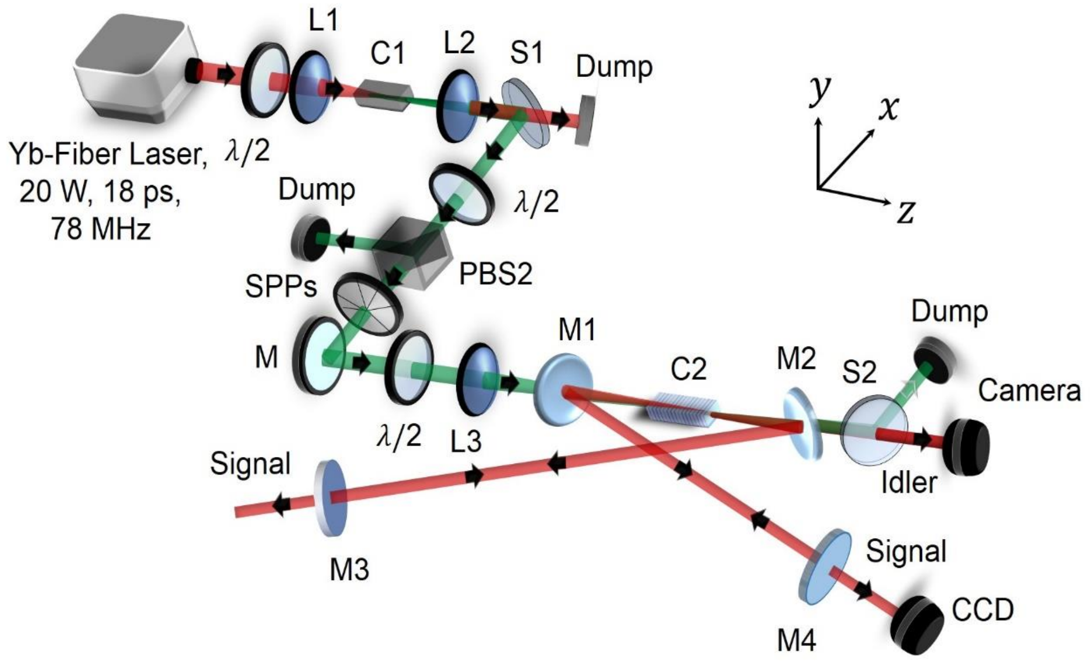

Figure 4.1. Experimental setup of the vortex pumped SRO. λ/2, half wave plate; PBS, polarizing beam splitter cube; SPP, spiral phase plate; L, lenses; S, wavelength separators; C, nonlinear crystals, M, mirrors.

1000 nm), and high transmission (T>95%) for the idler (1100-1450 nm) and pump (532 nm), ensuring singly resonant signal oscillation. The end faces of the crystal are antireflection-coated (R<0.5%) for the signal and pump, with varying reflectivity (R~1-15%) for the idler wavelengths. The total optical length of the cavity is maintained at 640 mm corresponding to the third harmonic of the pump repetition rate, resulting in a signal oscillations at a repetition rate of 234 MHz and idler generation at 78 MHz. However, while keeping the overall cavity length fixed for synchronization, we vary the separation between the focusing mirrors, M1 and M2, from 113 mm to 125 mm to alter the beam waist of the resonating signal to control the spatial overlap between the pump and resonating beams. The wavelength separator, S2 (high reflection for pump and high transmission for idler), is used to extract the idler output radiation from the undepleted pump beam for further studies. The spatial structure of the resonant signal beam is characterized using the leakage from the highly reflecting cavity mirror, M4. The intensity distribution of the signal and pump beams are recorded using a CCD camera of pixel size ~4.5×4.5 μm^2, while the idler beam is characterized using the pyroelectric array camera of pixel size ~85×85 μm^2.

4.1.2 Results and discussion

For initial operation and to study the vortex beam generation from the SRO, we fixed the crystal temperature at 92°C. Keeping a separation of 118 mm between the mirrors, M1 and M2, we pumped the SRO with vortex beams of orders, l_p=1, 2 and 3, at a constant power of 0.8 W. After successful operation of SRO, with the help of ocean optics spectrometer, we measured signal wavelength λ_s=962 nm with spectral width of 4 nm and corresponding idler wavelength λ_i =1190 nm. By keeping the pump power constant, we measured the intensity profile of the signal and idler beam, with the results shown in Figure 4.2. The first column, (a-c), of Figure 4.2, shows the intensity profile of the green pump beam generated by SPP1, SPP2, and their combination, respectively. As expected, the green beam after the SPPs in each case has a vortex (doughnut-shaped) intensity profile with increasing dark core size with the increase in the phase winding orders of the SPPs. To determine the order of the vortices, we used the tilted lens technique [74], where a vortex beam of order, l, while passing through a tilted lens, splits into l+1 lobes at the focal plane of the lens. The second column, (d-f), of Figure 4.2, shows the number of lobes, $n_p = l_p+1$ = 2, 3 and 4, aligned along 45° with respect to the tilt axis (vertical axis) of the lens, confirming the order of the pump vortices generated by the SPP1, SPP2 and the combination of SPP1 and SPP2 to be l_p = 1, 2 and 3, respectively. The third column, (g-i), of Figure 4.2, shows the doughnut-shaped intensity profile of the idler beam at 1190 nm with increasing dark core size with the pump vortices of orders, l_p = 1, 2 and 3. Again, to determine the order of the idler vortices, we passed the idler beam through a tilted lens and recorded the intensity profile at the focal plane of the lens, with the results shown in the fourth column, (j-l), of Figure 4.2. Counting the number of lobes of the images in the fourth column, (j-l), of Figure 4.2, we find the order of the idler vortices to be l_i = 1, 2, and 3, respectively, same as the order of the pump beam vortices, l_p = 1, 2, and 3. Similarly, we measured the intensity profile of the corresponding signal beam, as shown in the fifth column, (m-o), of Figure 4.2, in Gaussian spatial profile (l_s = 0) for all pump vortex orders. To confirm the absence of any phase singularity in the signal beam, we interfered the signal beam with itself using a Mach-Zehnder interferometer. The straight-line fringes, a characteristic pattern for the plane phase front, as shown in the sixth column, (p-r), of Figure 4.2, confirm the signal beams to carry vortex order,

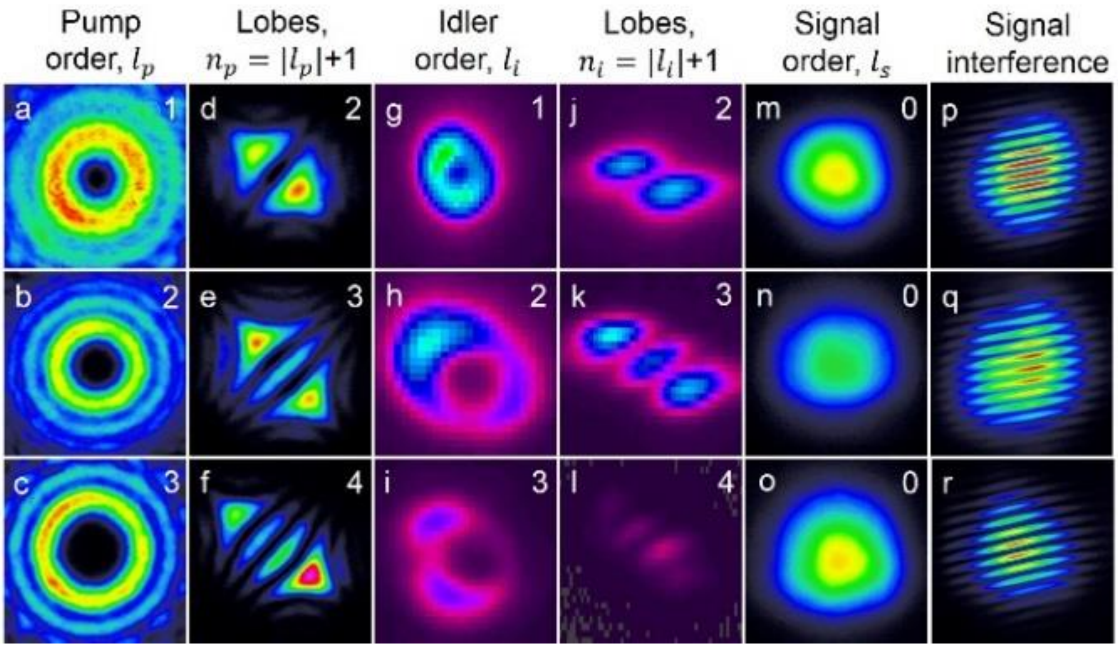

Figure 4.2. Far-field intensity distribution of the (a)-(c) pump OAM modes, lp=1, 2 and 3; (g)-(i) idler and (m)-(o) signal. Corresponding lobe structure of the (d)-(f) pump, (j)–(i) idler and interference pattern of the (p)–(r) signal OAM modes.

l_s = 0 (Gaussian), for all pump vortex orders. From the results of Figure 4.2, it is evident that the OAM of the pump beam of all orders, l_p = 1, 2 and 3, is directly transferred to the single-pass idler beam, resulting in vortex orders of l_i = 1, 2 and 3, respectively, whereas, the corresponding signal have vortex order, l_s = 0 (Gaussian beam), confirming OAM conservation in OPOs. It is to be noted that this is the first demonstration on the generation of tunable idler radiation of OAM order as high as $l_i = 3$. The pixelated images of the idler radiation, as compared to that of signal and pump radiation, is attributed to the larger pixel size and poor resolution of the pyroelectric camera than the CCD camera.

In the above experimental realization, pump OAM directly transferred to the idler beam while the signal is in the Gaussian intensity profile. Since for higher pump vortex order, there are finite probabilities of OAM division between signal and idler. To understand and control the OAM transfer mechanism in the SRO, we have calculated the normalized spatial overlap integral, $\Lambda_{p.s.i}$, of the interacting pump, signal and idler beams. As reported previously [48,49], the overlapping integral of the interacting beams, and hence the nonlinear parametric gain of an OPO, has a non-zero value for $l_p = l_s + l_i$. While l_s and l_i can have different integer values for a fixed value of l_p, satisfying OAM conservation, nevertheless, the cavity parity restricts the resonant modes in the OPO. Owing to the OAM conservation, one can expect the probable OAM mode combinations for signal and idler beams, (l_s, l_i), providing non-zero value of spatial overlap integral, to be (0,1) and (1, 0) for $l_p = 1$, (1,1), (0,2) and (2,0) for $l_p = 2$, and (1,2), (2,1), (0,3) and (3,0) for $l_p = 3$. Using the mathematical formalism of overlap integral for different interacting modes [48,49], we calculated, $\Lambda_{l_p l_s l_i}$, for different combinations of signal and idler OAM modes to be $\Lambda_{101} = \Lambda_{110}$ ~0.7 for $l_p = 1$, Λ_{211} ~0.7, $\Lambda_{220} = \Lambda_{202}$ ~0.5 for $l_p = 2$, and $\Lambda_{312} = \Lambda_{321}$~0.7, $\Lambda_{303} = \Lambda_{330}$ ~0.35 for $l_p = 3$. Since the Gaussian resonant beam (lowest-order mode) has the lowest cavity loss and maximum gain, the signal maintains the Gaussian profile (l_s=0) and the idler carries the OAM of the pump beam, $l_i = l_p$. However, from the calculated normalized overlapping integral, it is evident that the SRO can produce higher-order modes for the signal beam in the high-gain regime. However, for a given pump power and crystal parameters, the parametric gain in the SRO can be controlled by adjusting the confocal beam parameter of the resonant beam mode and its overlap with the pump beam, by varying the separation of the focusing mirrors. For a fixed pump power of 1 W at the input to the SRO, we thus systematically modified the separation between M1 and M2 in Figure 4.1, from 113 mm to 124 mm, while maintaining the overall cavity length at the third harmonic of the pump laser repetition rate, and recorded the spatial profile of the signal and idler beams for pump OAM order, $l_p = 2$ and 3. The results are shown in Figure 4.3. It is evident from Figure 4.3 that for both pump OAM modes, $l_p = 2$, and 3, the SRO have two distinct output OAM mode combination for the signal and idler beams for the two range of mirror separation of 113-118 mm and 119-124 mm. The pump beam of OAM mode, $l_p = 2$ (see Fig. 3(a)), produces signal and idler OAM mode combination, (l_s, l_i), of (1,1), as shown in Figure 4.3(b), and (0,2), as shown in Figure 4.3(c), with the cavity mirror separation in the range of ~119-124 mm and ~113-118 mm, respectively. Similarly, for the pump OAM mode, $l_p = 3$ (see Figure 4.3(d)), the variation in the cavity mirror separation in the range of 119-124 mm and 113-118 mm, results in OAM mode combination, (l_s, l_i), of (1,2), as shown in Figure 4.3(e), and (0,3), as shown in Figure 4.3(f), respectively, together with the verification of the vortex order using self-interference and tilted lens techniques. Such effect can be understood as follows. In the SRO cavity, the variation of focusing mirror separation modifies the confocal parameter of the resonant beam, hence its overlap with the pump beam in the crystal length, and thus alters the parametric gain. On the other hand, the calculated value of normalized overlap integral of the signal and idler OAM mode combination (1,1) of $l_p = 2$ and (1,2) for $l_p = 3$ are higher than that for other OAM mode combinations. Therefore, with the variation of the focusing mirror separation in the presence of high peak power of the pump pulses, the higher order modes in the SRO begin to oscillate, resulting in the resonant signal beam to carry OAM mode, $l_s = 1$, for pump OAM mode, $l_p = 2$ and 3. Given the increase of the SRO threshold for the higher-order resonant modes, the current source supports resonant beam of OAM mode, $l_s = 1$. Although the higher order OAM modes for the signal can, in principle, be achieved by increasing the pump power, however, we observed bulk damage in our MgO:sPPLT crystal at a green average power of ~4 GW/cm^2. Hence, we limited the pump power at the input to the SRO to < 2 W in these experiments. It is also important to note that, for pump vortex of order, l, the signal and idler OAM combinations, (l_s, l_i), of (l, 0) and (0, l) have same overlap integral and nonlinear parametric gain. However, the lowest loss of SRO for the resonant beam in the fundamental mode puts the selection rule to the OAM mode combination of (0, l) over (l, 0). We have also studied the wavelength tunability of our picosecond vortex beam source. Adjusting the focusing mirror separation of the SRO cavity for direct transfer the pump vortices to the idler beam, we pumped the crystal with vortex orders, l_p=1, 2, and 3, at 0.8 W of average power, and measured the single-pass idler power, with the results shown in Figure 4.4 As evident from Figure 4.4 (a), by changing the crystal temperature across 56-114°C, the idler vortex of order, li=1, can be tuned over 125 nm across 1102-1227 nm, with the output power varying from 116 mW at 1102 nm to 127 mW at 1227 nm, and a maximum idler vortex power of 147 mW at 1127 nm. Similarly, the idler vortex of orders, l_i =2 and 3, can be tuned across 1110-1209 nm with a maximum output power of 86 mW and 29 mW, respectively. The reduction in the output power of the idler vortices with order, across the tuning range, is

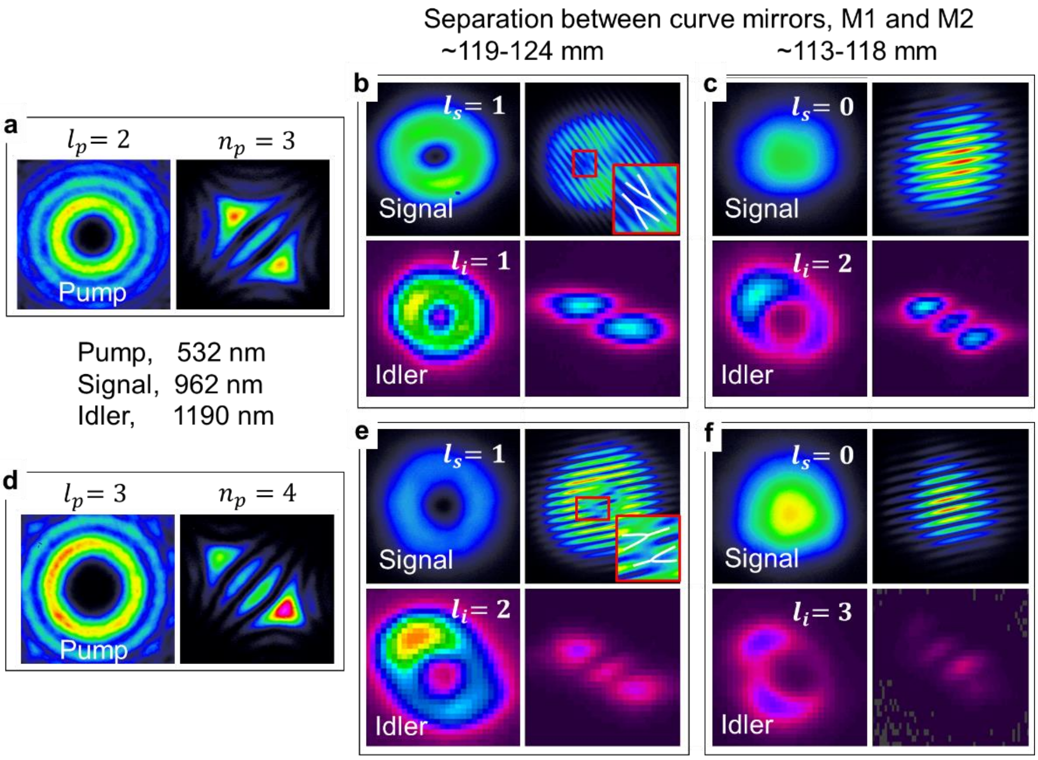

Figure 4.3. (a) Pump OAM mode, lp=2, and corresponding signal and idler OAM mode combinations for curve mirror separation (b) 119-124 mm and (c) 113-118 mm. (d) Pump OAM mode, lp=3, and corresponding signal and idler OAM mode combinations generated for curve mirror separation (e) 119-124 mm and (f) 113-118 mm. Insets are the zoomed image of the fork pattern of vortices marked with white lines.

attributed to the reduction in parametric gain with increasing order of the pump vortices [75]. To verify the idler beam in vortex spatial profile across the tuning range, we recorded the intensity profile of the generated idler beam for the pump vortex of order, l_p = 1, at three different crystal temperatures, 60ºC, 76°C and 92°C, corresponding to idler wavelengths of 1110 nm, 1154 nm and 1190 nm, respectively. As evident from the first column of Figure

4.4(b), in each case the idler beam has doughnut-shaped intensity profile resembling an optical vortex. Counting the number of lobes ($n_i = |l_i|+1 = 2$) in the intensity pattern recorded at the focal plane of the tilted lens, as shown in second column of Figure 4.4(b), we confirm the idler vortex order to be, $l_i = 1$, the same as the pump vortex order, across the SRO tuning range. We observed idler vortex of all orders maintaining stable intensity profile across the tuning range.

Further, we studied the power scaling characteristics of the source. For a fixed crystal temperature of 66°C, corresponding to the idler (signal) radiation at 1127 nm (1007 nm), we pumped the SRO with vortex orders, $l_p = 1$, 2, and 3, and recorded the idler power as a function of vortex pump power. As evident from Figure 4.4(c), the output power in the idler vortex of orders, $l_i = 1$, 2, and 3, increases linearly with the pump vortex power at slope efficiencies of η =29%, 19% and 17%, respectively, without any sign of saturation. The maximum average output power in idler vortex of orders, $l_i = 1$, 2, and 3, is 202, 113, and 57 mW, respectively, for pump power of 1 W. Although one can expect higher idler power with the increase in pump power for all vortex orders, we restricted our study to pump power of ~1 W, limited by the MgO:sPPLT crystal damage. Using the linear fit (black line) to the experimental data, we can

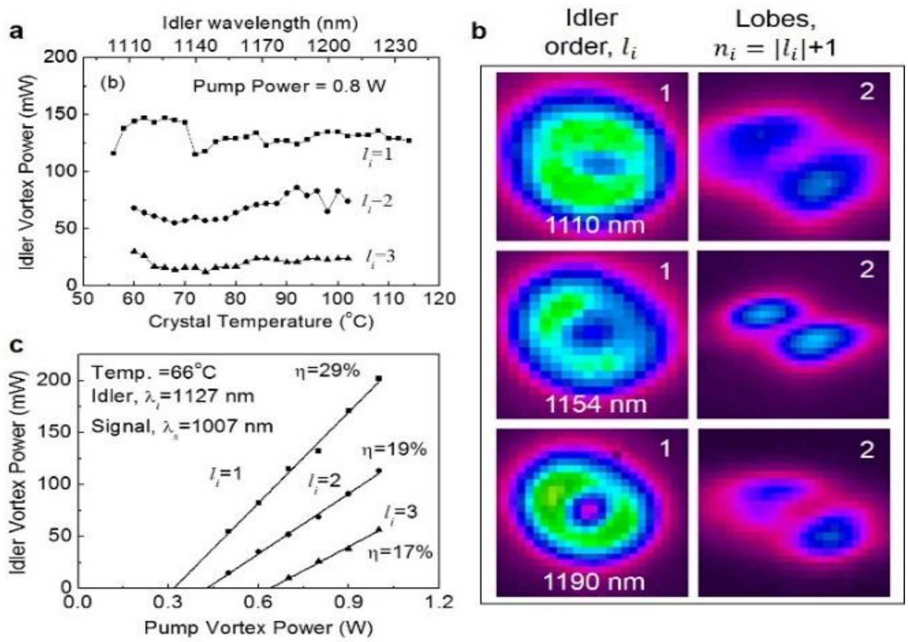

Figure 4.4. (a) Variation of output power of the idler OAM mode li=1, 2 and 3 across the tuning range. (b) Intensity distribution and characteristic lobe of the idler OAM mode at different wavelengths across the tuning range. (c) Power scaling of the SRO for idler OAM mode li=1, 2 and 3

estimate the operation threshold of the SRO for the pump vortex orders, l_p = 1, 2, and 3, to be ~320, 430, and 660 mW, respectively. The increase in the SRO operation threshold with the order of the pump vortex can be attributed to the reduction in parametric gain due to the increase in the dark core size of the pump vortex with order [75]. Using a CCD camera, we measured the dark core size for pump vortex orders, l_p = 1, 2, and 3, under our experimental conditions, to be ~38, 66 and 90 μm, respectively. It is to be noted that the intra-cavity signal beam measured using the leakage from the mirror, M3, shows a Gaussian spatial profile for all pump vortex orders and powers.

In conclusion, we have generated ultrafast optical radiation at a repetition rate of 78 MHz in vortex spatial profile tunable across the near-IR wavelength range. Pumped in the green the source produces idler beam with OAM modes of 1, 2 and 3 tunable across 1110-1209 nm with a maximum power of 201 mW. We have demonstrated the controlled transfer of OAM modes using an ultrafast SRO for the first time. Further, scaling of the vortex order as well as the power across the tuning range is possible by increasing the pump power, but limited by crystal damage.

4.2 High power, high order mid-IR ultrafast tunable optical vortices

Mid-infrared (mid-IR) coherent sources have drawn a great deal of interest for various scientific and technological applications in last few decades due to the presence of rich spectroscopic signatures or the strong absorption fingerprint of numerous molecules [76], harmful gases [77], and biological tissues [78]. As majority of the applications of the mid-IR sources, till date, are based on the use of the spectral, temporal and output characteristics of the such sources in Gaussian spatial profile, efforts have been made over time to improve such characteristics of the mid-IR sources with the help of recent technological advancement in the field of laser technology and material science. While vortex beams find numerous applications with time, efforts are being made to generate optical vortices across the electromagnetic spectrum from UV [41], to, THz [72,79] to facilitate new applications. Given the potential applications of the mid-IR wavelength range, the generation of higher-order mid-IR vortex beams can open potentially new avenue towards, for example, non-destructive super-resolution spectroscopy of molecules, free space optical networking with OAM multiplexing, and controlled fabrication of chiral organic materials. Therefore, it is imperative to device alternative techniques and methodologies to produce higher-order optical vortices in the mid-IR wavelength range. In the continuous wave domain, shorter cavity length enables the generation of optical vortices in the mid-IR spectral region [72]. But, the generation of vortex ultrafast pulses with high output power and shorter pulses have not been explored. Whereas OPOs have proved their versatility as a coherent source of radiation over a wide range of spectral region in all time scales. Particularly, the mid-IR molecular figure-print region in combination with the ultrafast optical vortices could lead to the study and advancement of high-resolution molecular spectroscopy, light-induced chiral structure [80] formation in organic molecules and bio-imaging. For the generation of optical vortices in the mid-IR region, periodically poled lithium niobate (PPLN) based OPOs are a potential solution. PPLN based 1.064 μm pump OPO [81] in mid-IR region enables the use of long interaction lengths resulting in high gain generating mid-IR radiation up to 4 μm. This configuration can be used to pump OPOs with higher order optical vortices directly which was not possible in continuous wave domain. (This is enabled by the availability of high average power 1 um picosecond lasers providing high peak-power). In this work, we have demonstrated the direct generation of optical vortices in mid-IR region of the spectrum with maximum vortex order 5. By using PPLN based ultrafast OPO, we have generated optical vortices up to 4035 nm with tunability up to 1600 nm with maximum output power up to 2.2 W.

4.2.1 Experimental setup

The experimental setup to generate optical vortices in mid-IR is shown in Figure 4.5. We used a picosecond Yb-fiber laser centered at 1064 nm with a spectral bandwidth of 1.4 nm, pulses of width ~20 ps at a maximum average output power of 20 W in Gaussian intensity profile mode as the pump laser. The laser power in the experiment controlled using a combination of the half-wave plate (λ/2) and a polarizing plate beam splitter cube (PBS). The same PBS in combination with a quarter-wave plate (λ/4), mirror, M and the spiral phase plate (SPP) acts as a vortex doubler setup [75] to modulate the Gaussian pump beam into optical vortices of order twice the phase winding of the SPP. With the help of two SPPs of phase winding corresponding to vortex order, *l*=1 and 2, in combination with the vortex doubler setup, we have modulated pump vortex order, l_p=1-5. A second λ/2 plate is used to adjust the polarization of the pump beam with respect to the poling direction of the nonlinear crystal for optimum phase-matching. The beam is focused at the center of the nonlinear crystal using a plano-convex lens of focal length, *f*=150 mm, corresponding to an estimated Gaussian pump beam waist radius of 40 µm. The singly-resonant OPO (SRO) is designed in a four mirror X-cavity configuration, with two curved mirrors, M1-M2, of the radius of curvature (ROC) of 150 mm and two plane mirrors, M3-M4. All OPO mirrors, M1-M3, have a high reflection for signal (R> 99.5%) across 1450-2100 nm, and high transmission (T> 90%) for pump (1064 nm) and idler across 2200-4000 nm. Mirror M4 acts as an output coupler to extract high intracavity power with 5% of

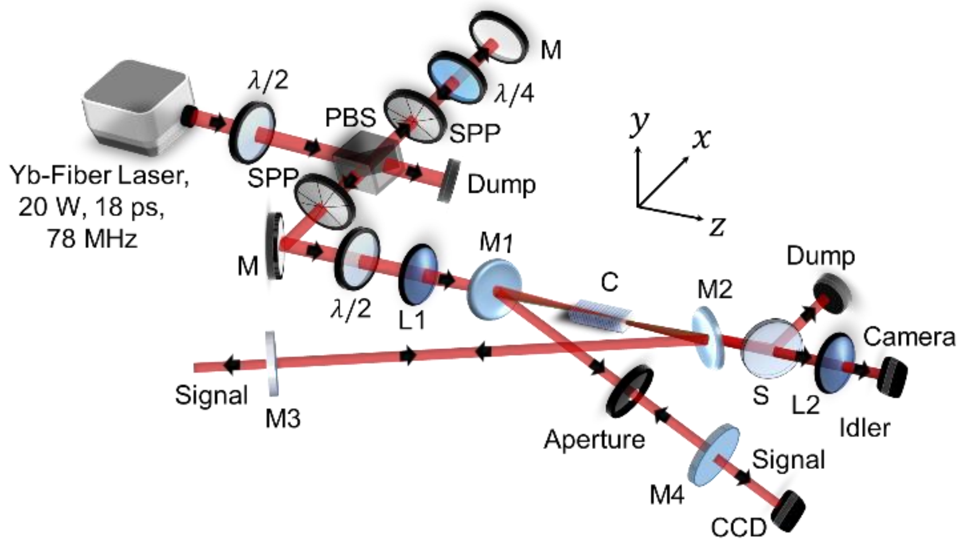

Figure 4.5. Schematic of the experimental setup. SPP, spiral phase plate; PBS, polarizing beam splitter; λ/2, half wave plate; λ/4, quarter wave plate; L1, focusing lens; PPLN, nonlinear crystal; M1-M4, OPO mirrors; S, wavelength separator; L2, idler collimating lens.

transmission for signal wavelength. The OPO is synchronized to the second harmonic of the repetition rate of the pump laser producing signal pulses at a rate of 160 MHz and idler at the pump repetition rate of 80 MHz corresponds to a total length of the cavity to be 938 mm. The nonlinear crystal for the vortex pumped picosecond mid-IR OPO is a 50-mm-long multi-grating MgO: PPLN crystal with an aperture of 8.1 × 1 mm^2 and grating period (Λ) varying from 29.05 to 31.5 µm. The end faces of the nonlinear crystal are antireflection coated

(R<0.5%) from 1450 nm to 2100 nm in the signal wavelength range. The nonlinear crystal is placed in an oven with a temperature variation of up to 200 °C with the thermal stability of ±0.1 °C. The idler output extracted from the undepleted pump and leakage signal using the wavelength separator S and subsequently imaged using the collimating lens, L2 and the camera. The spatial profile of the leakage signal of the high reflecting mirror, M4, is recorded using the CCD. The intracavity aperture is used to operate the OPO in fundamental cavity mode by eliminating the higher-order resonant cavity modes.

4.2.2 Results and discussion

To verify the generation of higher-order vortices in the mid-IR wavelength range, we adjusted the crystal temperature at 50°C and grating period, Λ=29.03 µm, which corresponds to signal wavelength of 1445 nm and idler at 4035 nm. Keeping the pump constant power at 5 W, well above the OPO threshold, we varied the order of the pump vortex and measured the spatial profile of the signal and idler with the result shown in Figure 4.6. As evident from the first column, (a-c), of Figure 4.6, the pump beams carry doughnut shaped intensity distribution with increasing dark core size with vortex order. To determine the order and sign of the optical vortices throughout the manuscript, we have used tilted lens technique [74], where an optical vortex of order, *l*, on propagation through a tilted lens, splits into |*l*|+1 lobes at the focal plane of the lens [74]. As evident from the tilted lens images shown in the second column, (d-f), of Figure 4.6, recorded at the back focal plane of the lens using a CCD camera having a pixel size of 4.4x4.4 μm^2, the pump vortices have orders of l_p = 1, 4 and 5. As reported [50,69,72], SRO configuration has low parametric gain in the CW pumping and the OAM of the pump beam directly transferred to the idler while the resonant signal maintains fundamental cavity mode (Gaussian beam) ensuring optimum spatial overlap among the interacting beams and OAM conservation in parametric processes. Additionally, in such cases, the OAM transfer mechanism observed for lower order (l≤2) pump vortices [48–50]. However, the increase of parametric gain with the use of ultrafast pump laser can produce OAM exchange in the SRO with different combinations of vortex orders for signal and idler satisfying OAM conservation and high value of spatial overlap integral among interacting beams. To avoid such OAM exchanges and restrict the pump OAM transfer to the mid-IR wavelength range, we have incorporated an intracavity aperture to limit the higher-order cavity modes of the resonant signal. As evident from the third column, (g-i), of Figure 4.6, the idler beam recorded using pyro-electric based camera with a pixel size of 85x85 μm^2 has doughnut shaped intensity profile with increasing dark core size and decreasing ring width with increasing pump vortex order. The tilted lens images as shown by the fourth column, (j-l), of Figure 4.6, confirm the order of the idler vortex to be l_i = 1, 4, and 5 same as that of the pump vortex order, l_p. Similarly, the corresponding signal beam as shown in the fifth column, (m-o), of Figure 4.6, caries Gaussian beam (l_s = 0) intensity profile for all pump vortex order, l_p, confirming the OAM conservation, $l_p = l_s + l_i$, even for high gain ultrafast SRO. Unlike the symmetric intensity distribution of the tilted lens images of the pump beam, the asymmetry in the tilted lens images of the idler can be attributed to the asymmetric intensity distribution of the idler vortex, especially at higher-order vortices. Such asymmetric intensity distribution of the idler vortex arises due to the increase of beam divergence influencing the spatial overlap of the interacting beams in the nonlinear crystal at higher order of the vortex. It is to be noted that the images of

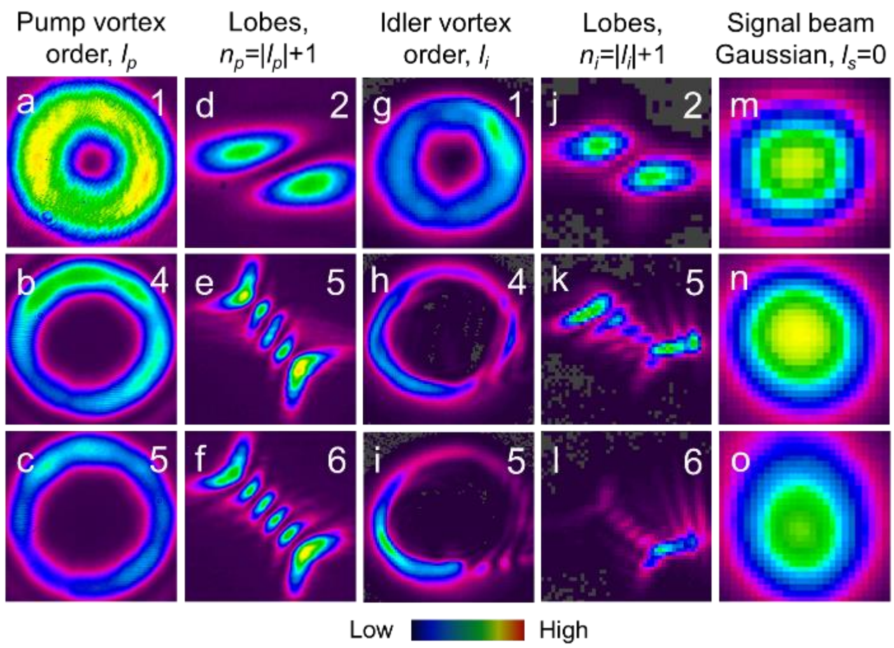

Figure 4.6. Far-field intensity distribution of the (a-c) pump beam profile for l_p=1, to 5, (f-j) tilted lens images of pump beam, (k-0) idler beam profile and (p-t) Corresponding idler tilted lens measurement, (u-y) signal beam profile.

Figure 4.6 have different spatial scales as these images have been recorded at different positions in the experiment. Contrary to previous reports, here, the high nonlinear gain due to the presence of ultrafast laser and longer interaction length of the nonlinear crystal enables the direct transfer of the higher order pump OAM mode to the idler radiation in an SRO enabling the generation of higher order optical vortices over wide wavelength range in the mid-IR spectrum.

Knowing the transfer of pump OAM to the idler wavelength and signal beam maintaining Gaussian spatial profile, we have studied the generation of higher-order optical vortices across the mid-IR wavelength range. Using multiple grating of the crystal ranging from 29.03 µm to 31.5 µm and varying the crystal temperature from 50°C to 180°C, we have studied the beam profile of idler beam across 2424 nm to 4035 nm as shown in Figure 4.7. Although we recorded the idler beams across the tuning range, for demonstration purpose, we have presented the idler spatial profile for arbitrarily selected three wavelengths, 2493, 2844 and 3866 nm and pump vortices of orders, $l_p = 1$, 4 and 5. As evident from the first column, (a-c), of Figure 4.7, the idler beam of pump vortex order, $l_p = 1$, has symmetric doughnut-shaped intensity profile across

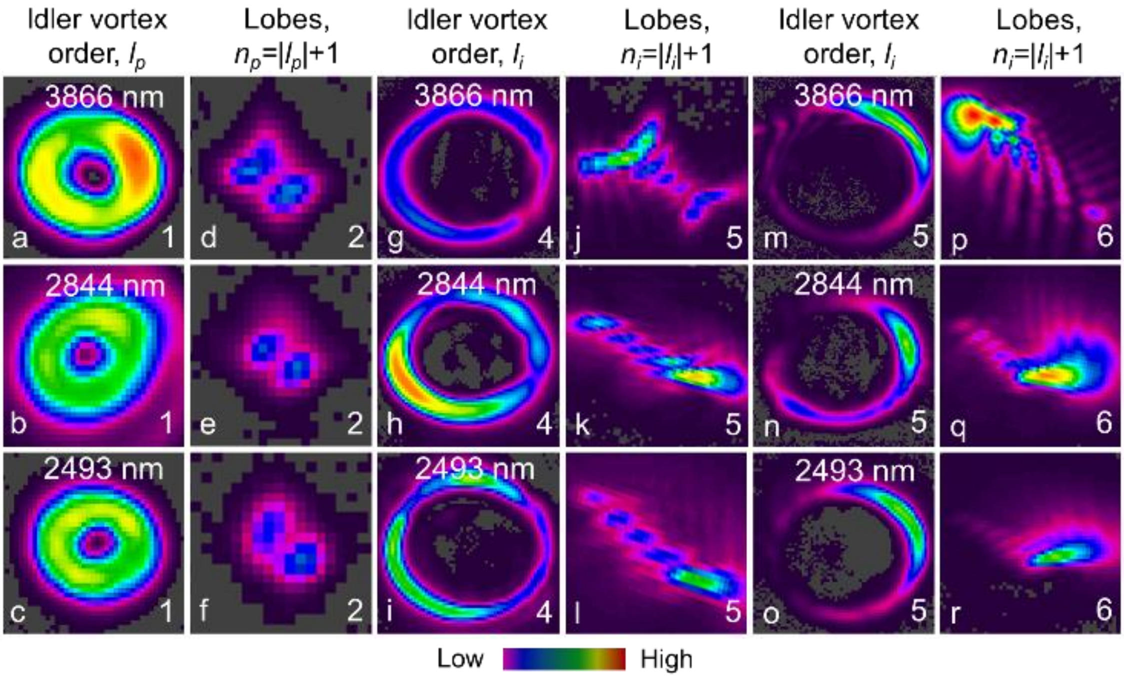

Figure 4.7. (a-c) idler beam profile for pump order 1, (d-f) tilted lens measurements, (g-i) idler beam profile for pump order 2, (j-l) corresponding tilted lens measurement, (m-o) idler beam profile for order 3-5 at 4035 nm, (p-r) corresponding tilted lens profile.

the tuning range with expected large annular width. The order of the idler vortex is confirmed to be l_i=1 using the tilted lens images as shown in the second column, (d-f), of Figure 4.7. As expected, the tiled lens images have symmetric lobe structure due to the symmetric intensity distribution of the idler vortex beam of order, l_i = 1. Similarly, the idler beams of pump vortex order, l_p = 4, have doughnut-shaped intensity profile with large dark core and narrow annual ring as shown in third column, (g-i), of Figure 4.7 which further confirmed to have vortex order, l_i = 4, using the tilted lens images as shown in fourth column, (j-l), of Figure 4.7. On the other hand, as evident from fifth column, (m-o), of Figure 4.7, the idler vortex across the tuning range have doughnut-shaped intensity profile with large dark core and thin annular ring for pump beam pump vortex order, l_p = 5, and confirmed to carry vortex order of l_i = 5 using the tilted lens image as shown in column, (p-r), of Figure 4.7. However, as expected, the idler beam has asymmetric intensity distribution and corresponding asymmetric lobe structure in the tilted lens images across the tuning range. It is to be noted that the signal beam, not shown here, across the tuning range has Gaussian spatial distribution, l_s = 0, confirming the OAM conservation, l_p=l_i+l_s. These experimental results prove the possibility of the generation of higher-order optical vortices tunable across 2424 nm to 4035 nm through the direct transfer of the pump OAM mode to the nonresonant idler radiation using a SRO.

We also measured the output power of the idler vortices across the tuning range. For a comparative study of the idler power variation for different idler vortex orders, we pumped the crystal with a constant power of 8 W and vortex orders of, l_p=1-3 and recorded the idler vortex power with the results shown in Figure 4.8. As evident from Figure 4.8(a), the output power of the idler vortex of order l_i=1 varies from 1.6 W to 658 mW for the wavelength variation from 2538 nm to 4035 nm. However, it is important to note that more than 60% of the entire tuning range of the SRO produces idler vortex beam of output power in excess of 1 W. Similarly, as evident from Figure 4.8(b) and Figure 4.8(c), the idler vortex power of the pump vortex orders, l_p = 2 and 3, vary from 1130 mW to 546 mW and 430 mW to 422 mW across the wavelength range of 2845-3924 nm and 2820-3862 nm respectively. It is important to note that the SRO produces more than 800 mW of output power across the 65% tuning range for idler vortex order l_i=2 and more than 400 mW idler power of vortex order l_i=3 over the entire tuning range in the mid-IR wavelength, making the current vortex source useful for a variety for applications. From the results of Figure 4.8, it is evident that the overall idler power decreases with the increase of pump vortex orders and for the same vortex order the idler power decreases for wavelength away from the degenerate wavelength of the SRO. While the decrease of the idler power with the increase of pump vortex order at constant pump power can be attributed to the decrease of the parametric gain of the SRO with the increase of the pump beam size and beam divergence with vortex orders. The decrease of the idler vortex power with wavelength can be attributed to the decrease of parametric gain for the generated wavelengths away from the degeneracy as commonly observed in OPOs. We should mention about the power variation for higher-order vortices.

We further studied the output characteristics of the higher-order vortex source with the results shown in Figure 4.9. Pumping the SRO with vortex orders, l_p = 1-5, we have measured the idler vortex power with the pump power at two different wavelengths, 2493 nm and 3860 nm with

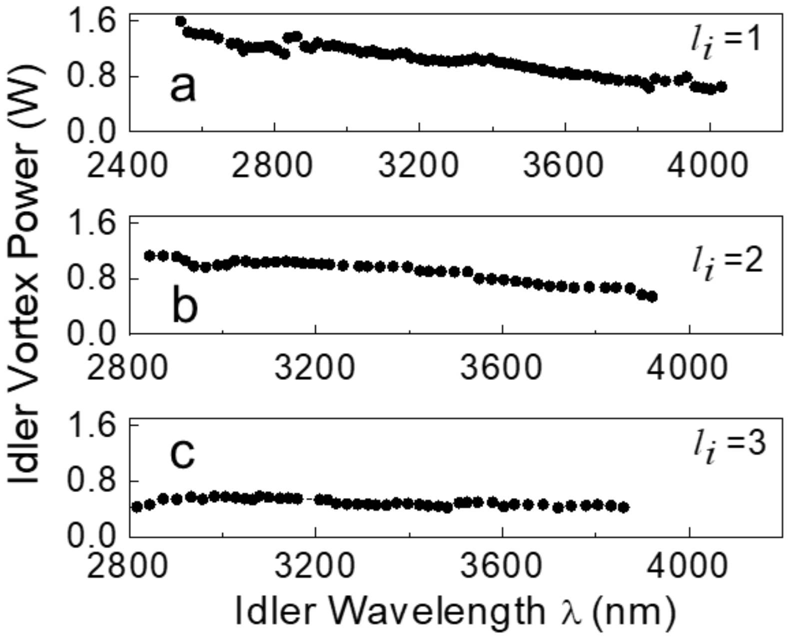

Figure 4.8. (a) power variation with idler wavelength for vortex order 1, (b) tunability curve for vortex order 2, (c) tunability curve for vortex order 3.

the results shown Figure 4.9(a) and Figure 4.9(b), respectively. As evident from Figure 4.9(a), the idler vortex power at 2493 nm increases linear to the pump power with the slope conversion efficiency of 23%, 21%, 19%, 11% and 12% and produced a maximum output power of 2.2 W, 1.9 W, 1.53 W, 0.78 W and 0.63 W for pump vortex order of l_p = 1, 2, 3, 4 and 5 respectively for constant power of 10 W. Similarly, the idler vortex power at 3860 nm as shown in Figure

4.9(b), increases with the pump power at the slope conversion efficiency of 9%, 7%, 6.5%, 4% and 3.3% and produces maximum idler vortex power of 0.8 W, 0.54 W, 0.3 W, 0.21 W and 0.16 W for the pump vortex order of lp=1, 2, 3, 4 and 5, respectively, at constant power of 10 W. It is interesting to note that the idler power of all orders do not show any sign of back conversion and roll-effect event at 10 W of pump power. Such observation clearly indicates the possibility of increasing the idler vortex power across the tuning range with a further increase of pump power. However, the crystal damage at high power for the ultrafast pump laser can be a limiting factor for the maximum available idler output power using the current experimental setup. Therefore, we have restricted the operation of the vortex pumped OPO to 10 W of pump power to avoid any chance of crystal damage. As also evident from Figure 4.9(a) and Figure 4.9(b), the threshold of the vortex pumped OPO increases with the pump vortex orders and the operation of OPO away from the degeneracy. To get further insight, we measured the OPO threshold at 2493 nm for different vortex orders of the pump with the results shown in Figure 4.9(c). As expected, the OPO has lowest operation threshold of 1.1 W for pump vortex order $l_p = 1$ and increases linear to the pump vortex order to 2.1 W, 3.8 W, 4.8 W and 6.2 W of average pump power of the ultrafast laser of orders, $l_p = 2$, 3, 4 and 5 respectively.

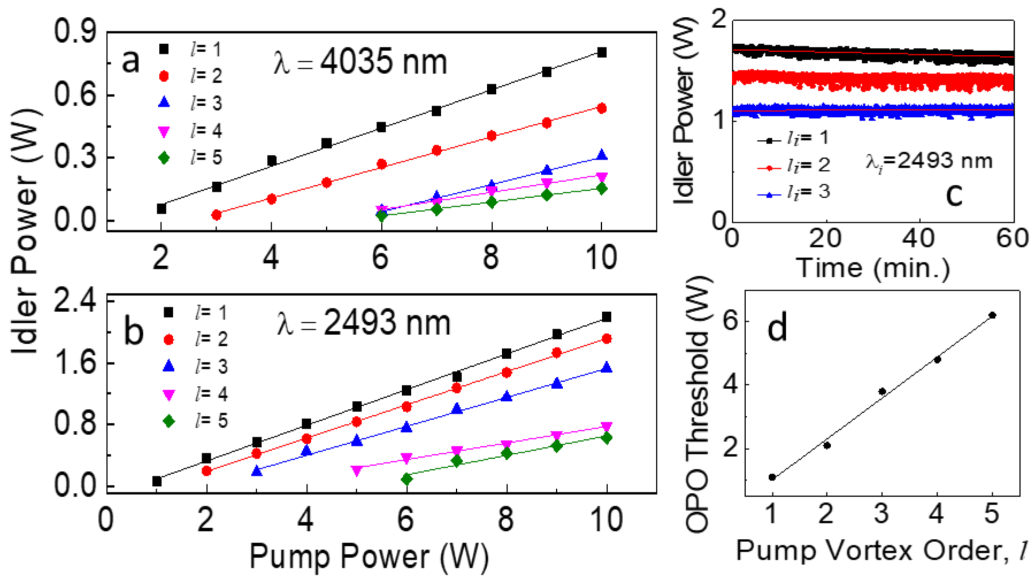

Figure 4.9. (a,b) Idler output power scaling at 4035 nm and 2493 nm respectively for pump vortex order 1 to 3, (c) power stability of idler output power for vortex order 1 to 3, (d) OPO threshold variation with pump vortex order.

However, it is to be noted that the stringent requirement of such high peak power of the pump beam to overcome the OPO threshold at higher vortex orders have restricted the successful generation of higher-order vortices (l>2) especially using CW OPOs till date. While one can address such stringent requirements using ultrafast lasers, however, the crystal damage effect is the limiting factor for the generation of a higher-order vortex (l>2) using CW OPO. We have further studied the power stability of the idler vortices at 2493 nm by keeping the pump power fix at 8 W and recording the output power of the idler of orders l_i = 1-3 for 60 minutes. The results are shown in Figure 4.9(d). As evident from Figure 4.9(d), the source shows a power fluctuation of 34 mW, 29 mW and 16 mW over the mean output power of 1.6 W, 1.42 W and 1.15 W of the idler of orders, l_i = 1, 2, and 3 respectively. Such idler power variation is the same as commonly observed in the case of OPOs and vortex pumping has little or no effect in the overall power stability of the vortex OPOs.

In this work, we have demonstrated the successful generation of high power and higher-order optical vortices tunable in the mid-IR wavelength range by directly transferring the pump vortices to the non-resonant idler beam of any ultrafast OPO. The source produces vortex beams of orders l_i = 1-5 tunability across 2493 nm to 4035 nm. The source produces idler vortices of maximum power ~2.2 W in vortex order 1 near to the degeneracy and all over we achieved a maximum output power of more than 1 W up to vortex order 3. This current scheme demonstrates for the first time generation of tunable optical vortices in this wavelength region in the ultrafast picosecond timescale. This scheme enabled the generation of a high order, high power optical vortices which have application in the various field of science and technology

4.3 Conclusion

In this chapter, we demonstrated the technique for vortex pumping in SRO configuration for achieving the high power higher-order optical vortices. Results and comparison of these two vortex sources with other demonstrated techniques by using nonlinear frequency conversion techniques are compared in the table below, whereas presented results in this chapter are highlighted in yellow.

Time-scale Pump characteristics	**Pump**	**Pump OAM** l_p	**Max. Signal OAM Generated** l_s	**Signal Power (mW)**	**Max. Idler OAM Generated** l_i	**Idler Power (W)**	**Tuning Range (nm)**	**Pulse duration**	**Ref.**
CW	Yb-fiber laser, 50 W, 1064 nm, Δν~100 kHz	2	0	-	2	5.2	2217–3574 (1357 nm)	-	Opt. Lett. **42**, 3674-3677 (2017)
Nanosecond	Q-switched Nd:YAG laser	2		2.1 mJ (max. pulse energy)		-	1953–2158 (205 nm)	18 ns	Opt. Express **20**, 23666-23675 (2012)
Nanosecond	Frequency doubled Q-switched Nd:YAG, 532 nm @50 Hz Δτ =25 ns,	1	1	2.36 mJ (max. pulse energy)	1	-	735-1903 (1168 nm)	<25 ns	Opt. Express **24**, 15204-15211 (2016)
Picosecond	Yb-fiber laser, 20 W, 1064nm, Δλ = 1.4 nm, Δτ = 20 ps Green pump	3	1	-	3	0.202	1102–1227 (125 nm)	-	Opt. Lett. **43**, 3606-3609 (2018)
Picosecond	Yb-fiber laser, 20 W, 1064nm, Δλ = 1.4 nm, Δτ = 20 ps	5	0	308	5	2.2	2538-4035 (1497 nm)	15 ps	Manuscript under preparation
Femtosecond	Yb-fiber laser, 5 W , 1064 nm, Δλ = 15 nm, Δτ = 270 fs	1	1	1.6	0	-	1433–1553 (120 nm)	637 fs	Journal of Optics, Vol. 20, No.1

Techniques demonstrated in this chapter are the first demonstration in the ultrafast time domain and enable to study OAM exchange dynamics in SRO. We demonstrated the mechanism for the generation of stable vortex sources with OAM order as high as 5 in the near-IR and mid-IR region of the spectrum. Work discussed in the last two chapters enabled us to generate high power higher-order scaler optical vortices in near-IR and mid-IR region, either directly from Gaussian pumped OPOs or vortex pumped OPO.

Chapter 5 Tunable optical vortex generation in ultraviolet

This chapter constitutes following publication

1) Varun Sharma, G. K. Samanta, S. Chaitanya Kumar, R. P. Singh, and M. Ebrahim-Zadeh, "Tunable ultraviolet vortex source based on a continuous-wave optical parametric oscillator," Opt. Lett. **44**, 4694-4697 (2019).

In previous chapters, we discussed the generation of vortex beams in the near-IR to the mid-IR region of the spectrum using OPOs. This chapter focus on the generation of scaler vortices in the ultraviolet region of the spectrum below 350 nm.

5.1 Introduction

Short-wavelength coherent sources in the ultraviolet (UV) are of great interest for a variety of applications in science and technology. While the majority of sources are based on Gaussian intensity distribution, and utilized in various applications including quantum optics [82], microsurgery [83], and spectroscopy [84]. With the evolution in sources in the short wavelength region, spatially engineering of such beams in vortices, have attracted a great deal of interest with application in the field of medical science [83], increasing the resolution of microscopy and spectroscopy [85,86]. Unfortunately, with absorption in the medium, damage threshold, limits liquid-crystal-based SLMs operation below 350 nm and SPPs are limited due to the fabrication technology in this wavelength region. Efforts have been extended to generate optical vortices in the UV by exploiting OAM conservation in nonlinear frequency conversion processes including second- harmonic-generation (SHG) and sum-frequency-generation (SFG) [41,87]. On the other hand, high-harmonic-generation (HHG) [88] provides an alternative method to transfer the pump optical vortices to discrete wavelengths in the UV spectral range. However, the limitation in the wavelength tunability of the input pump laser is directly transferred to the generated output vortex beam in the nonlinear conversion process. As a result, it is imperative to devise alternative methods to generate tunable vortex UV radiation using available laser sources in the visible and near-IR.

The use of intracavity and extracavity nonlinear frequency conversion processes have further extended the wavelength coverage of OPOs to the UV spectral range [89]. While conventional OPOs are pumped with Gaussian beams, recent efforts using vortex pump beams have led to the generation of vortex beams tunable across the near- to mid-IR [49,69]. The results of these experiments point to the possibility of generating optical vortices in the UV by deploying intracavity frequency conversion processes in vortex-pumped OPOs operating in the near-IR spectral range. In this work, we demonstrated, what is to our knowledge, the first demonstration of this approach, enabling the generation of optical vortices tunable across 332 nm to 344 nm in the UV spectral range. Using a continuous-wave (cw) green vortex beam to pump a singly-resonant OPO based on MgO-doped stoichiometric periodically-poled LiTaO3 (MgO:sPPLT) as the nonlinear gain medium, and deploying intracavity SFG of the undepleted pump and resonant signal tunable across 883-974 nm in the crystal of BiB3O6 (BIBO), we have generated optical vortex beams of order up to l_{uv} = 2 with maximum power of 12 mW tunable across

332-344 nm in the UV. In addition, the source produces idler vortex beam of order up to l_i=2 with an output power of up to 1.38 W, as well as Gaussian signal beam with a maximum power of 250 mW, tunable in the near-IR wavelength range.

5.2 Experimental setup

The schematic of the experimental setup for tunable vortex-beam OPO in the UV is shown in Figure 5.1. A cw laser (Verdi 10) centered at 532 nm with a maximum output power of 10 W in the Gaussian intensity profile is used as the pump source. The laser power to the OPO is controlled using a combination of a half-wave plate (λ/2) and a polarizing beam-splitter cube (PBS). The Gaussian pump beam is mode-converted into vortex beams of orders, l_p = 1 and 2, using two spiral phase plates, SPPs, having transverse thickness variation corresponding to the vortex of order 1 and 2. The second λ/2 plate adjusts the input pump beam polarization. A plano-convex lens of focal length, f=150 mm, is used to focus the pump beam at the center of nonlinear crystal to an estimated Gaussian beam waist radius of w_0~36 μm. The OPO is configured in a four-mirrors ring cavity comprising two curved mirrors, M1 and M2, with a radius of curvature, r=150 mm, and two plane mirrors, M3 and M4. All mirrors have high reflectivity (R>99%) for signal across 850-950 nm and high transmission (T>80%) for idler across 1100-1400 nm, ensuring singly-resonant oscillation. To achieve intracavity SFG between the resonant signal and undepleted pump, the mirrors, M2-M3, have high reflectivity (R>80%) for pump at 532 nm, while both M1 and M4 have high transmission (T>80%) at 532 nm, M4 also has high UV transmission (T>80%) across 310-390 nm. A 30-mm-long, 2-mm-wide, and 1-mm-thick MgO:sPPLT crystal with a single grating period of Λ=7.97 μm, and housed in an oven providing temperature control up to 200°C with a stability of ±0.1°C, is used as the nonlinear crystal (C1) for the OPO. The crystal end faces are antireflection-coated (R<1%) for 800-1100 nm. A 5-mm-long BIBO crystal (C2) of 8x4 mm^2 aperture, cut at θ=136° (ϕ=90°) in the optical yz-plane for type-I (ee→o) interaction, and placed between M3 and M4, is used for SFG of the undepleted pump and signal into the UV. The crystal is mounted on a rotation stage for angle tuning, and two wavelength separators, S1 and S2, are used to extract the idler from the leaked signal, and the UV from the undepleted pump and leaked signal, respectively. The spatial profile of the UV and signal are analyzed using a CCD camera.

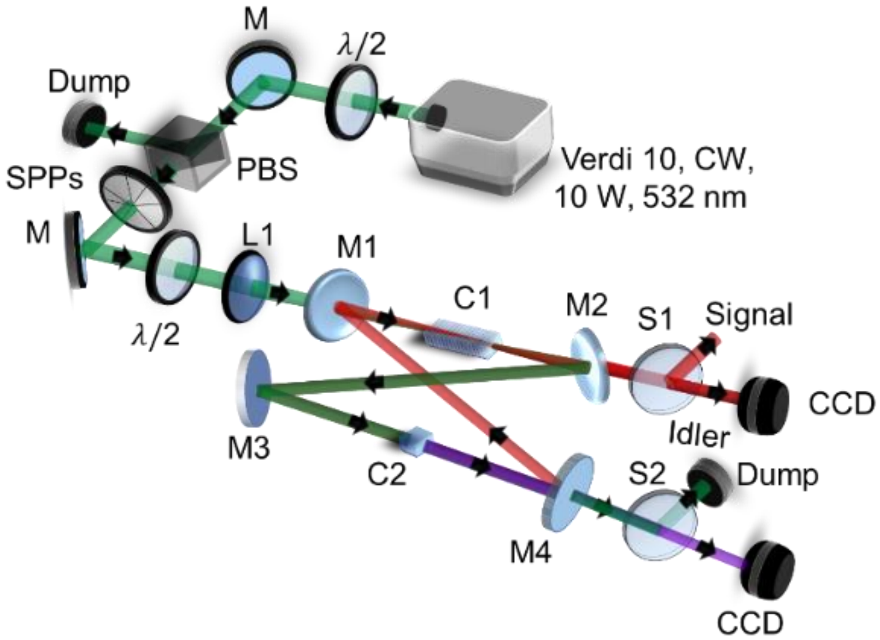

Figure 5.1. Schematic of experimental setup; λ/2: half-wave plate, SPP: spiral phase plate, PBS: Polarizing beam-splitter cube, SPP: spiral phase plate, L1: lens, M1-M4: OPO mirrors, C1: MgO:sPPLT crystal (in oven), C2: BIBO crystal, S1-S2: wavelength separators

5.3 Results and discussion

To study the vortex beam generation in the UV, we maintained the MgO:sPPLT crystal at a temperature of 124°C, corresponding to signal and idler wavelengths of 935 nm and 1234 nm, respectively, and pumped the OPO with vortex beam of order, $l_p = 1$. To confirm the OAM exchange mechanism, we first characterized the OPO without the intracavity SFG crystal. Under this condition, the vortex- beam-pumped OPO had an operation threshold of 3.4 W, slightly higher than that pumped by a Gaussian beam [90]. While pumping the OPO with a constant power of 6 W, we recorded the spatial profile of the pump, signal, and idler beams using a CCD camera with a pixel size of 4.4x4.4 μm^2. The results are shown in Figure 5.2. To confirm the order of the vortex throughout the experiment, we used the standard tilted lens technique [74], where the vortex beam of order, l, on propagation through a lens tilted in the transverse plane, splits into $|l|+1$ number of characteristic lobes at the focal plane of the lens. By counting the number of lobes, one can confirm the order of optical vortices. For the tilted lens technique, we used a lens of focal length, f = 400 mm. As evident from the first row, (a-d), of Figure 5.2, the pump beam has doughnut-shaped intensity profile as shown in Figure 5.2(a, c), and the titled lens images as shown in Figure 5.2(b, d), confirm the order of the pump vortex to be l_p = 1 and 2. According to the OAM conservation in an OPO, the OAM of the pump can be transferred either to signal and idler with equal probability or shared by both signal and idler. However, as previously reported in [69], in the case of a singly-resonant OPO, the OAM or the vortex order of the pump beam is directly transferred to the idler and the resonant signal maintains the fundamental cavity mode. To confirm the mode selection in the OPO, we imaged the signal beam leakage through M2 after separating from the idler. The results are shown in the second row, (e-h), of Figure 5.2. As evident from Figure 5.2(e, g), the signal beam intensity distribution resembles Gaussian mode (l_s = 0) for both pump vortex orders, which is further confirmed from the straight-line fringes, see Figure 5.2(f, h), recorded by the self-interference of the signal beam using the Mach-Zehnder interferometer. The third row, (i-l) of Figure 5.2, shows the corresponding idler beam to carry doughnut-shaped spatial intensity profiles, see Figure 5.2(i, k). Using the tilted lens images, shown in Figure 5.2(j, l), we confirm the order of the idler to be l_i = 1 and 2, same as that of the pump vortex orders, verifying the OAM conservation in the OPO.

After the successful operation of the OPO with the resonant signal in Gaussian mode and idler in the vortex profile, we inserted the BIBO crystal between M3 and M4. The OPO threshold increased to 4.2 W and 6 W for pump vortex of order l_p=1 and 2, respectively, due to the coating loss on the BIBO crystal facets. On the other hand, the higher OPO threshold for pump vortex of order, l_p = 2, as compared to the pump vortex order, l_p = 1, can be attributed to the increase in pump beam size with the vortex order at the center of MgO:sPPLT crystal and subsequent reduction in parametric gain. For better overlap between the undepleted vortex pump and resonant Gaussian signal in the BIBO crystal, we have designed the OPO cavity using Gaussian beams and the ABCD matrix formalism ensuring identical confocal parameters for the interacting beams in both the crystals. Adjusting the tilt of the BIBO crystal for perfect phase-matching, we recorded the wavelength of SFG radiation between the undepleted vortex pump of order, l_p = 1 and 2, and the resonant Gaussian (l_s = 0) signal at 935 nm to be 339 nm. As evident from fourth row, (m-p), of Figure 5.2, the UV radiation has doughnut-shaped intensity profile, Figure 5.2(m, o), with vortex order, $l_{uv} = l_p + l_s$ = 1 and 2, in accordance with OAM conservation in SFG process, as confirmed by the tilted lens images, 6.2(n, p). It is to be noted that, a prism (not shown in Fig.) was used to separate any residual signal and pump from the UV vortex beam. The poor image quality of the vortex beam in the UV is due to the low sensitivity of the silicon CCD camera below 350 nm. However, the splitting of optical vortex dark core of UV vortex beam of order, l_{uv} = 2, is attributed to various parameters including the birefringence and spatial walk-off effect in the BIBO crystal [64], astigmatism due to the curved cavity mirrors, and dispersion of the prism used to extract the UV radiation. Further improvement in the spatial profile and output power of the UV vortex beam could be expected by using non-critical phase-matched crystals for the SFG process. We used the same CCD camera to record the idler wavelength despite the low sensitivity of the silicon CCD for

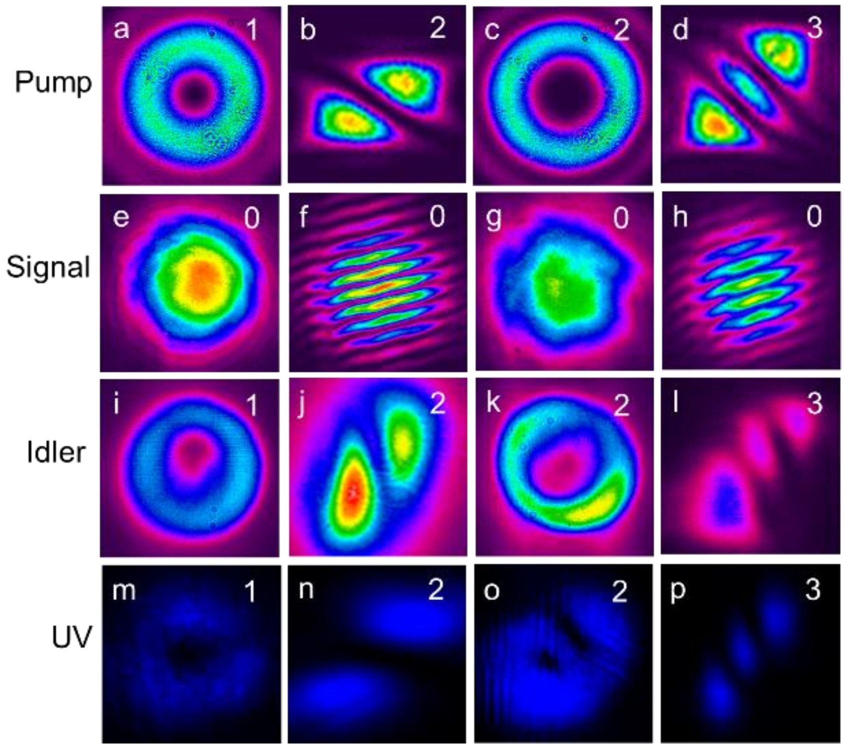

Figure 5.2. (a-d) Intensity profile and tilted lens images of pump beam of vortex order, lp = 1 and 2. (e-h) Intensity profile and interference pattern of the signal, and (i-l) corresponding intensity profile and tilted lens images of the idler. (m-p) Intensity profile and the tilted lens pattern of the UV beam generated from pump vortex of order, lp = 1 and 2. Spatial profile of signal, idler and UV beams have different scales.

wavelengths above 1100 nm. Since we did not measure the beam width of the idler vortices in the current experiment, the significant blooming effect of the CCD camera for wavelengths beyond 1100 nm does not have any impact on our results throughout the work. Due to higher available power and the non-critical phase matching of PPSLT crystal, the idler vortices have a superior spatial profile as compared to the UV radiation.

We have studied the tuning capability of the vortex beam source. Using pump vortex of orders, l_p = 1 and 2, at a constant power of 7 W, we tuned the OPO across 883-974 nm in the signal, with the corresponding idler across 1338-1172 nm, by changing the crystal temperature from 84°C to 188°C. By varying the phase-matching angle of the BIBO crystal, we recorded the intensity profile of the UV radiation across 332-344 nm, with the results shown in Figure 5.3. As evident from the first column, (a-d), the UV radiation recorded at four different wavelengths, 332 nm, 335 nm, 339 nm, and 344 nm, across the tuning range, has doughnut-shaped intensity profile for the pump vortex of order, l_p = 1. Counting the number of lobes, $n_{uv} = l_p + 1$, of intensity pattern recorded using the tilted lens, as shown in the second column, (e-h), we confirm the order of the UV vortex to be, l_{uv} = 1, the same as that of the pump order, l_p = 1, across the tuning range. Similarly, for pump vortex order, l_p = 2, we observe the UV beam to carry doughnut-shaped intensity pattern, as shown in the third column, (i-l), across the tuning range. The tilted lens images, as shown in the fourth column, (m-p), confirm the order of the UV beam to be l_{uv} = 2 across the tuning range. The splitting of the UV vortex of order, l_{uv} = 2, can be attributed to the birefringence of the BIBO crystal influencing the spatial overlap of pump and signal beams throughout the interaction length, as also observed for Gaussian beam-pumped OPO generating UV [89,90]. Due to the unavailability of SLM for UV wavelengths, we could not measure the purity of the UV vortices. Although the image quality of the vortex beams of all orders are highly influenced by the low sensitivity of the CCD camera at UV wavelengths, the relatively inferior intensity profile of the vortex beam of order, l_{uv} = 2, as compared to that of the vortex order, l_{uv} = 1, is attributed to the astigmatism of the curved OPO cavity mirrors for higher-order pump vortices, and also the lower output power of the UV radiation. It is to be noted that the idler beam (not shown here) carries vortex beam of order, $l_i = l_p$, across the entire tuning range, while the signal has Gaussian spatial profile (l_s = 0), satisfying OAM conservation in an OPO. It is to be noted that the further increase in the wavelength tunability of the UV vortex requires suitable broadband AR coated mirrors and increased nonlinear gain of the OPO using a pulsed laser to pump the OPO.

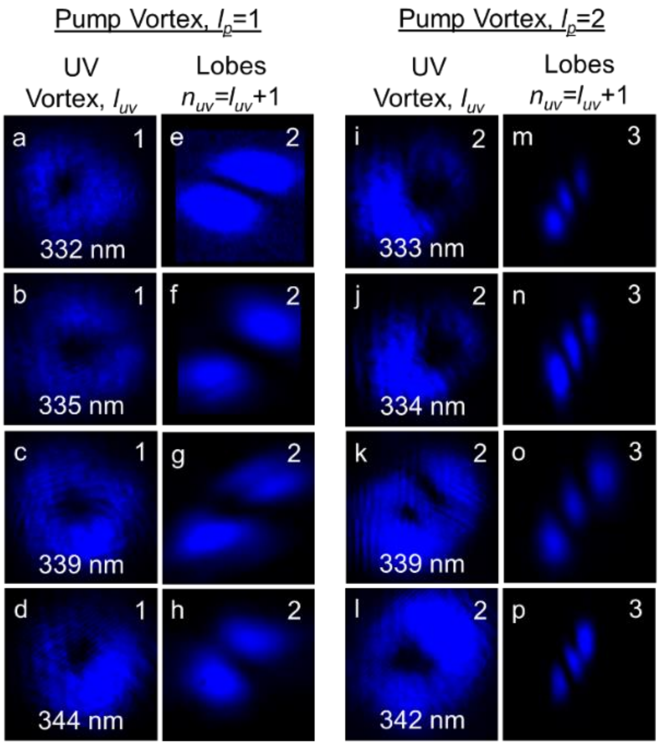

Figure 5.3. (a-d) Intensity profile, and (e-h) tilted lens images of UV beam generated by pump vortex of order, lp = 1. (i-j) Intensity profile, and (m-p) tilted lens images of the UV beam generated by pump vortex of order, lp = 2, across the tuning range.

We also measured the UV vortex power across the tuning range, while keeping the pump power constant at 7 W. The results are shown in Figure 5.4. As evident from Figure 5.4(a), the output power of UV vortex beam of order, l_{uv} = 1, varies from 5.2 mW at 332 nm to 7 mW at 344 nm, reaching a maximum of 11 mW at 341.3 nm, with >7 mW over 90% of the entire tuning range. Similarly, the output power of the UV vortex beam of order, l_{uv} = 2, varies from 3 mW at 333 nm to 4.5 mW at 338 nm, reaching a maximum of 5.6 mW at 336 nm. Although, we recorded the intensity profile of the UV vortex beam across the entire tuning range, the output power was measured to be below 1 mW. The more confined tuning range of the UV vortex of order, l_{uv} = 2, can be attributed to the lower parametric gain and higher threshold of the OPO due to the larger beam size of the pump vortex of order, l_p = 2. We also measured the idler vortex and leaked signal power across the tuning range. The results are shown in Figure 5.4(b). As evident, the output power of the idler vortex of order, l_i = 1, varies from 460 mW at 1338 nm to 1.12 W at 1172 nm, with a maximum of 1.3 W at 1248 nm. On the other hand, the output power of the idler vortex of order, $l_i = 2$, varies from 160 mW at 1320 nm to 420 mW at 1243 nm. The leaked signal beam in Gaussian spatial profile generated by the pump vortex of order, $l_p = 1$ and 2, delivers an output power in excess of 150 mW and 80 mW, respectively, with a maximum of 290 mW at 902 nm for pump vortex of order, $l_p = 1$.

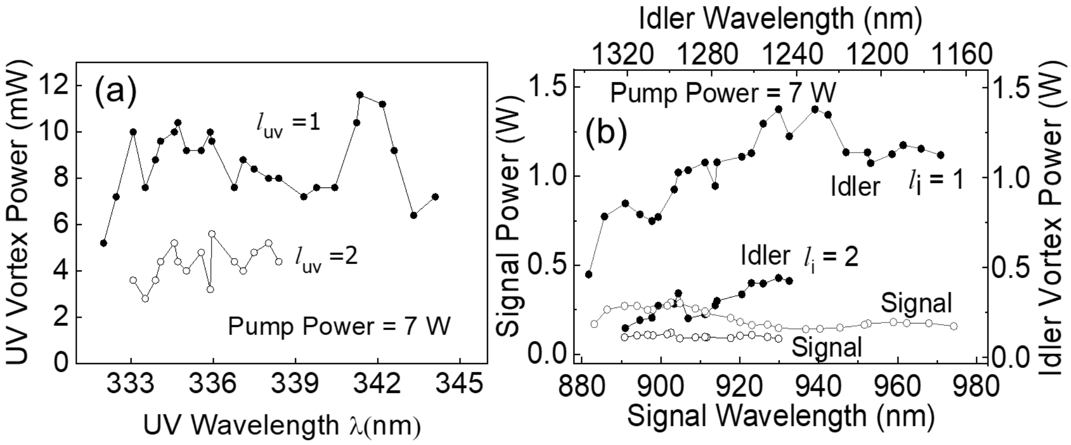

Figure 5.4. Variation of output power of (a) UV vortex beams of order, luv = 1 and 2, and (b) idler vortex beam of order, li = 1 and 2, and Gaussian signal beams across the tuning range, generated by pump vortex of order lp = 1 and 2.

We further studied the power scaling characteristics of the UV vortex OPO. Keeping the MgO:sPPLT crystal temperature fixed at 104°C, producing signal and idler at 897 nm and 1308 nm, respectively, corresponding to the UV wavelength of 334 nm, we measured the UV, idler and leaked signal power as a function of the pump power of vortex order, $l_p = 1$. The results are shown in Figure 5.5. As evident from Figure 5.5(a), the UV vortex power and the single-pass UV efficiency vary quadratically and linearly, respectively, with the vortex pump power, producing a maximum UV power of 12 mW at a single-pass efficiency of 0.17%. We did not observe any sign of saturation in the UV power, which is also confirmed by the variation of UV power with the square of the pump power, as shown in the inset of Figure 5.5(a), up to the maximum available pump power of 7 W. We also measured the idler vortex beam power and the leaked Gaussian signal beam with input pump power. As evident from Figure 5.5(b), we obtained a maximum idler vortex power of 782 mW and a corresponding useful leaked signal power of 250 mW in Gaussian profile for a maximum available pump power of 7 W. The tighter focusing of the interacting beams can increase the UV power at the cost of poor UV vortex profile leaving a trade-off between the spatial profile and output power of the UV vortex.

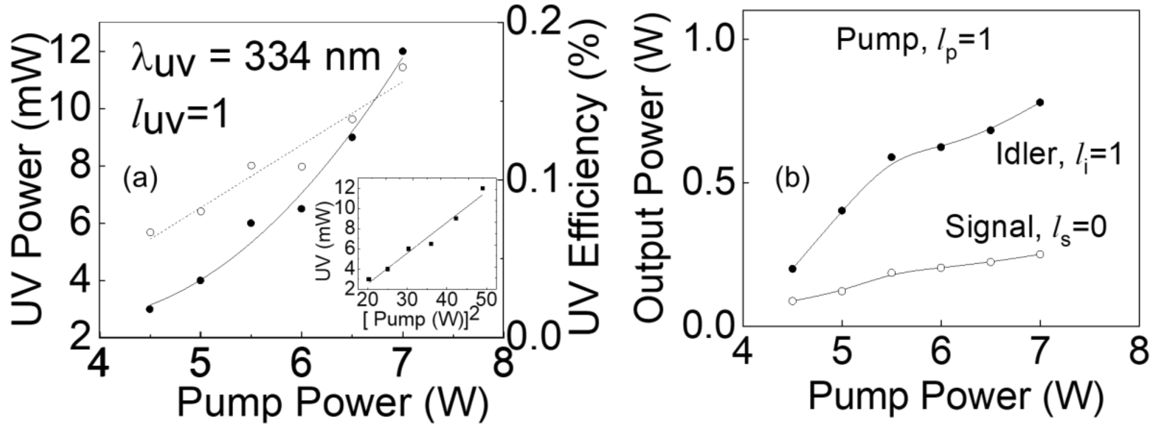

Figure 5.5. (a) Dependence of UV vortex power and efficiency on the pump vortex power. (Inset) Variation of UV vortex power with square of the pump power. (b) Variation of idler vortex power and corresponding Gaussian signal power as function of input pump power.

5.4 Conclusion

In conclusion, we have demonstrated a viable source of tunable optical vortex radiation based on a cw OPO, providing practical powers in UV as well as the near-IR spectral range. By deploying a green vortex pump beam of order, l_p = 1 and 2, in combination with intracavity SFG, we have generated UV vortex beam of order, l_{uv} = 1 and 2, tunable across 332-344 nm, with a maximum cw output power of 12 mW. The OPO also delivers near-IR idler vortex beam of order, l_i = 1 and 2, tunable across 1172-1338 nm, with a maximum power of 1.3 W, as well as signal radiation in Gaussian spatial profile with a usable maximum power of 250 mW tunable across 883-974 nm. These characteristics make the OPO a highly versatile and practical source of optical vortex radiation across extended spectral regions in the UV and near-IR

Chapter 6 Tunable vector vortex beam OPO

This chapter constitutes the following journal publications:

1) V. Sharma, S. C. Kumar, G. K. Samanta, and M. Ebrahim-Zadeh, " Tunable vector-vortex beam optical parametric oscillator," Scientific Reports, 9, 9578 (2019).

In the previous discussions, we focused on the generation of scaler optical vortices, with polarization uniform all across the beam. Our focus was on the generation of such beams with high power and broad wavelength tunability. In this chapter, we are going to study a different class of beams known as vector beams, and their generation, using OPO.

6.1 Introduction

Light beams carry angular momentum in the form of spin and orbital angular momentum (OAM). While spin angular momentum (SAM) is associated with the polarization of the light field, OAM is attested to the helicity to the Poynting vector of the optical field. While optical vortices have found a great deal of interest in a variety of fields including communication [91], lithography [11], and high-resolution microscopy [37], in most cases these beams are scalar vortex beams where the polarization of the beam is the same across the entire beam. However, in addition to the phase singularity, optical vortices can carry polarization singularity. Due to the vector nature (polarization), together with the vortex intensity distribution, such special class of beams are known as vector-vortex beams. Vector-vortex beams, having both phase and polarization singularities, are of great interest for a variety of applications, for example, in material processing [92], optical trapping [93], photon entanglement [94], and microscopy [95]. The vector-vortices are described by points on the higher-order Poincaré sphere (HOP) [96], representing the total angular momentum of light.

The generation of vector-vortex beams or HOP beams requires manipulation of polarization and spatial mode of a laser beam. Typical techniques to generate such beams external to the optical cavity involve q-plates and phase retarders [97], nematic spatial light modulator [98], spatially varying retarders [99], or superposition methods [100]. On the other hand, efforts have been made for direct generation of such beams internal to the laser cavity by exploiting the birefringence and thermal properties of the gain medium [101], by incorporating intracavity optical elements such as axicon [102], or by a combination of q-plate and quarter wave plates [15]. Unfortunately, the limited spectral coverage of lasers and material dispersion of intracavity and extracavity optical components manipulating the polarization and spatial mode of a laser beam restrict all these existing techniques, thus precluding vector-vortex beam generation over a wide spectral range.

Using OPOs providing scalar vortex beams, one can, in principle, manipulate the polarization of the intracavity field to generate vector-vortex beams directly from OPOs. However, the phase-matching condition is critically dependent on the polarization of the interacting beams, dictating the parametric gain for the nonlinear process. Therefore, manipulating the polarization of intracavity beams in an OPO, as required for vector-vortex generation, is very challenging.

In this work, we demonstrated a generic experimental scheme to generate a tunable vector-vortex beam directly from an OPO. Taking advantage of the directional property of the OPO (nonlinear gain in the direction of the pump beam), we manipulate the resonating beam in such a way that the polarization state is preserved after every round-trip, enabling efficient frequency conversion in the presence of the pump beam. Consider a standing-wave Fabry-Perot cavity, as shown in Figure 6.1(a). The nonlinear gain can be achieved in both clockwise and counter-clockwise directions with the resonating beams having vortex spatial structures when the gain medium is pumped with vortex beam of linear polarization (say, vertical) from both sides. The inclusion of two quarter-wave plates (QWP) with optic axis rotated by 45° with respect to horizontal axis ensures that the polarization state is always linear in region A and circular in region B. In every round-trip, the resonating beam in region A returns to its initial polarization state (vertical) to ensure efficient frequency conversion in the gain medium. Here, the manipulation of polarization and spatial mode of the output beam, as required for vector-vortex beams, is achieved by the intracavity QWP and the OAM conservation in the parametric process, respectively. Using such a scheme in a nanosecond OPO in doubly-resonant (DRO) configuration and pumped in both directions by optical vortex beam, we generate vector-vortex beam of order, l=1, tunable over 964-990 nm with an output power in excess of 5 mW.

6.2 Experimental setup

The schematic experimental setup is shown in Figure 6.1(b). A Q-switched Nd:YAG laser producing 5 W of average power at 1064 nm in 6.6 ns pulses at a repetition rate of 30 kHz, works as the fundamental source. Using a lens (L1), the fundamental laser is frequency-doubled in a 30-mm-long LBO crystal, providing up to 1.5 W of green power at 532 nm in the Gaussian intensity profile. After separation from the fundamental using a dichroic mirror (S1), the green pump beam is collimated using a lens (L2), with the input power to the experiment controlled using a combination of a half-wave plate (λ/2) and a polarizing beam-splitter (PBS) cube. A spiral phase plate (SPP) is used to convert the green Gaussian pump beam into an optical vortex of order, $l_p = \pm 1$. The green pump vortex is divided into two beams, PB1 and PB2, of equal intensity, by using a non-polarizing 50:50 beam-splitter (BS) cube. Further, the two beams are steered to the DRO with an equal number (three) of reflections, in order to maintain the same vortex polarity, $l_p = 1$, for both PB1 and PB2. The path length of the pump beams is also maintained to be identical. The DRO is configured in a four-mirror standing-wave cavity with two concave mirrors, M1-M2 (r=100 mm), and two plane mirrors, M3 and M4, with a total cavity length of 33.5 cm, allowing six roundtrips of the resonant waves over the 6.6 ns pulse duration. All mirrors are antireflection-coated for high transmission (R<5%) at 532 nm and high reflectivity (R>95%) across 950–1200 nm, ensuring DRO operation over the signal and idler wavelength range [49]. A 30-mm-long, 1-mm-wide, and 0.5-mm-thick periodically-poled congruent $LiTaO_3$ (PPCLT) crystal with a single grating period of Λ_c=7.91 µm, placed between M1 and M2, is used as the nonlinear crystal. The crystal is housed in an oven, adjustable from room temperature to 200°C with a stability of ±0.1°C. The $\lambda/2$ plate before SPP adjusts the pump beam polarization for optimum phase-matching of PPCLT crystal. The nonlinear crystal is pumped from both sides using two identical lenses (L3) of focal length, f=150 mm, ensuring identical mode-matching and all cavity parameters for OPO operation in both clockwise and counter-clockwise directions. QWP1 and QWP2, optimized for the signal wavelength centered at 980 nm, placed inside the DRO cavity, are used to manipulate the polarization state of the resonating beam. The leakage signal and idler of M3 are separated by the separator, S2, and recoded by CCD and pyro-camera, respectively. The working principle of our experimental scheme can be understood as follows. The PPCLT crystal is designed for type-0 ($e \rightarrow e+e$) quasi-phase-matched interaction with vertical polarization states for the pump, signal and idler. On the other hand, the OAM of the pump beam with vortex order, l, can be transferred either to the signal or idler through systematic control of the cavity losses [49]. Therefore, due to higher losses of the cavity mirrors at the idler wavelength than the signal, the pump OAM is transferred to the signal, while idler carries order, $l = 0$ (Gaussian).Under this condition, the pump beam, PB1, creates signal with the state (polarization and OAM) of $|V, l\rangle$, and the corresponding idler state of $|V, 0\rangle$. As each reflection flips the OAM from $+l$ to $-l$ and vice-versa, the states of the signal beam before and after the QWP1, with optic axis at +45°, are $|V, -l\rangle$ and $|R, -l\rangle$, respectively. The mirror, M3, on reflection, changes the state of the signal beam into $|L, l\rangle$, which, on passing through QWP1, is converted into $|H, l\rangle$. Here, V and H correspond to the vertical and horizontal polarization, while R and L represent the right and left circular polarizations. Similarly, the state of the signal beam before QWP2, and after successive reflection by M2 and M1 is |H, l ⟩, which on propagation the state into |R, -l ⟩, which is further transformed into |V, -l ⟩ by QWP2. As a result, the signal beam produced by the pump, PB1, after one round-trip returns to its original state, |V, l ⟩, and is amplified by the pump beam. Similarly, the signal beam generated by the pump beam, PB2, of state |V, l ⟩, has the state of |L, l ⟩ and |R, -l ⟩ before M3 and M4, respectively. As a result, the signal beam out-coupled from M3 and M4 has state, |R, -l ⟩ + |L, l ⟩, which is the final state of the generated vector-vortex beam. Since QWP1 and QWP2 are not optimized at the idler wavelengths, in each round-trip the idler beam of vortex order, l = 0, generated by both pump beams, will encounter extra losses due to the improper (elliptical) polarization rotation by the QWPs, which in turn results in the idler carrying OAM of order, l = 0, satisfying the OAM conservation in DRO.

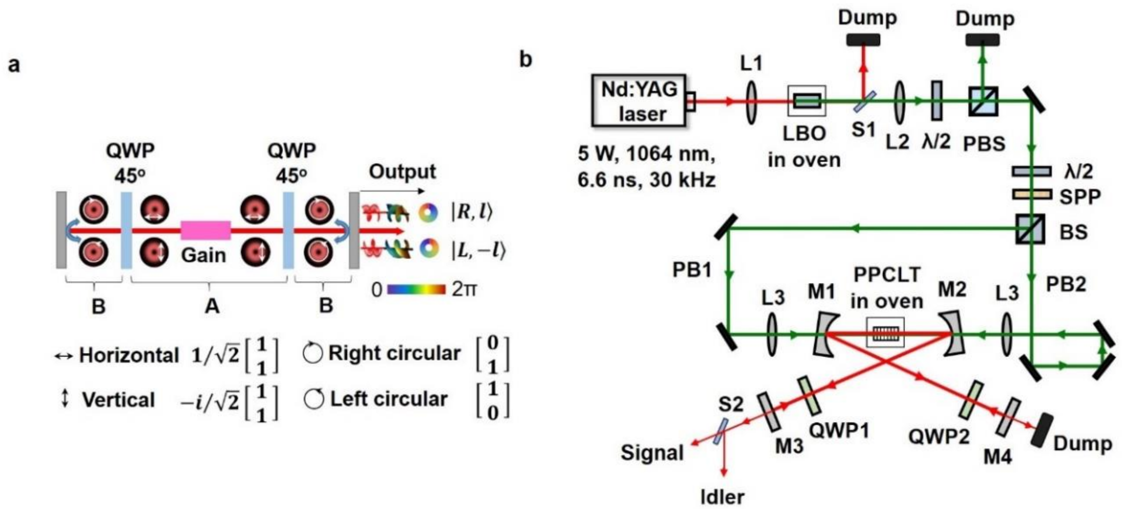

Figure 6.1. Vector vortex beam optical parametric oscillator. (a) Pictorial representation of the evolution of polarization and OAM states of the resonant beam, through one roundtrip in the OPO cavity, horizontal, vertical, right circular and left circular represent the polarization of resonating beam light. (b) Schematic of the experimental setup. λ/2, half-wave plate; PBS, polarizing beam-splitter; BS, 50:50 beam-splitter; SPP, spiral phase plate; L1-3, lenses; M1-4, OPO mirrors; QWP1-2, quarter-wave plates; LBO, PPCLT, nonlinear crystals; S1-2, wavelength separators.

6.3 Results and discussions

To study the OAM exchange mechanism of the nanosecond DRO, we fixed the crystal temperature at 77°C, corresponding to the signal (idler) wavelength of 977 nm (1168 nm). Pumping the crystal with PB1 and PB2, separately, with an average power of 300 mW and vortex order of $l_p = 1$, we recorded the spatial intensity profile of the signal and idler beams, with the results shown in Figure 6.2. As expected, both the pump beams, PB1 and PB2, derived from a single pump beam, carry the same doughnut-shaped intensity profile (first column, (a, b), of Figure 6.2). The number of characteristic lobes, ($n_p = | l_p | + 1$), and their orientation, as shown in second column, (c, d), of Figure 6.2, recorded using the tilted lens technique [74], confirm that both the pump beams (PB1 and PB2) carry vortex beam of same order, $|l_p| = 1$, and, same helicity (sign). The third column, (e, f), of Figure 6.2, shows the intensity profile of the signal beams generated by PB1 and PB2, respectively. The signal

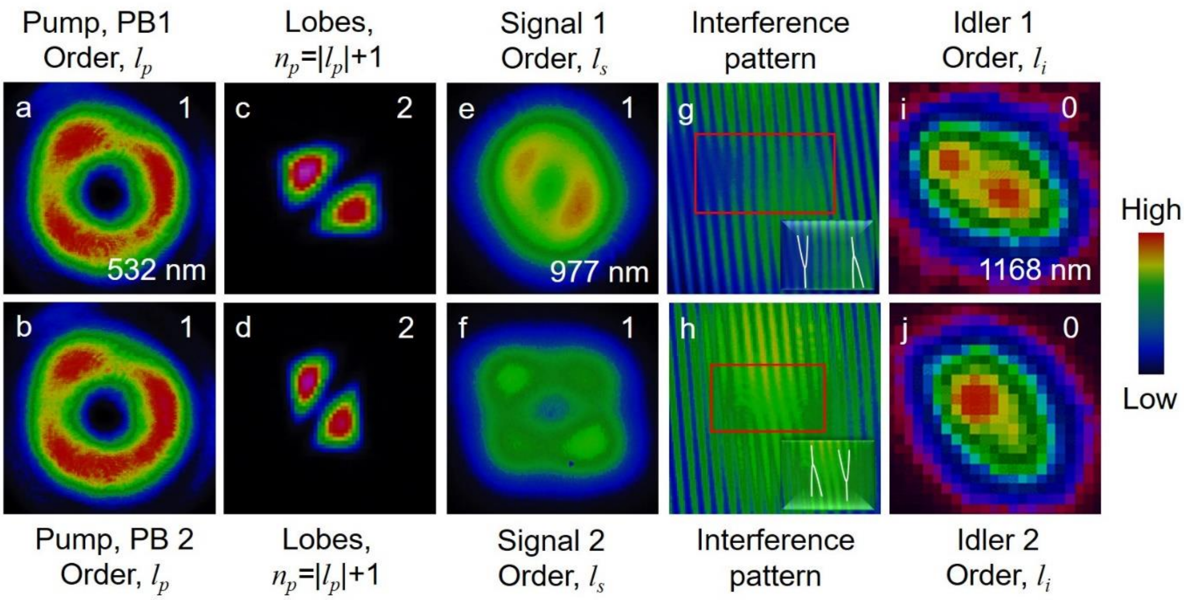

Figure 6.2. Generation of vortex beam. (a, b) Intensity profiles and (c, d) lobe structure of the pump beams, PB1 and PB2. (e, f) Intensity distribution and corresponding (g, h) self-interference fringe pattern of the signal beams generated by PB1 and PB2. (i, j) Idler intensity profiles generated by PB1 and PB2

beams have a doughnut-shaped intensity profile with the central minimum, resembling a vortex beam, which is further confirmed by the characteristic fork pattern of the vortex-vortex interference recorded using Mach-Zehnder interferometer. As evident from the fork pattern and their orientation, shown in the fourth column, (g, h), of Figure 6.2, both the signal beams carry vortex of order, $|l_s| = 1$, but with opposite sign (±). The opposite sign of the signal vortices, as required for vector-vortex generation, can be attributed to the odd and even number of reflections experienced by the signal beams generated by PB1 and PB2 vortices of the same sign, respectively, before transmission through the mirror, M3. Unlike the pump vortices, the signal vortices have background intensity at their dark core, which is due to the presence of the OPG signal generated by the high gain of the PPCLT crystal under nanosecond laser pumping. In our experimental setup, we observed OPG of the vortex pump beam at an input power of 350 mW. For OPO operation, we adjusted the pump power below the OPG threshold. Under this condition, we still observed background OPG signal due to the high intra-cavity power. The fifth column, (i-j), of Figure 6.2, shows the intensity profiles of the corresponding idler beams in the Gaussian intensity profile, without any dark core in the beams. The elliptic beam profile of the idler is attributed to tilts in the collection optics. Such observation clearly confirms that in nanosecond vortex-pumped DRO, the pump OAM is directly transferred to the signal beam ($l_s = l_p$), while the idler beam maintains Gaussian spatial mode (l_i =0), owing to OAM conservation ($l_p = l_s + l_i$) in the parametric process [49]. The pixelated image of the idler intensity distribution can be attributed to the large pixel size of the pyro-camera. Knowing the generation of signal scalar-vortex beams for both pump beams (PB1 and PB2), using a spectrometer, we measured the wavelength of signal beams to be 977 nm separately for both pumps. However, with both pump beams present in the crystal, the resultant signal beam spectrum shifted by 1 nm to 976 nm as shown in Figure 6.3. Such a shift in the signal spectrum could be attributed to a minor temperature change (~0.6 ºC) in the crystal due to high intra-cavity signal as well as the pump power. Since both signal beams have same wavelength and polarization, we expect coherent coupling between the signal pulses generated by both pump

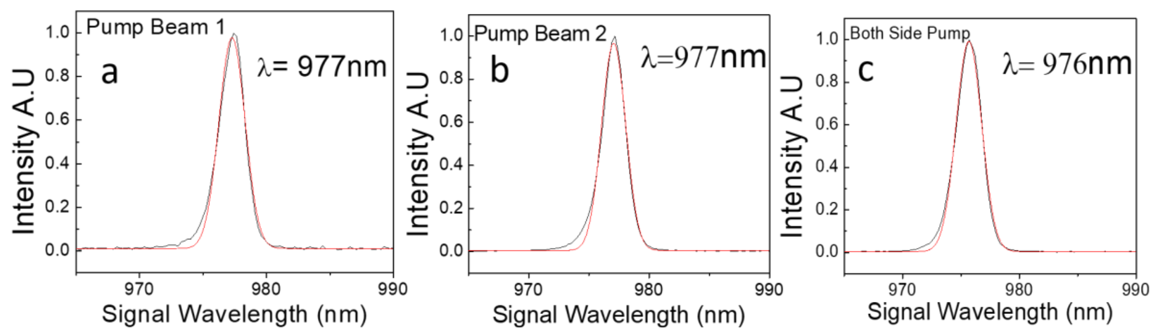

Figure 6.3. Signal spectrum, (a) for pump beam 1, (b) for pump beam 2, (c) for both pump beams

beams [103]. The threshold of the DRO for Gaussian pumping in the absence of SPP was measured to be ~75 mW for each pump beam in either direction. However, in the presence of both pump beams, the DRO threshold decreased to ~40 mW, clearly confirming coherent coupling between the generated signal pulses. It also confirms the temporal and spatial overlap of the resonating signal beams of both pumps, as required for vector-vortex generation. As expected [72], the DRO threshold for vortex pump beams, PB1 and PB2, separately, was measured to be ~290 mW, higher than that for the Gaussian-beam-pumped DRO. While a similar threshold reduction due to coherent coupling is also observed for vortex pumping, the signal beam loses its vorticity as the signal pulses generated from PB1 and PB2 are of opposite helicities. However, for the vector-vortex generation, we inserted QWPs inside the cavity, while pumping the DRO from both sides with an average power of 300 mW in each beam. Both QWPs (QWP1 and QWP2) had optic axis rotated by +45° with respect to the horizontal axis. We analyzed the outcoupled signal from the mirror, M3, using a detection unit comprising the combination of QWP, $\lambda/2$ plate, and a PBS [94]. We projected the signal vector-vortex beam of OAM mode, l=1, in different polarization states, horizontal (H), vertical (V), diagonal (D), anti-diagonal (A), right circular (R), and left circular (L), on the Poincaré sphere, by adjusting the optic axis of the QWP and $\lambda/2$ plate. The results are shown in Figure 6.4. As evident from Figure 6.4, the projection of the signal beam to R and L polarization states results in vortex intensity profile with OAM order, $l = 1$ and $l = -1$, respectively. However, the projection on H, V, A and D polarization states result in the superposition of two opposite helical wave fronts of vortex order, $|l| = 1$, generating a ring lattice structure containing two-lobe ($2l$) pattern at different orientations. All these projected intensity distributions represent different points on the Poincaré sphere. The rotation of the two-lobe pattern obtained with the rotation of the optic axis of the QWP and $\lambda/2$ plate for polarization measurement determines the spatial distribution pattern of the vector-vortex beam and verifies the non-separability. The inset of Figure 6.4 shows the intensity profiles of the pump and idler beams without any polarization projection. As in previous reports [15,104], one can measure the purity of the OAM mode of the vector vortex beam through the mode projection technique [105]. However, due to a lack of suitable spatial light modulator (SLM) in our laboratory, we were not able to perform the mode purity measurement for the vector vortex beams. On the other hand, since the OAM beam of the OPO is generated through the OAM conservation in nonlinear process, we expect the generated beam to carry the pure OAM mode of the pump. Additionally, the polarization projection and beam quality measurements are performed in the far field region to reduce the effect of higher order cavity modes (if any) in the resonant beams.

Confirming the generation of the vector-vortex beam from the OPO at 977 nm, we further studied the performance of the device across the tuning range. Pumping the OPO from both sides, we changed the crystal temperature to vary the signal and idler wavelengths. Although

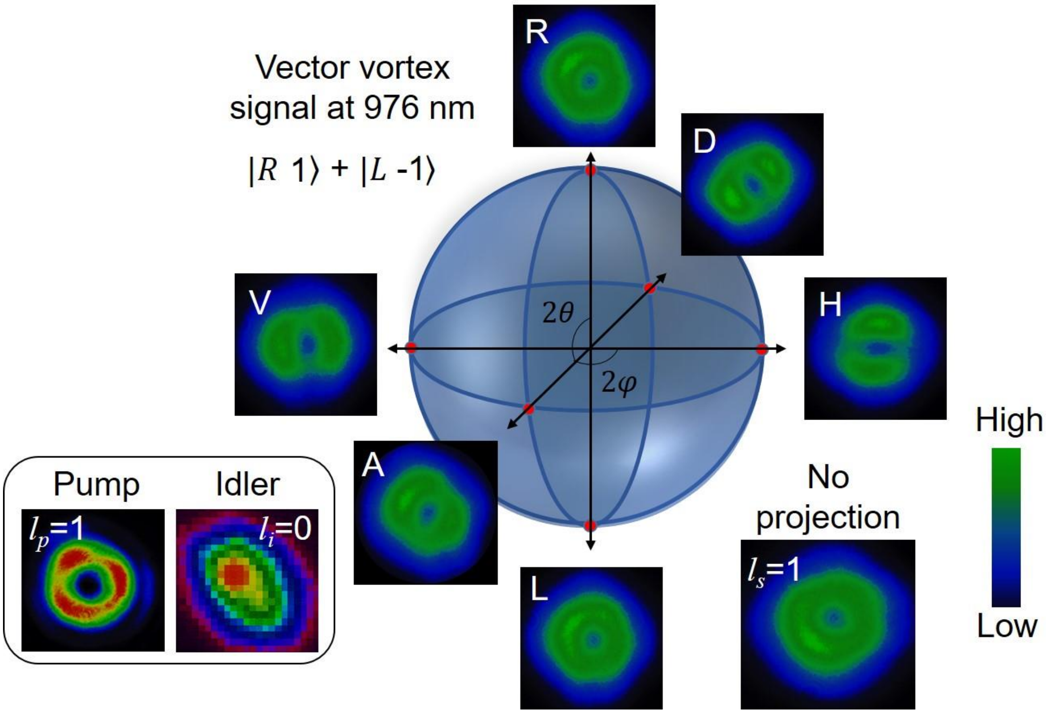

Figure 6.4. Intensity profiles of the signal vector-vortex beam of OAM mode, ls = 1. Depending on the projection of the beam in different polarization states, R, A, L, D, H and V (as shown by the white letters on the images) on the Poincaré sphere, the mode pattern of the beam recorded by the CCD camera change at different points on higher-order Poincaré (LG-Bloch) sphere for $1/\sqrt{2}$ (| R, 1⟩ + e−iφ |L,−1⟩). Inset images are intensity distribution of one of the pumps, idler and the signal beams

the current OPO can be tuned across 850-1420 nm [103], the cavity mirrors limit the operation to 950-1200 nm. On the other hand, the retardance of the intra-cavity QWPs is the limiting factor for the wavelength tunability of the vector-vortex output. Since the zeroth-order QWPs used in the current study have retardance varying from 0.2523 (0.20) to 0.2447 (0.208) with the signal (idler) wavelength variation from 960 nm (1193 nm) to 990 nm (1149 nm), the tuning is confined to this wavelength range. Such a small change of retardance with wavelength maintains linear polarization of the resonating signal beam in region A (see Fig. 1a) of the OPO without introducing significant losses due to polarization rotation. However, the inappropriate retardance of the QWP changes the linear polarization into elliptic, severely effecting the phase-matching condition. One can, in principle, use achromatic QWPs having constant retardance over a wider range of wavelengths to increase the tunability of the vector vortex beam. However, we did not have the availability of such achromatic QWP to extend the wavelength range of the current vector vortex OPO. We studied the non-separability of the signal beam at two different wavelengths, 964 nm and 990 nm, across the tuning range. To confirm the vector-vortex nature of the signal pulses in this range, we again performed projective measurements by using a QWP and PBS, and projected the generated state in different polarization basis, with the results shown in Figure 6.5. As evident from Figure 6.5(a) and 5.5(b), the rotation of the QWP for polarization measurement rotates the spatial intensity distribution of signal beams at 964 nm and 990 nm, thus verifying the non-separability and vector-vortex nature of the signal beam across the tuning range of 964-990 nm. Due to the high reflectivity of the cavity mirrors, we measured an outcoupled vector-vortex beam power of >5 mW in 4.4 ns pulses of 0.25 µJ energy across the tuning range. However, with the optimization

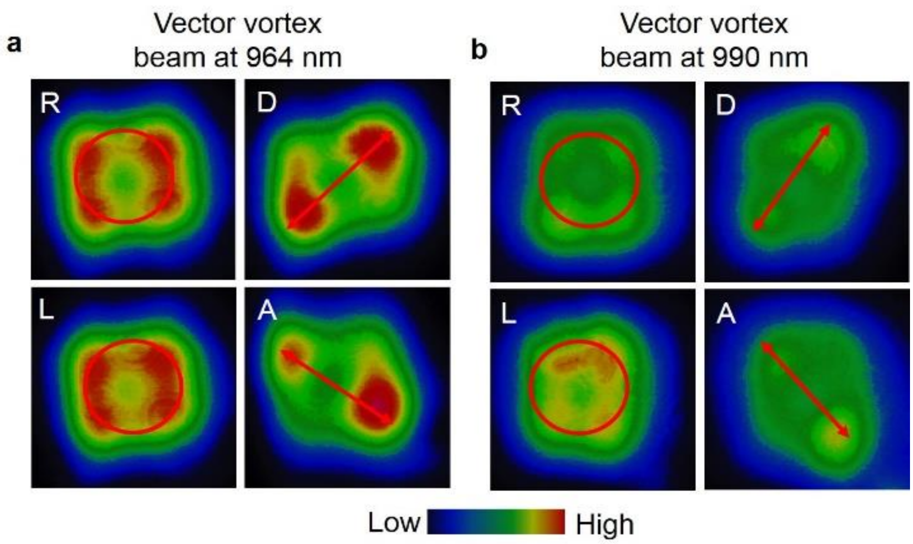

Figure 6.5. Vector-vortex beam at two different wavelengths, 964 and 990 nm, across the tuning range of the OPO. Intensity distribution of the vector-vortex beams for the projective measurement in polarization states, R, L, D, and A for the vector-vortex beams at (a) 964 nm and (b) 990 nm. The projective measurement in A and D basis results 2l petals.

of output coupling, a substantial enhancement in vector-vortex beam power are expected, enabling practical applications certainly at the cost of increase of operation threshold of the OPO.

6.4 Conclusion

In conclusion, we have demonstrated an experimental scheme to generate vector-vortex beam directly from an OPO in DRO configuration, pumped by vortex beams from both sides of the cavity. By manipulating the polarization of the resonant wave using a pair of intra-cavity QPWs, we have generated vector-vortex beam tunable across 964-990 nm. Wavelength tunability of the source is limited by the uniform retardance range of the QWPs. Further increase in the tunability of the vector-vortex beam can be achieved by using broadband achromatic zero-order QWP. The generic approach can also be used in cw and ultrafast OPOs and extended to other wavelength regions across the optical spectrum.

Chapter 7 Multi-structured beam optical parametric oscillator

This chapter constitutes following publication

1) **Varun Sharma**, S. C. Kumar, G. K. Samanta, and M. Ebrahim-Zadeh, "Tunable multi-structured-beam optical parametric oscillator," in Frontiers in Optics + Laser Science APS/DLS, The Optical Society (Optical Society of America, 2019), paper JW3A.41.in Optics + Laser Science APS/DLS, The Optical Society (Optical Society of America, 2019), paper JW3A.41 and manuscript under preparation for journal submission.

7.1 Introduction

In the previous chapters, we discussed different techniques for the generation of optical vortices and vector beams in a wide spectral range, starting from mid-IR to UV. As discussed before, beams with OAM and varying polarization across the beam showed applications in quantum information [9,94], microscopy [16,85], and material processing [11,17]. Spatial structures discussed until now have common limitations of diffraction with propagation and does not self-heal after obstruction in the path. On the other hand, the Airy beam shows all these emerging properties of non-divergence, self-healing and propagate in a parabolic path. These peculiar properties utilized in curved plasma guiding [23], light-sheet microscopy [22] and micro-particle manipulation [106]. While the Airy beam and optical vortices demonstrated various applications, the conventional method of generating all these different spatial structures based on SLM or different phase elements (SPPs and CPM) does not work for a simultaneous generation. The simultaneous generation of all these spatial structures from a single source is not very efficient, and we often need to rely on different techniques for the generation of different spatial structures, as demonstrated in [13,21,99]. This chapter focus on a new method for generating multiple spatial structures over a broad range of wavelength from a single source.

Vortex pumping in OPOs has been used to control the transfer of pump vortex content between signal and idler [48,49] and for the generation of high power optical vortices up to mid-IR spectral region [50,72]. Similarly, the technique of intracavity cubic phase mask enables the generation of coherent two-dimensional Airy beam from a laser and OPO [107,108]. Still, to generate each structured beam from an OPO, it requires a separate cavity setup with different phase elements. In this work, we demonstrated the simultaneous, direct generation of multi-spatial structure beams from a singly resonant ultrafast OPO cavity. With the help of higher-order vortex pumping and controlled exchange of OAM between signal and idler, we have generated vortex-Airy beam, vortex beam with OAM order of 1 in the signal, and vortex beam of order 1 in idler. In the same cavity setup by controlling the OAM transfer between signal and idler with the help of intracavity aperture, we have transferred pump OAM to the non-resonant idler and generated signal beam with the spatial structure in Airy beam, Gaussian beam, and idler in vortex profile of order 2. These all mentioned spatial structures are tunable across 1457 – 1680 nm in signal wavelength and 2901-3944 nm in idler wavelength. At the same time, each set of spatial structures generated from a separate output port in OPO, which enables their simultaneous use for various applications at the same time.

7.1 Experimental scheme

The schematic of the experimental setup to generate multi spatial structured beams is shown in Figure 7.1. A Yb fiber laser centered at 1064 nm with a spectral width of 1.4 nm producing output pulse width of 20 ps at a repetition rate of 80 MHz in Gaussian spatial intensity profile (M^2<1.1) is used as the pump source. For the best performance of the laser, we operated the laser at its maximum output power of 14 W and subsequently controlled the laser power to the experiment with the help of a half-wave plate (λ/2) and a polarizing beam splitter cube (PBS). The spiral phase plate (SPP) of phase winding corresponding to vortex order, *l*=2 is used to convert the Gaussian pump beam into an optical vortex. Further, a second λ/2 plate controls the input pump beam polarization for phase matching inside the nonlinear crystal. The input pump beam is focused at the center of the nonlinear crystal using a plano-convex lens, L1, of focal length *f*=150 mm which results in the beam waist radius of 40 µm while used Gaussian pump beam. A 50 mm long and 8x1 mm^2 in aperture multi-grating MgO doped periodically poled lithium niobate (MgO:PPLN) crystal with the grating period varying from 29.05 µm to 31.5 µm is used as the nonlinear crystal for OPO. To control the wavelength tunability of the

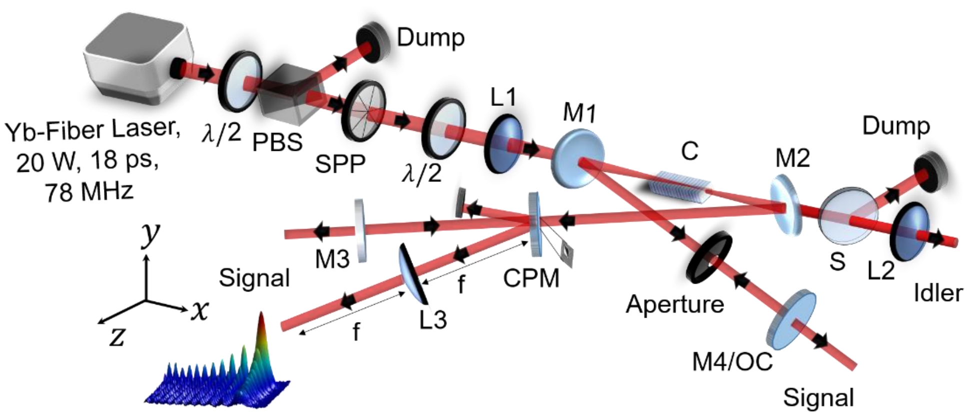

Figure 7.1. Schematic of the experimental setup. λ/2, half-wave plate; PBS, polarizing beam splitter cube; L1-3, plano-convex lenses of different focal lengths; SPP: spiral phase plate, M1-4: OPO mirrors; OC, output coupler; C, PPLN crystal; CPM, cubic phase mask.

OPO, the crystal is housed in a temperature oven allowing the crystal temperature variation up to 200°C with stability of ±0.1°C. The OPO is configured in a singly resonant four mirror standing wave X-cavity configuration with two curved mirrors, M1 and M2, of a radius of curvature of 150 mm and two plane mirrors, M3 and M4. The mirrors, M1, M2 and M3 have high reflection (>99%) for the signal wavelength across 1400-2100 nm and high transmission for the idler wavelength across 2100-4400 nm and pump wavelength at 1064 nm. To extract the resonating signal power, we have used mirror M4 with a transmission of 5% for signal the wavelengths across 1400-1600 nm. To record and study the idler beam profile we used a CaF2 lens of focal length *f*=150 mm after extracting the beam from the undepleted pump and leakage signal power using the wavelength separator, S. For the Airy beam generation, we have used a cubic phase mask (CPM) in the form of a binary diffraction grating . The CPM is optimized to have 5% diffraction efficiency in first diffraction orders. The CPM produces cubic phase-modulated beam which subsequently Fourier transformed into an Airy beam using a lens, L3, of focal length, *f*=300 mm. However, to control the spatial mode of the resonating beam, an aperture is used before the mirror M4. The OPO cavity is synchronized with the second harmonic of the pump repetition rate. The total physical cavity length of the OPO is 981 mm.

7.2 Results and discussion

For the implementation of the current scheme from OPO, we used the method of higher-order vortex pumping in the singly resonant OPO. In the process of down-conversion inside an OPO, the overlap integral $\Lambda_{p,s,i}$ between spatial modes of pump, signal, idler, and the loss parameter for the cavity modes decides the spatial modes of generated signal and idler [49]. With the vortex pumping with pump OAM $l_p = 2$, there are three different possible combinations of signal and idler modes conditioned to the OAM conservation. Out of these possibilities, allowed combination $\Lambda_{p=2,s=1,i=1}$ inside the OPO, with signal and idler OAM content $l_s = l_i = 1$ have maximum value of 0.7. Similarly, for the same vortex pumping order overlap integral $\Lambda_{p=2,s=2,i=0}$ or $\Lambda_{p=2,s=0,i=2}$ has a value of 0.5, which corresponds to signal in vortex beam profile of order 2 and idler in Gaussian beam profile and vice versa. With these conditions, cavity loss also plays a crucial role in switching the OAM modes between signal and idler [50]. For the simultaneous generation of multiple spatial structures in the signal, the choice of resonating signal mode plays a crucial role. Firstly, with the vortex pump $l_p = 2$, we utilized $\Lambda_{p=2,s=0,i=2}$ combination with signal in Gaussian intensity distribution and idler in vortex beam with OAM $l_i = 2$. For this OPO operation, we kept PPLN crystal at 110°C with the grating period (Λ) of 30.3 μm. For this grating period and temperature, signal wavelength corresponds to 1552 nm and corresponding idler at 3380 nm. For mode selection of signal inside the cavity, we further used the method of an intracavity aperture to restrict any higher-order mode oscillation inside the cavity and restricted the signal to oscillate in Gaussian mode. To confirm the spatial mode of resonating signal and idler, we used a pyrocam based camera with a pixel area of 85x85 μm^2 while the pump beam is imaged on a CCD based camera with pixel area of 4.4x4.4 μm^2. Pump beam coming through SPP resulted in a doughnut shape profile, as shown in Figure 7.2(a). For topological charge measurement in the pump beam, we used the tilted lens scheme [74], and counted the characteristic lobes at the Fourier plane of the lens. As shown in Figure 7.2(b), the pump beam splits into 3 characteristic lobes at the Fourier plane after passing through a tilted lens of focal length of 400 mm. We observed successful OPO operation at a pump power of 1.5 W for the second harmonic cavity configuration and pump beam with $l_p = 2$. After this, we have studied idler beam profile by using CaF2 based collimating lens L3, of focal length 150 mm and wavelength separator S1 for extracting idler from undepleted pump beam. By using a pyrocam based camera, we recorded the idler in far field, and observed doughnut shaped beam profile as shown in Figure 7.2(c). After confirming the idler beam profile, we used tilted lens measurement to confirm the OAM content in the idler beam. For the tilted lens measurement, we used another lens L4 of focal length 750 mm, after the collimating lens L3. We have recorded the idler beam profile at the Fourier plane of tilted lens L4 and calculated the number of lobes present in the idler beam as shown in Figure 7.2(d). Presence of 3 characteristic lobes at the Fourier plane confirms that idler OAM content, $l_i = 2$, same as that of the pump beam. After this, we have recorded the spatial structure of the signal beam coming from the output coupler M3 as shown in Figure 7.2(e). It is evident from Figure 7.2(e), the signal is resonating in the Gaussian beam profile, and OAM conservation satisfies for this OPO configuration. For the simultaneous generation of the Airy beam in the signal spectrum, we introduced a cubic phase mask (CPM) before mirror M4 in the OPO cavity. This CPM is in the form of a binary diffraction grating, which can be represented by equation (7.2.1). This binary grating modulates the phase as well as the amplitude of the input pump beam. For resonating signal in the Gaussian beam profile, this cubic phase mask introduces a cubic phase to the signal beam in x & y direction and results in a two-dimensional cubic phase pattern. To convert the cubic phase into the Airy beam, we used another Fourier lens, L2, of focal length 150 mm outside the OPO cavity. We recorded the beam profile of the signal beam after Fourier length on pyrocam, as shown in Figure 7.2(f), and confirmed the Airy profile in the signal beam. To simplify the study of Airy beam properties such as acceleration, non-diffraction, and self-healing, we fixed the cubic phase mask in such a way that the central lobe always accelerates along the y-axis as shown in Figure 7.2(f).

$$h(x,y)=\frac{1}{2}h_0\left[\operatorname{sgn}\left\{\cos\left(2\pi x\frac{N}{l}+\left(\frac{x}{w_o}\right)^3+\left(\frac{y}{w_o}\right)^3\right)\right\}+1\right] \quad \textbf{(7.2.1)}$$

After the successful generation of Gaussian and Airy beam in signal and optical vortices in the idler spectrum, we have investigated the Airy properties of acceleration, non-diffracting, and self-healing in the signal beam. For measuring acceleration in the Airy beam, we recorded the Airy beam profile after the Fourier plane of the lens in a regular spatial interval of 10 cm for a distance of 1.4 m. We used a pair of mirrors after the Fourier lens to align the Airy beam along

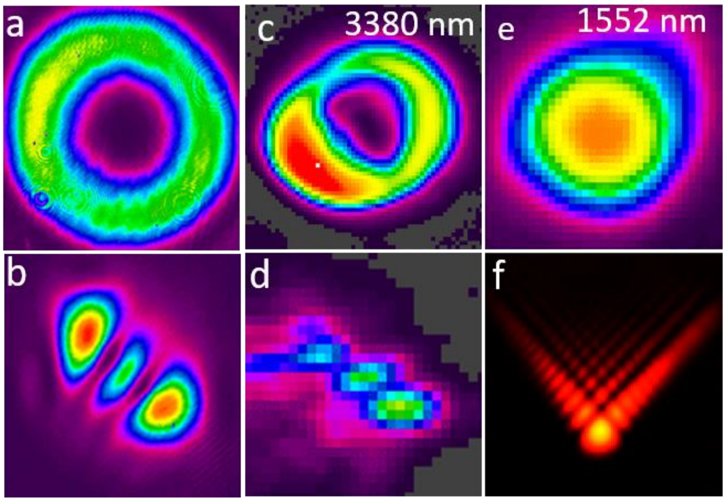

Figure 7.2. (a,b) Signal beam profile and tilted lens measurement, (c,d) idler beam profile and tilted lens measurement, (e) signal in Gaussian beam profile, (f) signal in Airy beam profile

the length of the optical table. By taking snapshots of the Airy signal profile along the propagation direction, we recorded a variation of 1.02 mm in the central lobe position from the rectilinear path. To find the launching angle and y_0 parameter we have fitted the shift in the central lobe of the Airy beam along the propagation direction with quadratic function as shown in Figure 7.3(a). After plotting the curve (with correlation coefficient of fitting r^2= 0.99), we calculated the launching angle of 1 mrad and parameter y_0 = 484 µm. We also measured the non-divergence property of the Airy beam with propagation. For this, we plotted the spatial beam profile with Airy function and calculated the width of the central lobe along the propagation direction. With the propagation of 1 m, we recorded a variation of FWHM of central lobe from 0.644 mm to 0.709 mm along beam direction, as shown in Figure 7.3(b). We recorded the variation of 65 µm in the central lobe size, which is lower than our pixel size of 85 µm of the camera and confirmed the non-diffraction property of the Airy beam for a propagation distance of 1 m. We have tested the self-healing property of the Airy beam. For

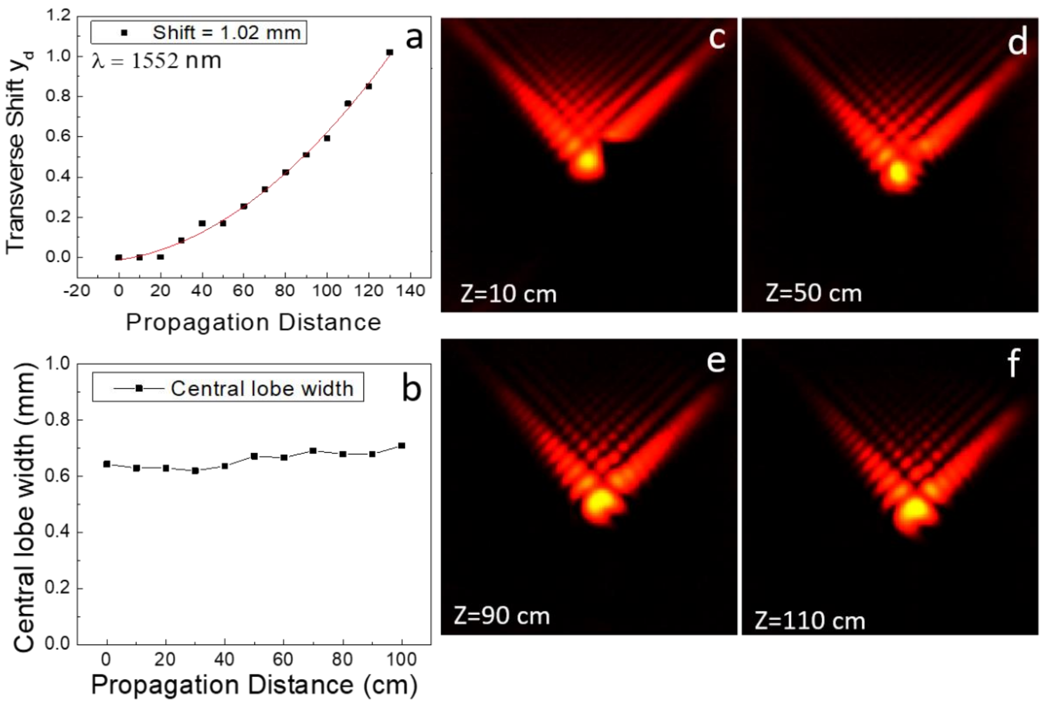

Figure 7.3. Airy properties, (a) acceleration of Airy beam, (b) non-divergence property, (c-f) self healing property

this study, we used a knife-edge to remove the first side lobe from the Airy beam, as shown in Figure 7.3(c), and propagated it for 1.1 m. We recorded the spatial beam profile of the Airy beam profile along the propagation direction at 10, 50, 90 and 110 cm as shown in Figure 7.3(c-f). We started observing side lobe appearance along the propagation direction with complete healing of the Airy beam after the propagation distance of 90 cm, as shown in Figure 7.3(e). This mode selection and successful demonstration of the Airy beam properties confirmed the signal in the Gaussian and Airy beam profile and idler in vortex beam with OAM $l_i = 2$.

Further, we utilized the mechanism of pump OAM content sharing between signal and idler [50] to generate another spatial pattern in the signal and idler from the same OPO configuration. By removing the intracavity aperture and allowing higher-order modes in the signal, we aimed for pump OAM transfer between signal and idler with the same topological charge. For OPO operation, we kept the temperature of PPLN crystal at 115°C with grating period to 29.3 µm. At this grating period, the signal, correspond to 1482 nm and idler at 3772 nm, and recorded the OPO operation threshold of 800 mW, which is lower as compared to Gaussian mode oscillation inside the cavity. Threshold variation can be understood, as overlap integral $\Lambda_{p=2,s=1,i=1}$ for the signal and idler OAM of order 1 is 0.7, which is higher as compared to $\Lambda_{p=2,s=0,i=2}$ combination. This signifies a better overlap and energy exchange for $\Lambda_{p=2,s=1,i=1}$ combination and results in a lower threshold of OPO to work. To confirm and study OAM exchange between signal and idler for pump vortex order $l_p = 2$, we recorded signal and idler beam profile at far-field. We recorded doughnut shape in the signal beam after output coupler M3 is shown in Figure 7.4(a). We confirmed signal is carrying OAM $l_s = 1$, by using tilted lens measurement and counting the number of lobes present at the Fourier plane, as shown in Figure 7.4(b). Similarly, we have imaged idler on the pyrocam and recorded doughnut beam profile with OAM $l_i = 1$ as shown in Figure 7.4(e,f). This mode selection of signal resulted in the intracavity beam with a helical wavefront and provided a gateway to generate vortex-Airy beam from the OPO. To generate vortex-Airy beam, from OPO, we used the method of passing a beam with a helical phase from the cubic phase modulator [109]. Beam with such phase variation, modulates its phase after passing through CPM and results in a beam with cubic phase containing phase singularity imprint, as shown in equation 7.2.2.

$$u(x,y,z=0)=Ai(x/x_0)Ai(y/y_0)\exp\left[a\left(\frac{x}{x_0}+y/y_0\right)\right](x+iy)\ (3) \qquad \textbf{(7.2.2)}$$

From equation (7.2.2), it is clear that the resultant beam has a phase singularity at the central lobe of 2-dimensional cubic phase pattern. Since the signal is oscillating in vortex mode with OAM $l_s = 1$, the output beam in the first-order diffraction from CPM will result in a beam with phase profile, as shown in the equation (7.2.2). To convert the cubic phase with a phase singularity into a vortex-Airy beam, we used a Fourier lens of 150 mm, as shown in Figure 7.4(c,d). To confirm the phase singularity and OAM content in the vortex-Airy beam, we used Mach-Zehnder based self-interferometric technique. Due to the smaller size of vortex Airy lobes as compared to the pixel size of the camera, we were not able to resolve interference

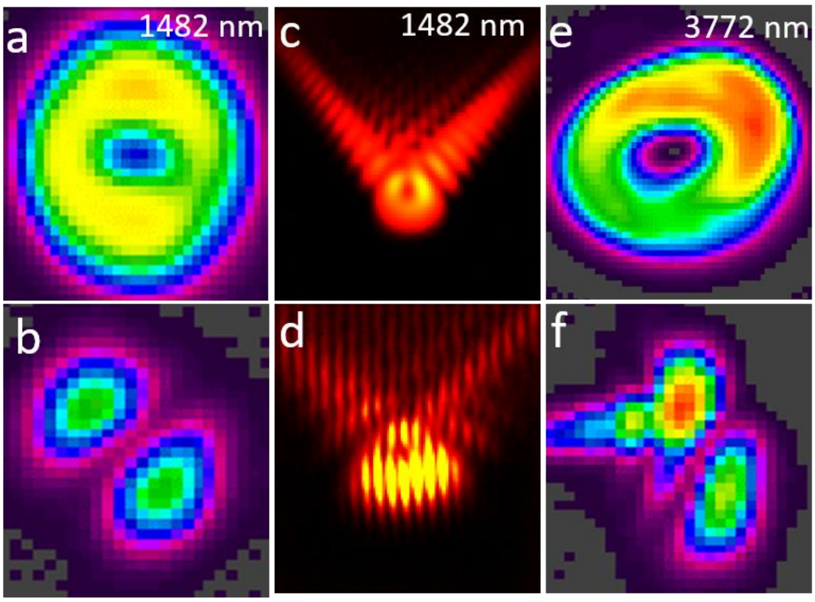

Figure 7.4. (a,b) Signal beam profile and corresponding tilted lens measurement, (c) vortex-Airy profile, (d) self-interference fringes of vortex-Airy beams, (e,f) idler beam profile and corresponding tilted lens measurment

fringes of the Airy beam with itself. To avoid this ambiguity in the phase information, we passed the cubic phase coming out of the CPM through Mach-Zehnder interferometer and recorded interference fringes. In the interference fringes, as shown in Figure 7.4(d), we observed a pair of fork pattern aligned in the opposite direction to each other, which is a confirmation of optical vortex of order 1. Interferometric fringes confirmed that vortex-Airy beam carries the same vortex charge of $l_a = 1$ as that of the input signal beam. After confirmation of OAM content in signal, idler, and vortex-Airy beam, we investigated the properties of vortex-Airy beam. Firstly, to find out the acceleration in the beam, after the

Fourier plane, we propagated the output beam up to 1.2 m and recorded the vortex-Airy beam profile. We recorded the beam profile in a regular spatial interval of 10 cm after the Fourier plane and observed the pixel position of the dark core area in the central lobe. After propagating the vortex-Airy beam up to 1.2 m, we found a transverse shift of 1 mm in the central lobe along the y-axis from the rectilinear path, as shown in Figure 7.5(a). Plotting the change in the central lobe dark core area along the transverse direction with propagation, we used a quadratic function fitting for matching the experimental results. We calculated the launching angle of 4 mrad and y_0 of 586 μm. These parameters fit with the recorded vortex Airy beam profile and further confirms the parabolic trajectory of the vortex-Airy beam. To study the non-diffraction properties of the vortex-Airy beam, we have plotted the x-axis line profile of vortex distribution in the Airy beam and measured the separation between intensity maxima of the line profile. After propagating the beam up to 90 cm, we recorded fluctuation in the FWHM of the recorded line profile from 680 μm to 725 μm, as shown in Figure 7.5(b). Variation in vortex-Airy radius is 45 μm which is less than the pixel size of pyrocam and confirms the non divergence properties of vortex-Airy beam upto propagation distance of 90 cm. To observe the property

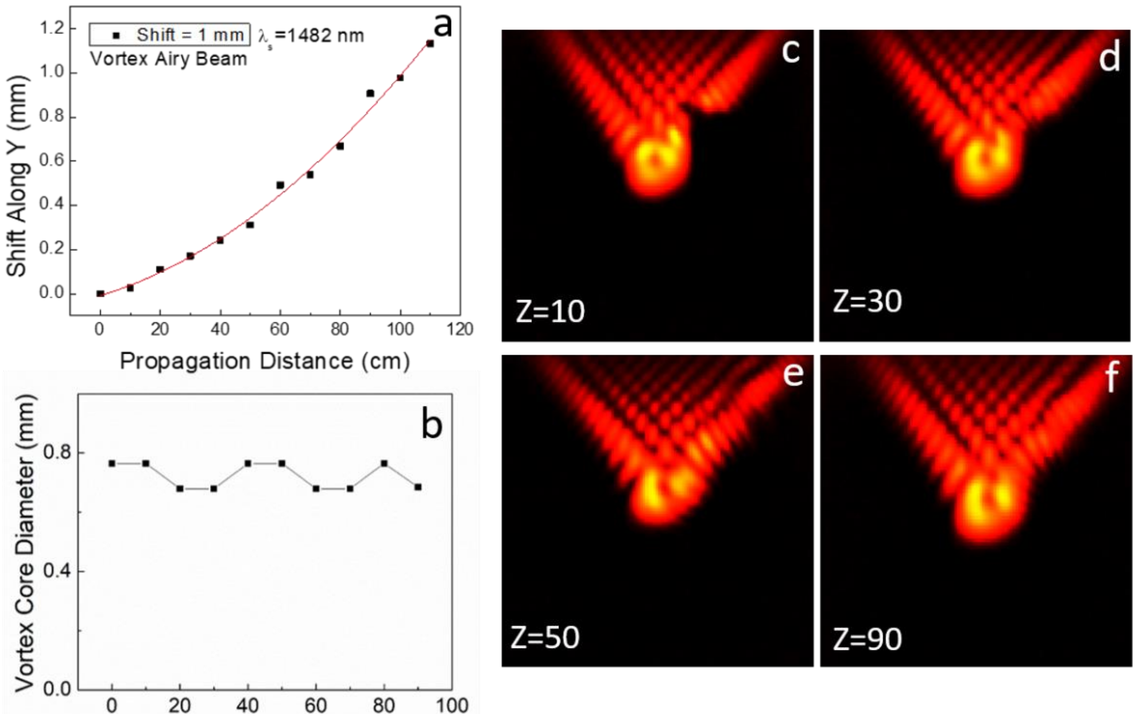

Figure 7.5. (a): vortex-Airy beam acceleration up to 1.2 m, (b) non-diffraction measurement of vortex beam profile, (c-f) self-healing of vortex-Airy beam .

of self-healing in vortex-Airy beam, we removed first side lobe of the beam by using a knife edge as shown in Figure 7.5(c). The vortex-Airy beam was then propagated along the rectilinear path and the beam profile recorded at z=10, 30, 50 & 90 cm. After taking the beam profile along this propagation direction, we have observed complete healing of the first side with propagation up to 90 cm.

After the successful simultaneous generation of these multiple spatial structure beam in signal and optical vortices in idler, we extended their generation over a broad range of wavelength by tuning the OPO. For OPO tunability, we varied the temperature from 50-200°C for temperature tuning across different grating periods from 29.05 μm to 31.5 μm of PPLN. By implementing the intracavity aperture for the signal oscillation in Gaussian mode, which results in addition to Gaussian intensity distribution, Airy beam in signal, and corresponding vortex of order l_i =

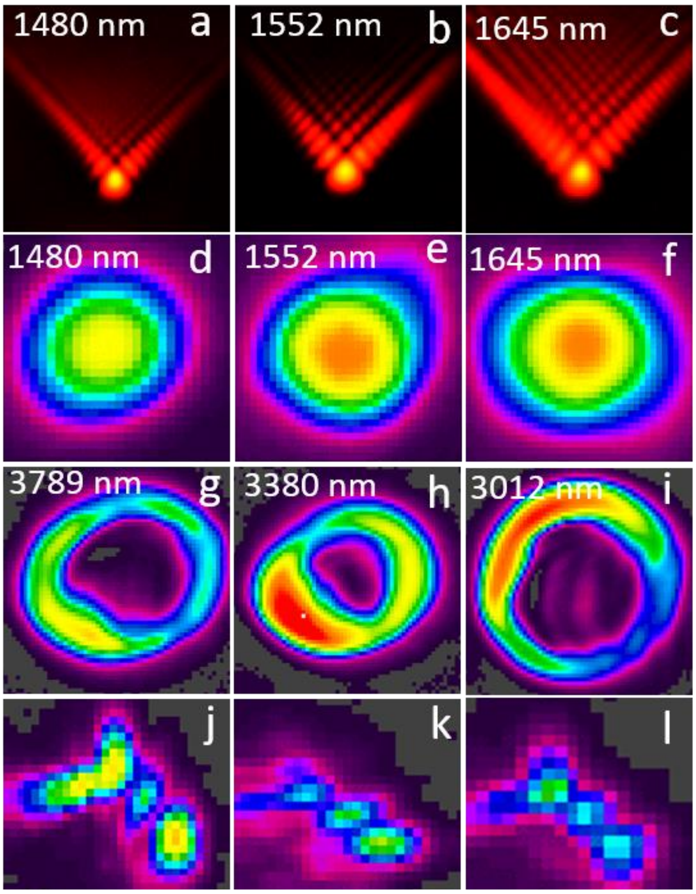

Figure 7.6. Beam profile across the tuning range, (a-c) signal in Airy beam profile, (d-f) signal in Gaussian intensity profile, (g-l) idler vortex beam profile and corresponding tilted lens measurements.

2 in idler. For this configuration, we tuned OPO from 1457 nm to 1680 nm in signal wavelength and 2901 nm to 3944 nm in the corresponding idler region. We recorded the spatial beam profile of signal beam across the tuning range in Airy and Gaussian intensity distribution, as shown in Figure 7.6(a-f) and idler in vortex beam profile with tilted lens measurements as shown in figure 7.6(g-l). For all beam profile measurements, we have used pyrocam and recorded the far-field pattern in both signal and idler as shown in Figure 7.6(a-l). Asymmetry in the idler vortex beam profile across the tuning range can be attributed to the astigmatism due to the curved mirror in the cavity and asymmetry in the interacting beams. After confirming the tunable generation of these spatial structures for Gaussian resonating signal mode, we have removed the intracavity aperture and studied the tunability characteristics for signal in vortex resonating mode. For this cavity configuration, we again tuned cavity from 1457 nm to 1680 nm in signal and 2901 nm to 3944 nm in idler. Across this tuning range, we recorded the signal in the vortex and vortex-Airy profile with OAM content $l_s = 1$ (tilted lens measurements) as shown in Figure 7.7(a-f) and idler in vortex beam profile with OAM content $l_i = 1$ (tilted lens measurements) as shown in Figure 7.7(j-o).

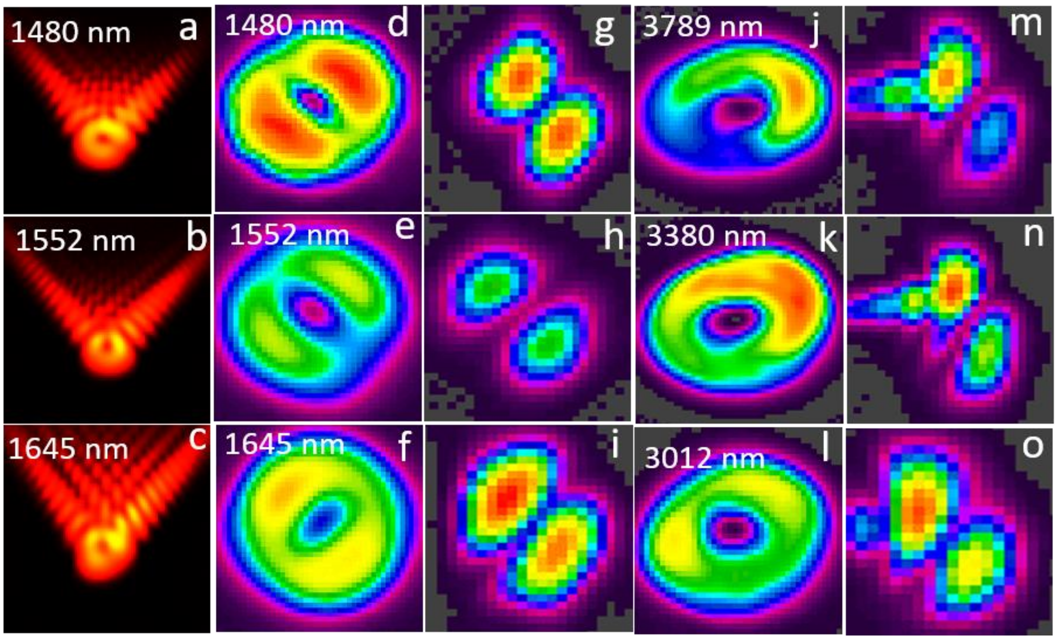

Figure 7.7. Beam profile across tuning range, (a-c) signal in vortex-Airy profile, (d-f) signal in vortex beam profile and corresponding tilted lens measurements, (j-o) idler in vortex beam profile and corresponding tilted lens measurements

Across the tuning range for Gaussian resonating mode, we studied output power variation across the tuning range at a constant pump power of 8 W. For vortex idler beam with, $l_i = 2$, we recorded power variation from 435 mW to 1.059 W. For signal in Gaussian intensity profile we recorded power variation from 340 mW to 1.275 W and for signal in Airy distribution, we recorded power variation from 162 mW to 132 mW as shown in Figure 7.8(a). After studying the power across the tuning range, we studied the power scaling for the same cavity configuration at signal $\lambda_s = 1482$ nm in Gaussian and Airy profile and idler $\lambda_i = 3772$ nm in the vortex beam profile of order 2 by increasing the pump power up to 10 W. We generated idler in vortex beam profile with vortex order 2 with maximum output power of 803 mW. For signal output power coming out of output coupler, we recorded a maximum output power of 547 mW and signal in Airy beam profile with a maximum output power of 238 mW as shown in Figure 7.8(b).

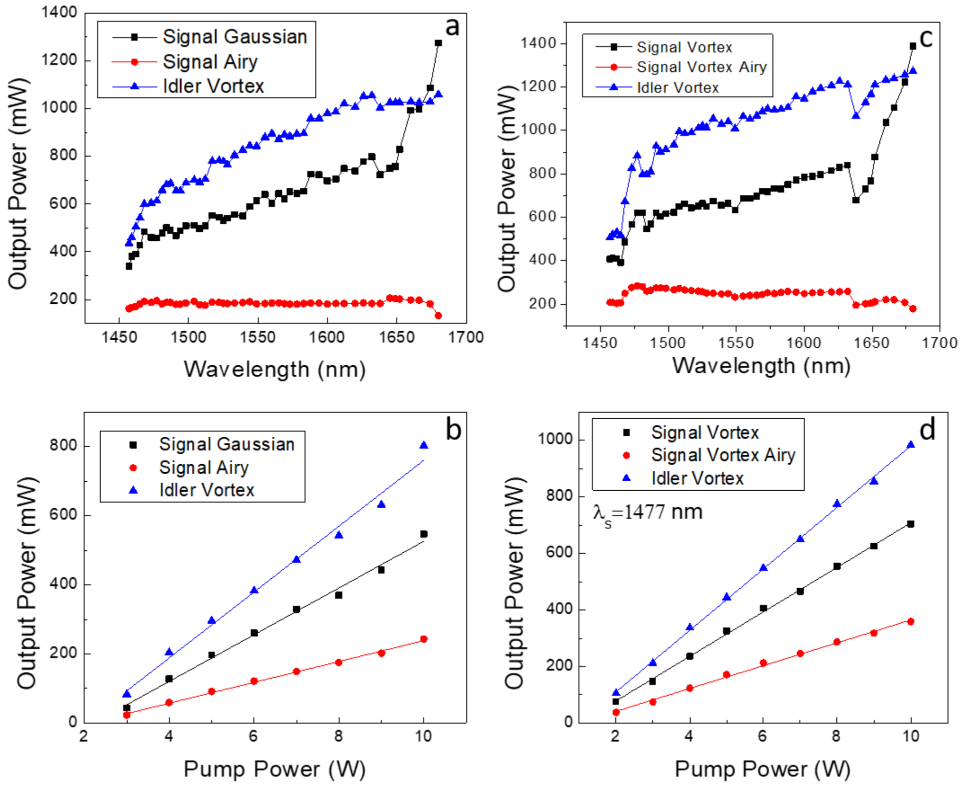

Figure 7.8. Output power characteristics of the OPO, (a,b) tunability and power scaling for Gaussian resonating mode, (c,d) tunability and power scaling for vortex resonating mode

After this, we studied the power across the tuning range for resonating signal in vortex mode and recorded idler output power variation from 506 mW to 1.273 W, in the vortex of order l_i = 1. For the signal in vortex beam profile with l_s = 1, we recorded power variation from 406 mW to 1.388 W, and for signal in vortex Airy profile with l_s = 1, we recorded power variation from 208 mW to 179 mW was recorded as shown in Figure 7.8(c). After this, we studied the power scaling performance for this cavity configuration with l_i = l_s = 1, at λ_s = 1482 nm, and the corresponding idler at λ_i = 3772 nm for a maximum input pump power of 10 W as shown in Figure 7.8(d). For the idler beam, we recorded the maximum output power of 980 mW at the pump power of 10 W with a slope conversion efficiency of 10%. For signal in vortex beam profile, we recorded maximum output power of 704 mW at maximum pump power with a slope conversion efficiency of 7.8% and for the vortex-Airy beam at 1482 nm, we have recorded maximum output power of 364 mW with a slope conversion efficiency of 4%. This increased output power in the spatial-structure corresponding to vortex mode oscillation configuration beams as compared to Gaussian mode configuration is attributed to the better overlap integral between the pump, signal and idler beam.

For ultrafast characteristics of the OPO, we have measured the spectrum and pulse width of the generated signal in the Gaussian intensity profile as shown in Figure 7.9(a,b). To measure the pulse width, we used intensity auto-correlation method and measured the pulse width of the

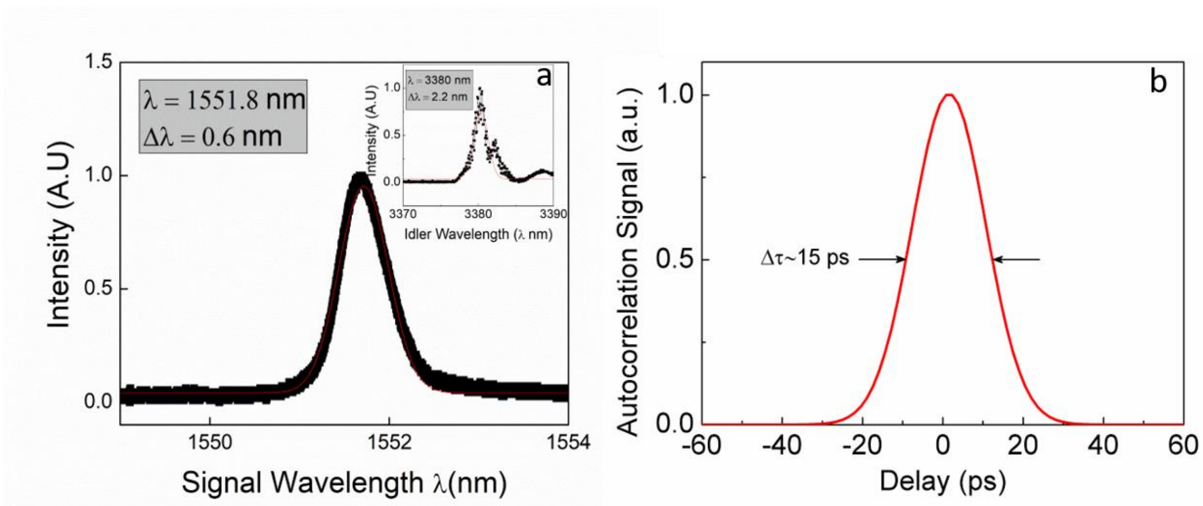

Figure 7.9. Spectral and temporal characterstics in Gaussian intensity distribution, (a) signal and idler wavelength, (b) autocorrelation for signal

output signal at 15 ps at a repetition rate of 160 MHz and the corresponding spectrum was centered at 1551 nm with 0.6 nm of spectral width with bandwidth product $\Delta\tau\Delta\upsilon$ of 1.12 well above the transform limited pulse.

7.3 Conclusion

In conclusion, we demonstrated the simultaneous generation of multiple structured beams from an ultrafast singly resonant OPO in the mid-IR spectral region. By exploiting the OAM transfer between signal and idler with the intracavity aperture as a controlling unit, we generated these multi-structures in Gaussian, vortex, Airy and vortex-Airy intensity distribution. In the case of pump vortex transfer to the idler, we have generated the signal in Gaussian and Airy distribution while idler has vortex distribution with $l_i = 2$ with maximum output power as high as 1W. For the pump vortex sharing between signal and idler, generated signal with, $l_s = 1$ in vortex beam profile and vortex-Airy profile while idler is in vortex beam profile with vortex order $l_i = 1$ with output power as high as 1.2 W. This scheme successfully demonstrated the tunability of all these structures from 1457 nm to 1680 nm in signal and 2901 to 3944 nm in idler. This scheme provides all these spatial structures from the different output ports of the cavity and can be utilized simultaneously for various applications.

Chapter 8 Summary and future scope

8.1 Summary

This thesis is primarily focused on the study of optical parametric oscillators and using them to generate different spatial structures. We presented new methods to generate spatial structures, either by using the Gaussian beam as a primary pump source or by manipulating the Gaussian pump beam into optical vortices. We presented the generation of Gaussian beams, optical vortices, vector vortex, Airy beam, and vortex-Airy beam through different OPO configurations. The thesis also covers the generation of mentioned spatial structures in a wide spectral range starting from ultraviolet to the mid-IR region of the spectrum in both ultrafast as well as in the CW time domain.

In Chapter 3, we presented the study of the direct generation of the optical vortex and vortex dipoles from a CW and ultrafast OPO. In CW OPO, we genereated optical vortex in signal and idler with vortex order $l_s = l_i = 1$, through intracavity astgmatic mode conversion of HG_{01} mode. Generated optical vortices showed tunability across the near-IR region of the spectrum from 968 – 1180 nm. In ultrafast time domain, we used an anti-resonant ring (ARR) based pico-second OPO to generate optical vortices. We generated the HG_{01} mode through the output port of the ARR, which is further converted into the optical vortex of order 1 with the help of single cylindrical lens scheme. The generated of optical vortices showed tunability in the near-IR region across 1457 – 1657 nm with a maximum output power of 1 W, pulses width of 16.5 ps and 1.4 nm of spectral width.

In chapter 4, we presented method of vortex pumping to genrate higher-order, high power optical vortices over broad wavelength. We demonstrated the mechanism for pump OAM exchange between signal and idler in singly resonant OPO configuration. We also presented the SRO cavity configuration for high power optical vortices with OAM content as high as 3 in the near-IR region of the spectrum. The chapter is followed by another study, and we demonstrated the generation of higher-order optical vortices in the mid-IR region. We demonstrated the generation of optical vortices with a maximum order of 5 across 2493 nm to 4035 nm, with maximum output power in excess of 2 W.

Chapter 5 focused on the generation of optical vortices in the ultraviolet region of the spectrum. By successfully implementing the intracavity SFG based OPO, we generated the vortex beam of order l_{uv} =1, 2 across 332 nm to 344 nm. With OAM conservation in this OPO, we also generated optical vortices with maximum order 2 in the near-IR region from 1172-1338 nm, with a maximum output power of 1.3 W.

In chapter 6, we moved our discussion to the tunable vector-vortex beam generation. We demonstrated the successful generation of vector vortex beam from a vortex pumped doubly resonating nanosecond OPO. The generated vector vortex beam is tunable from 964 nm to 990 nm with few µJ pulse energies.

In chapter 7, we studied the simultaneous generation of multiple spatial structures from a single OPO. In this work, we demonstrated a synchronous vortex pumped picosecond SRO, in combination with the intracavity CPM technique. By using this scheme, we generated the Gaussian, vortex, Airy and vortex-Air beam from a single OPO. All mentioned spatial

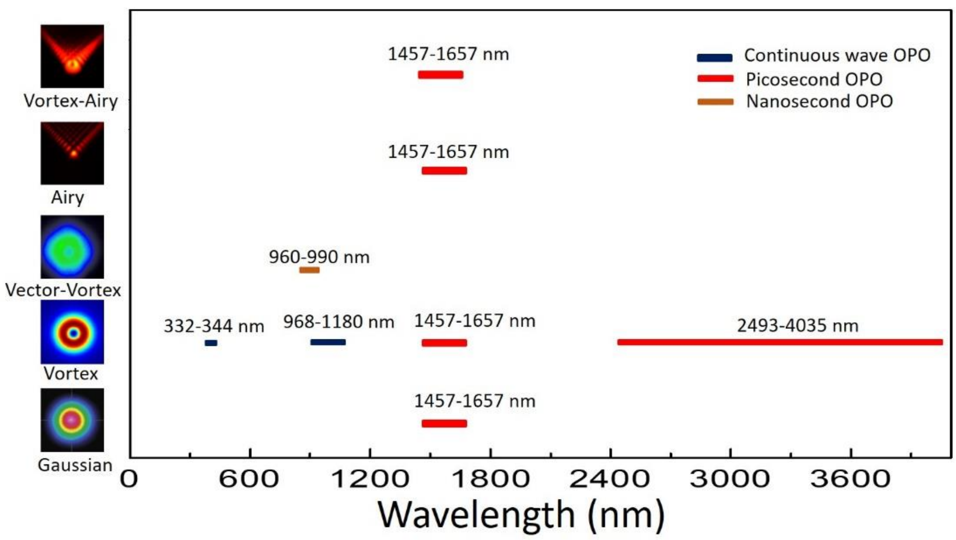

Figure 8.1. Different spatial structure generation across the wavelength region studied in this thesis

structures showed tunability from 1457 nm to 1680 nm in the signal and 2901 to 3944 nm in the idler region. Figure 8.1 is summarising this thesis, with a description of the different spatial structures generated from UV to the mid-IR region.

8.2 Future work

Optical parametric oscillators are mostly based upon the Gaussian intensity distribution and used in various applications. Developing OPOs with different spatial structures can extend their application in different unexplored areas. In this thesis, we have only focused on the generation of optical vortices, vector beams, Airy beam, and vortex-Airy beam across different parts of the wavelength spectrum. This thesis can be used as a foundation for the generation of other spatial structures, such as vector-Airy beam, hollow Gaussian beams, and Bessel beams from the OPOs. Out of various ideas, there are few projects from the part of our future works.

8.2.1 Tunable blue vortex beam source

Since most of the quantum optics work requires pump source at 405 nm and current methods are dependent on the diode lasers. They have limitations in term of poor beam quality and frequency stabilization, these limitations can be easily overcome by using intracavity SHG in green pumped OPOs. Such OPO configurations provide frequency stabilized output beams with good beam quality. Method of vortex pumping can be extended for this scheme, which will generate optical vortices in the blue region and their implementation for the down-conversion process can be used to study the OAM entanglement in signal and idler.

8.2.2 Vector-vortex Airy beam OPO

The generation of vector-vortex Airy beam requires a complicated setup with the involvement of different phase elements and interferometers. We would like to generate vector Airy beams by superposing two orthogonal polarized scalar Airy beams inside an OPO. Different forms of polarization singularity are possible, which depend on the way two Airy beams are superposed. When the dark point along the x-axis for x-polarized Airy beams (between the main lobe and its neighbour in the x-polarized Airy beams) overlap with the dark point along the y-axis for y-polarized Airy beams, they generate radially polarized Airy beams. However, when the dark point along the x-axis for y-polarized Airy beams overlap with the dark point along the y-axis for x-polarized Airy beams, then azimuthally polarized Airy beams are generated. With two independent OPOs, we can control the OPOs to maintain a relative angle among the beams inside the anti-resonating ring which in turn produce angle between the orthogonal polarization components of the cubic phase modulated beams. Using a Fourier transforming lens we will generate a vector vortex beam from the cubic phase modulated beams.

Bibliography

1. B. C. Stuart, M. D. Feit, A. M. Rubenchik, B. W. Shore, and M. D. Perry, "Laser-Induced Damage in Dielectrics with Nanosecond to Subpicosecond Pulses," Phys. Rev. Lett. **74**(12), 2248–2251 (1995).

2. N. E. Schore, "Modern molecular photochemistry (Turro, Nicholas J.)," J. Chem. Educ. **58**(10), A312 (1981).

3. V. W. S. Chan, "Free-Space Optical Communications," J. Light. Technol. **24**(12), 4750–4762 (2006).

4. S. Wieneke and C. Gerhard, *Lasers in Medical Diagnosis and Therapy*, 2053-2563 (IOP Publishing, 2018).

5. J. Hecht, "Short history of laser development," Opt. Eng. **49**(9), 1–23 (2010).

6. M. Harris, C. A. Hill, P. R. Tapster, and J. M. Vaughan, "Laser modes with helical wave fronts," Phys. Rev. A **49**(4), 3119–3122 (1994).

7. J. F. Nye and and M. V. Berry, "No Title," Proc. R. Soc. Lond. A **336**(1605), (1974).

8. L. Allen, M. W. Beijersbergen, R. J. C. Spreeuw, and J. P. Woerdman, "Orbital angular momentum of light and the transformation of Laguerre-Gaussian laser modes," Phys. Rev. A **45**(11), 8185–8189 (1992).

9. A. Mair, A. Vaziri, G. Weihs, and A. Zeilinger, "Entanglement of the orbital angular momentum states of photons," Nature **412**(6844), 313–316 (2001).

10. Y. Yan, G. Xie, M. P. J. Lavery, H. Huang, N. Ahmed, C. Bao, Y. Ren, Y. Cao, L. Li, Z. Zhao, A. F. Molisch, M. Tur, M. J. Padgett, and A. E. Willner, "High-capacity millimetre-wave communications with orbital angular momentum multiplexing," Nat.

Commun. **5**(1), 4876 (2014).

11. K. Toyoda, K. Miyamoto, N. Aoki, R. Morita, and T. Omatsu, "Using Optical Vortex To Control the Chirality of Twisted Metal Nanostructures," Nano Lett. **12**(7), 3645–3649 (2012).

12. M. W. Beijersbergen, L. Allen, H. E. L. O. van der Veen, and J. P. Woerdman, "Astigmatic laser mode converters and transfer of orbital angular momentum," Opt. Commun. **96**(1), 123–132 (1993).

13. N. R. Heckenberg, R. McDuff, C. P. Smith, and A. G. White, "Generation of optical phase singularities by computer-generated holograms," Opt. Lett. **17**(3), 221–223 (1992).

14. M. W. Beijersbergen, R. P. C. Coerwinkel, M. Kristensen, and J. P. Woerdman, "Helical-wavefront laser beams produced with a spiral phaseplate," Opt. Commun. **112**(5), 321–327 (1994).

15. D. Naidoo, F. S. Roux, A. Dudley, I. Litvin, B. Piccirillo, L. Marrucci, and A. Forbes, "Controlled generation of higher-order Poincaré sphere beams from a laser," Nat. Photonics **10**, 327 (2016).

16. K. Huang, P. Shi, G. W. Cao, K. Li, X. B. Zhang, and Y. P. Li, "Vector-vortex Bessel--Gauss beams and their tightly focusing properties," Opt. Lett. **36**(6), 888–890 (2011).

17. S. Matsusaka, Y. Kozawa, and S. Sato, "Micro-hole drilling by tightly focused vector beams," Opt. Lett. **43**(7), 1542–1545 (2018).

18. H. Moradi, V. Shahabadi, E. Madadi, E. Karimi, and F. Hajizadeh, "Efficient optical trapping with cylindrical vector beams," Opt. Express **27**(5), 7266–7276 (2019).

19. M. V Berry and N. L. Balazs, "Nonspreading wave packets," Am. J. Phys. **47**(3), 264–267 (1979).

20. G. A. Siviloglou, J. Broky, A. Dogariu, and D. N. Christodoulides, "Observation of Accelerating Airy Beams," Phys. Rev. Lett. **99**(21), 213901 (2007).

21. R. S. Grewal, A. Ghosh, and G. K. Samanta, "Simultaneous generation of high-power, ultrafast 1D and 2D Airy beams and their frequency-doubling characteristics," Opt. Lett. **43**(16), 3957–3960 (2018).

22. T. Vettenburg, H. I. C. Dalgarno, J. Nylk, C. Coll-Lladó, D. E. K. Ferrier, T. Čižmár, F. J. Gunn-Moore, and K. Dholakia, "Light-sheet microscopy using an Airy beam," Nat. Methods **11**, 541 (2014).

23. P. Polynkin, M. Kolesik, J. V Moloney, G. A. Siviloglou, and D. N. Christodoulides, "Curved Plasma Channel Generation Using Ultraintense Airy Beams," Science, **324**(5924), 229–232 (2009).

24. A. Mathis, F. Courvoisier, L. Froehly, L. Furfaro, M. Jacquot, P. A. Lacourt, and J. M. Dudley, "Micromachining along a curve: Femtosecond laser micromachining of curved profiles in diamond and silicon using accelerating beams," Appl. Phys. Lett. **101**(7), 71110 (2012).

25. P. A. Franken, A. E. Hill, C. W. Peters, and G. Weinreich, "Generation of Optical Harmonics," Phys. Rev. Lett. **7**(4), 118–119 (1961).

26. R. W. Boyd, *Nonlinear Optics, Third Edition*, 3rd ed. (Academic Press, Inc., 2008).

27. V. G. Dmitriev, G. G. Gurzadyan, and D. N. Nikogosyan, *Handbook of Nonlinear Optical Crystals*, 3rd ed. (Springer-Verlag Berlin Heidelberg, 1999).

28. N. A. Chaitanya, A. Aadhi, M. V Jabir, and G. K. Samanta, "High-power, high-repetition-rate, Yb-fiber laser based femtosecond source at 355 nm" Opt. Lett. **40**(18), 4269–4272 (2015).

29. Y. J. Ding, "Progress in terahertz sources based on difference-frequency generation," J. Opt. Soc. Am. B **31**(11), 2696–2711 (2014).

30. W. H. Louisell, A. Yariv, and A. E. Siegman, "Quantum Fluctuations and Noise in Parametric Processes. I.," Phys. Rev. **124**(6), 1646–1654 (1961).

31. D. C. Burnham and D. L. Weinberg, "Observation of Simultaneity in Parametric

Production of Optical Photon Pairs," Phys. Rev. Lett. **25**(2), 84–87 (1970).

32. K. Dholakia, N. B. Simpson, M. J. Padgett, and L. Allen, "Second-harmonic generation and the orbital angular momentum of light," Phys. Rev. A **54**(5), R3742--R3745 (1996).

33. P. D. Maker, R. W. Terhune, M. Nisenoff, and C. M. Savage, "Effects of Dispersion and Focusing on the Production of Optical Harmonics," Phys. Rev. Lett. **8**(1), 21–22 (1962).

34. J. A. Armstrong, N. Bloembergen, J. Ducuing, and P. S. Pershan, "Interactions between Light Waves in a Nonlinear Dielectric," Phys. Rev. **127**(6), 1918–1939 (1962).

35. G. D. Boyd and D. A. Kleinman, "Parametric Interaction of Focused Gaussian Light Beams," J. Appl. Phys. **39**(8), 3597–3639 (1968).

36. T. F. Scott, B. A. Kowalski, A. C. Sullivan, C. N. Bowman, and R. R. McLeod, "Two-Color Single-Photon Photoinitiation and Photoinhibition for Subdiffraction Photolithography," Science (80-.). **324**(5929), 913–917 (2009).

37. S. Fürhapter, A. Jesacher, S. Bernet, and M. Ritsch-Marte, "Spiral phase contrast imaging in microscopy," Opt. Express **13**(3), 689–694 (2005).

38. D. G. Grier, "A revolution in optical manipulation," Nature **424**(6950), 810–816 (2003).

39. L. Marrucci, C. Manzo, and D. Paparo, "Optical Spin-to-Orbital Angular Momentum Conversion in Inhomogeneous Anisotropic Media," Phys. Rev. Lett. **96**(16), 163905 (2006).

40. A. F. Carmelo Rosales-Guzmán, "How to Shape Light with Spatial Light Modulators," (2017).

41. N. A. Chaitanya, S. C. Kumar, K. Devi, G. K. Samanta, and M. Ebrahim-Zadeh, "Ultrafast optical vortex beam generation in the ultraviolet," Opt. Lett. **41**(12), 2715–

2718 (2016).

42. M. Granata, C. Buy, R. Ward, and M. Barsuglia, "Higher-Order Laguerre-Gauss Mode Generation and Interferometry for Gravitational Wave Detectors," Phys. Rev. Lett. **105**(23), 231102 (2010).

43. M. Kraus, M. A. Ahmed, A. Michalowski, A. Voss, R. Weber, and T. Graf, "Microdrilling in steel using ultrashort pulsed laser beams with radial and azimuthal polarization," Opt. Express **18**(21), 22305–22313 (2010).

44. Y. Shen, Y. Meng, X. Fu, and M. Gong, "Wavelength-tunable Hermite-Gaussian modes and an orbital-angular-momentum-tunable vortex beam in a dual-off-axis pumped Yb:CALGO laser," Opt. Lett. **43**(2), 291–294 (2018).

45. M. Ebrahim-Zadeh, S. C. Kumar, A. Esteban-Martin, and G. K. Samanta, "Breakthroughs in Photonics 2012: Breakthroughs in Optical Parametric Oscillators," IEEE Photonics J. **5**(2), 700105 (2013).

46. M. Ebrahim-Zadeh, "Continuous-wave optical parametric oscillators," in *OSA Handbook of Optics*, Vol. IV (McGraw-Hill, 2010).

47. G. K. Samanta, A. Aadhi, and M. Ebrahim-Zadeh, "Continuous-wave, two-crystal, singly-resonant optical parametric oscillator: Theory and experiment," Opt. Express **21**(8), 9520–9540 (2013).

48. M. Martinelli, J. A. O. Huguenin, P. Nussenzveig, and A. Z. Khoury, "Orbital angular momentum exchange in an optical parametric oscillator," Phys. Rev. A **70**(1), 13812 (2004).

49. A. Aadhi, G. K. Samanta, S. C. Kumar, and M. Ebrahim-Zadeh, "Controlled switching of orbital angular momentum in an optical parametric oscillator," Optica **4**(3), 349–355 (2017).

50. V. Sharma, S. C. Kumar, G. K. Samanta, and M. Ebrahim-Zadeh, "Orbital angular momentum exchange in a picosecond optical parametric oscillator," Opt. Lett. **43**(15), 3606–3609 (2018).

51. A. Amon, P. Suret, S. Bielawski, D. Derozier, and M. Lefranc, "Cooperative Oscillation of Nondegenerate Transverse Modes in an Optical System: Multimode Operation in Parametric Oscillators," Phys. Rev. Lett. **102**(18), 183901 (2009).

52. D. N. Naik, T. P. Chakravarthy, and N. K. Viswanathan, "Generation of optical vortex dipole from superposition of two transversely scaled Gaussian beams," Appl. Opt. **55**(12), B91-B97 (2016).

53. G. K. Samanta, G. R. Fayaz, Z. Sun, and M. Ebrahim-Zadeh, "High-power, continuous-wave, singly resonant optical parametric oscillator based on MgO:sPPLT," Opt. Lett. **32**(4), 400–402 (2007).

54. R. Uren, S. Beecher, C. R. Smith, and W. A. Clarkson, "Novel Method for Generating High Purity Vortex Modes," in *2018 Conference on Lasers and Electro-Optics (CLEO)* (2018), pp. 1–2.

55. A. Esteban-Martin, O. Kokabee, and M. Ebrahim-Zadeh, "Optimum output coupling in optical oscillators using an antiresonant ring interferometer," Opt. Lett. **35**(16), 2786–2788 (2010).

56. A. Siegman, "An antiresonant ring interferometer for coupled laser cavities, laser output coupling, mode locking, and cavity dumping," IEEE J. Quantum Electron. **9**(2), 247–250 (1973).

57. D. Milam, R. Bradbury, A. Hordvik, H. Schlossberg, and A. Szoke, "Production of intense subnanosecond pulses by cavity dumping," IEEE J. Quantum Electron. **10**(1), 20–25 (1974).

58. W. R. Kerridge-Johns and M. J. Damzen, "Vortex laser from anti-resonant ring coupled cavities," Opt. Express **26**(25), 32839–32846 (2018).

59. O. Kimmelma, S. C. Kumar, A. Esteban-Martin, and M. Ebrahim-Zadeh, "Multi-gigahertz picosecond optical parametric oscillator pumped by 80-MHz Yb-fiber laser," Opt. Lett. **38**(22), 4550–4553 (2013).

60. K. Devi, S. C. Kumar, A. Esteban-Martin, and M. Ebrahim-Zadeh, "Antiresonant ring

output-coupled continuous-wave optical parametric oscillator," Opt. Express **20**(17), 19313–19321 (2012).

61. P. Vaity, A. Aadhi, and R. P. Singh, "Formation of optical vortices through superposition of two Gaussian beams," Appl. Opt. **52**(27), 6652–6656 (2013).

62. H. A. Nam, M. G. Cohen, and J. W. Noé, "A simple method for creating a robust optical vortex beam with a single cylinder lens," J. Opt. **13**(6), 64026 (2011).

63. J. Courtial, K. Dholakia, L. Allen, and M. J. Padgett, "Second-harmonic generation and the conservation of orbital angular momentum with high-order Laguerre-Gaussian modes," Phys. Rev. A **56**(5), 4193–4196 (1997).

64. A. Beržanskis, A. Matijošius, A. Piskarskas, V. Smilgevičius, and A. Stabinis, "Sum-frequency mixing of optical vortices in nonlinear crystals," Opt. Commun. **150**(1), 372–380 (1998).

65. A. P. Piskarskas, "OPTICAL PARAMETRIC TUNABLE, GENERATORS: POWERFUL & ULTRAFAST," Opt. Photon. News **8**(7), 24 (1997).

66. T. Südmeyer, J. A. der Au, R. Paschotta, U. Keller, P. G. R. Smith, G. W. Ross, and D. C. Hanna, "Novel ultrafast parametric systems: high repetition rate single-pass {OPG} and fibre-feedback {OPO}," J. Phys. D. Appl. Phys. **34**(16), 2433–2439 (2001).

67. R. Baumgartner and R. Byer, "Optical parametric amplification," IEEE J. Quantum Electron. **15**(6), 432–444 (1979).

68. A. Aadhi and G. K. Samanta, "High-power, high repetition rate, tunable, ultrafast vortex beam in the near-infrared," J. Opt. **20**(1), 01LT01 (2017).

69. A. Aadhi, V. Sharma, R. P. Singh, and G. K. Samanta, "Continuous-wave, singly resonant parametric oscillator-based mid-infrared optical vortex source," Opt. Lett. **42**(18), 3674–3677 (2017).

70. B. C. dos Santos, K. Dechoum, and A. Z. Khoury, "Continuous-Variable Hyperentanglement in a Parametric Oscillator with Orbital Angular Momentum,"

Phys. Rev. Lett. **103**(23), 230503 (2009).

71. K. Liu, J. Guo, C. Cai, S. Guo, and J. Gao, "Experimental Generation of Continuous-Variable Hyperentanglement in an Optical Parametric Oscillator," Phys. Rev. Lett. **113**(17), 170501 (2014).

72. A. Aadhi, V. Sharma, and G. K. Samanta, "High-power, continuous-wave, tunable mid-IR, higher-order vortex beam optical parametric oscillator," Opt. Lett. **43**(10), 2312–2315 (2018).

73. S. C. Kumar, E. S. Bautista, and M. Ebrahim-Zadeh, "Stable, high-power, Yb-fiber-based, picosecond ultraviolet generation at 355 nm using BiB3O6," Opt. Lett. **40**(3), 403–406 (2015).

74. P. Vaity, J. Banerji, and R. Singh, "Measuring the topological charge of an optical vortex by using a tilted convex lens," Phys. Lett. A **377**, 1154–1156 (2013).

75. N. A. Chaitanya, A. Aadhi, M. V Jabir, and G. K. Samanta, "Frequency-doubling characteristics of high-power, ultrafast vortex beams," Opt. Lett. **40**(11), 2614–2617 (2015).

76. C. R. Webster, G. J. Flesch, D. C. Scott, J. E. Swanson, R. D. May, W. S. Woodward, C. Gmachl, F. Capasso, D. L. Sivco, J. N. Baillargeon, A. L. Hutchinson, and A. Y. Cho, "Quantum-cascade laser measurements of stratospheric methane and nitrous oxide," Appl. Opt. **40**(3), 321–326 (2001).

77. Y. A. Bakhirkin, A. A. Kosterev, C. Roller, R. F. Curl, and F. K. Tittel, "Mid-infrared quantum cascade laser based off-axis integrated cavity output spectroscopy for biogenic nitric oxide detection," Appl. Opt. **43**(11), 2257–2266 (2004).

78. B. Guo, Y. Wang, C. Peng, H. L. Zhang, G. P. Luo, H. Q. Le, C. Gmachl, D. L. Sivco, M. L. Peabody, and A. Y. Cho, "Laser-based mid-infrared reflectance imaging of biological tissues," Opt. Express **12**(1), 208–219 (2004).

79. R. Imai, N. Kanda, T. Higuchi, K. Konishi, and M. Kuwata-Gonokami, "Generation of broadband terahertz vortex beams," Opt. Lett. **39**(13), 3714–3717 (2014).

80. J. Ni, C. Wang, C. Zhang, Y. Hu, L. Yang, Z. Lao, B. Xu, J. Li, D. Wu, and J. Chu, "Three-dimensional chiral microstructures fabricated by structured optical vortices in isotropic material," Light Sci. Appl. **6**(7), e17011–e17011 (2017).

81. R. Das, S. C. Kumar, G. K. Samanta, and M. Ebrahim-Zadeh, "Broadband, high-power, continuous-wave, mid-infrared source using extended phase-matching bandwidth in MgO:PPLN," Opt. Lett. **34**(24), 3836–3838 (2009).

82. J.-W. Pan, M. Daniell, S. Gasparoni, G. Weihs, and A. Zeilinger, "Experimental Demonstration of Four-Photon Entanglement and High-Fidelity Teleportation," Phys. Rev. Lett. **86**(20), 4435–4438 (2001).

83. A. K. Jayasinghe, J. Rohner, and M. S. Hutson, "Holographic UV laser microsurgery," Biomed. Opt. Express **2**(9), 2590–2599 (2011).

84. C. Corsi, I. Liontos, S. Cavalieri, M. Bellini, G. Venturi, and R. Eramo, "An ultrastable Michelson interferometer for high-resolution spectroscopy in the XUV," Opt. Express **23**(4), 4106–4113 (2015).

85. A. Sakdinawat and Y. Liu, "Soft-x-ray microscopy using spiral zone plates," Opt. Lett. **32**(18), 2635–2637 (2007).

86. M. van Veenendaal and I. McNulty, "Prediction of Strong Dichroism Induced by X Rays Carrying Orbital Momentum," Phys. Rev. Lett. **98**(15), 157401 (2007).

87. Y. Sasaki, K. Yamaguchi, J. Shibakawa, K. Miyamoto, and T. Omatsu, "Ultraviolet optical vortex generation using a pair of β-BaB2O4 crystals with inverted orientations," Appl. Opt. **56**(29), 8075–8080 (2017).

88. G. Gariepy, J. Leach, K. T. Kim, T. J. Hammond, E. Frumker, R. W. Boyd, and P. B. Corkum, "Creating High-Harmonic Beams with Controlled Orbital Angular Momentum," Phys. Rev. Lett. **113**(15), 153901 (2014).

89. A. Aadhi, N. A. Chaitanya, R. P. Singh, and G. K. Samanta, "High-power, continuous-wave, solid-state, single-frequency, tunable source for the ultraviolet," Opt. Lett. **39**(12), 3410–3413 (2014).

90. K. Devi, S. C. Kumar, and M. Ebrahim-Zadeh, "Tunable, continuous-wave, ultraviolet source based on intracavity sum-frequency-generation in an optical parametric oscillator using BiB3O6," Opt. Express **21**(21), 24829–24836 (2013).

91. G. Vallone, V. D’Ambrosio, A. Sponselli, S. Slussarenko, L. Marrucci, F. Sciarrino, and P. Villoresi, "Free-Space Quantum Key Distribution by Rotation-Invariant Twisted Photons," Phys. Rev. Lett. **113**(6), 60503 (2014).

92. H. Cheng, P. Li, S. Liu, P. Chen, L. Han, Y. Zhang, W. Hu, and J. Zhao, "Vortex-controlled morphology conversion of microstructures on silicon induced by femtosecond vector vortex beams," Appl. Phys. Lett. **111**(14), 141901 (2017).

93. B. Yao, S. Yan, M. Lei, F. Peng, B. Ma, and T. Ye, "Optical trapping with cylindrical vector beams," in *2011 Functional Optical Imaging* (2011), p. 1.

94. M. V Jabir, N. Apurv Chaitanya, M. Mathew, and G. K. Samanta, "Direct transfer of classical non-separable states into hybrid entangled two photon states," Sci. Rep. **7**(1), 7331 (2017).

95. D. P. Biss, K. S. Youngworth, and T. G. Brown, "Dark-field imaging with cylindrical-vector beams," Appl. Opt. **45**(3), 470–479 (2006).

96. G. Milione, H. I. Sztul, D. A. Nolan, and R. R. Alfano, "Higher-Order Poincaré Sphere, Stokes Parameters, and the Angular Momentum of Light," Phys. Rev. Lett. **107**(5), 53601 (2011).

97. F. Cardano, E. Karimi, S. Slussarenko, L. Marrucci, C. de Lisio, and E. Santamato, "Polarization pattern of vector vortex beams generated by q-plates with different topological charges," Appl. Opt. **51**(10), C1--C6 (2012).

98. M. Bashkansky, D. Park, and F. K. Fatemi, "Azimuthally and radially polarized light with a nematic SLM," Opt. Express **18**(1), 212–217 (2010).

99. W. J. Lai, B. C. Lim, P. B. Phua, K. S. Tiaw, H. H. Teo, and M. H. Hong, "Generation of radially polarized beam with a segmented spiral varying retarder," Opt. Express **16**(20), 15694–15699 (2008).

100. G. Milione, S. Evans, D. A. Nolan, and R. R. Alfano, "Higher Order Pancharatnam-Berry Phase and the Angular Momentum of Light," Phys. Rev. Lett. **108**(19), 190401 (2012).

101. H. Kawauchi, Y. Kozawa, and S. Sato, "Generation of radially polarized Ti:sapphire laser beam using a c-cut crystal," Opt. Lett. **33**(17), 1984–1986 (2008).

102. Y. Kozawa and S. Sato, "Generation of a radially polarized laser beam by use of a conical Brewster prism," Opt. Lett. **30**(22), 3063–3065 (2005).

103. G. K. Samanta and M. Ebrahim-Zadeh, "Continuous-wave singly-resonant optical parametric oscillator with resonant wave coupling," Opt. Express **16**(10), 6883–6888 (2008).

104. D. Wei, Y. Cheng, R. Ni, Y. Zhang, X. Hu, S. Zhu, and M. Xiao, "Generating Controllable Laguerre-Gaussian Laser Modes Through Intracavity Spin-Orbital Angular Momentum Conversion of Light," Phys. Rev. Appl. **11**(1), 14038 (2019).

105. S. U. Alam, A. S. Rao, A. Ghosh, P. Vaity, and G. K. Samanta, "Nonlinear frequency doubling characteristics of asymmetric vortices of tunable, broad orbital angular momentum spectrum," Appl. Phys. Lett. **112**(17), 171102 (2018).

106. P. Zhang, J. Prakash, Z. Zhang, M. S. Mills, N. K. Efremidis, D. N. Christodoulides, and Z. Chen, "Trapping and guiding microparticles with morphing autofocusing Airy beams," Opt. Lett. **36**(15), 2883–2885 (2011).

107. G. Porat, I. Dolev, O. Barlev, and A. Arie, "Airy beam laser," Opt. Lett. **36**(20), 4119–4121 (2011).

108. A. Aadhi, N. A. Chaitanya, M. V Jabir, P. Vaity, R. P. Singh, and G. K. Samanta, "Airy beam optical parametric oscillator," Sci. Rep. **6**, 25245 (2016).

109. J. Zhou, Y. Liu, Y. Ke, H. Luo, and S. Wen, "Generation of Airy vortex and Airy vector beams based on the modulation of dynamic and geometric phases," Opt. Lett. **40**(13), 3193–3196 (2015).